Understanding the molecular basis of neuronal 3'UTR length-dependent mRNA sorting

Julia Grawenhoff

TESI DOCTORAL UPF / 2023

Thesis supervisor

Dr. Thomas Surrey

Quantitative Cell Biology Program
Centre for Genomic Regulation (CRG)

DEPARTMENT OF MEDICINE AND LIFE SCIENCES
UNIVERSITAT POMPEU FABRA

Acknowledgments

After 5 and a half years, my PhD journey comes to its end.

I would like to thank Sebastian, who has given me the opportunity to merge my interest in RNAs, proteins and their interactions by studying the transport of mRNAs within mRNA transport complexes. Thank you for always sharing my excitement about new data and for always believing in me! I like to think back to the moments in which we celebrated the first successful purification of SRSF3 and the first time I observed co-transport of NXF1 and SRSF3. Although I did not finish my PhD in your lab, it was a pleasure to work with you.

I would also like to thank Thomas, who became my PI in 2021, when Sebastian's lab closed. Thank you for not only giving me the chance to finish my PhD, but also for dedicating a huge amount of effort to understanding a new field, providing me with the best supervision possible and supporting me during a difficult time. One of my favorite memories will always be when you came to me with the "Molecular Biology of the Cell", showing me a cartoon of an mRNA and a protein, and being astonished by how much bigger an mRNA is compared to a protein.

I would also like to express my gratitude to my thesis committee, Thomas Surrey, Dierk Niessing, and Sophie Bonnal. I remember being really nervous during my first meeting in 2019, when Thomas came all the way from the UK, and Dierk came all the way from Germany, just to hear about my first year as a PhD student. Who would have known back then which important role Thomas and Dierk would play in my journey as a PhD student! Thank you for all the fruitful discussions, amazing feedback and support!

In 2019, I was so happy to be able to present my work to the German mRNA localization field, when Sebastian asked me to join him for the FOR2333 Research Unit meeting in Günzburg. Who would have known back then that Dierk, as the head of the research unit, would not only invite me to the next FOR2333 meeting in 2022, but also offer me to become an "associated scientist". This was the greatest honor ever, thank you so much for supporting me and believing in me and my work. I loved hearing about the exciting research and getting to know all of the PIs, Postdocs and PhD students, especially in the castle bar in the evenings! Thank you, FOR233, for not only giving me a travel grant to attend the International Conference on mRNA localization in Düsseldorf in 2022 and assigning me a talk, but also for giving me my first experience as a session chair!

Next, I want to thank the Maurer lab: Magüi, Silvia, Artem, Elsa, Andrea and Bogu, every day in the lab was so much fun and you felt and still feel like family to me! Magüi, you were there from the first to the last day of my PhD. Thank you for celebrating every success with me and for consoling me during every small setback, for being there for me in the most difficult situations, for all the morning coffees and laughs, and of course for all the support! Silvia, when you prepared tiramisu for the 7 am breakfast during the tubulin prep after your first week in the lab, you had already earned a place in my heart. Thank you for all the fun times in- and outside of the lab! Artem, you are one of the craziest people I know, and there was never a boring day with you. Elsa, you became such an important friend to me, and I thank you for everything. Andrea, Bogu, even though we didn't overlap a lot in the lab, you received me in the lab with open arms and I could not have imagined a better start into my PhD. I love the fact that we all remain close to each other, and I look forward to our next reunion!

In addition to the Maurer lab, I would like to express my gratitude to the entire Surrey lab for welcoming me as a new lab member. Cláudia, I want to extend special thanks to you for becoming such an important person in my life.

Of course, thank you also to Eduardo from the CRG IT support, who saved my corrupted thesis file 2 days before submission. You deserve all the cookies in the world!

Fede, Laasya and Queralt, thank you for all the nice times in the past years and for sharing the PhD journey with me! Ishier and José, thank you for your mentoring!

Dominik and Claudia, thank you for your amazing friendship, not only during all those years in Heidelberg but also ever since. Katharina, I could not imagine my time in Heidelberg without you. Besides being my Bachelor and Master theses supervisor, you became a true friend. Thank you for introducing me to the RNA world! I learned so much from you, and working alongside you was a fantastic experience.

I could not have completed my PhD without the help of my family. I would especially like to thank my mother, who always supports and helps me in everything I do.

Finally, my biggest gratitude goes to my partner, Miguel. Muchísimas gracias por estar a mi lado en los buenos y malos momentos, y por apoyarme en todo.

Abstract

The local translation of messenger RNAs (mRNAs) within specialized neuronal compartments is a prerequisite for synaptic plasticity which underlies the formation of long-term memories. mRNAs are localized via active transport along microtubules, an extensively studied process, yet the associated mechanisms, dynamic interactions and key contributors remain poorly understood to this day.

Recently, a novel many-by-many protein interaction screening approach suggested yet unknown interactions between microtubule motor proteins, the major nuclear export factor NXF1 and its adaptor SRSF3. Using a total internal reflection fluorescence microscopy-based in vitro reconstitution approach with recombinant full-length proteins, we were able to reconstitute an RNA transport system consisting of these factors, revealing a potential link between the export of mRNAs and their active transport along microtubules in neurons.

Besides being an NXF1 adaptor, SRSF3 functions as a regulator of 3’ untranslated region (3’UTR) length. As 3’UTR length has only recently been discovered as an important determinant of mRNA localization, this reconstituted system potentially also establishes the groundwork for studying and understanding 3’UTR length-dependent mRNA sorting in neurons.

Resum

La traducció local d'ARNs missatgers (ARNms) dins de compartiments neuronals especialitzats és un requisit previ per a la plasticitat sinàptica que hi ha darrere de la formació de memòria a llarg termini. Els ARNms es localitzen mitjançant el transport actiu al llarg dels microtúbuls, un procés àmpliament estudiat, tot i que els mecanismes associats, les interaccions dinàmiques i els contribuents clau segueixen sent poc coneguts fins avui.

Recentment, un nou enfocament de cribratge d'interacció de proteïnes va suggerir interaccions encara desconegudes entre proteïnes motores de microtúbuls, el principal factor d'exportació nuclear NXF1 i el seu adaptador SRSF3. Utilitzant un enfocament de reconstitució in vitro basat en microscòpia de fluorescència de reflexió interna total amb proteïnes recombinants de longitud completa, vam poder reconstituir un sistema de transport d'ARN que consistia en aquests factors, revelant un enllaç potencial entre l'exportació de l'ARNm i el seu transport actiu al llarg dels microtúbuls a les neurones.

A més de ser un adaptador de NXF1, SRSF3 funciona com un regulador de longitud de 3' de la regió no traduïda (3'UTR). Com que la longitud de 3'UTR només s'ha descobert recentment com un determinant important de la localització de l'ARNm, aquest sistema reconstituït també estableix les bases per estudiar i entendre la classificació de l'ARNm depenent de la longitud de 3'UTR a les neurones.

Table of Contents

List of Figures

List of Abbreviations

AD	Activation Domain
ADP	Adenosine Diphosphate
ATP	Adenosine Triphosphate
BD	Binding Domain
BDNF	Brain-Derived Neurotrophic Factor
BRET	Bioluminescence Resonance Energy Transfer
CLIP	Cross-Linking Immunoprecipitation
co-IP	Co-Immunoprecipitation
CTE	Constitutive Transport Element
CV	Column Volumes
DHC	Dynein Light Chain
DIC	Dynein Intermediate Chain
DLC	Dynein Light Chain
DLIC	Dynein Light Intermediate Chain
DoG	Difference of Gaussian
EB1	Microtubule End-Binding Protein 1
EB2	Microtubule End-Binding Protein 2
EB3	Microtubule End-Binding Protein 3
FEZ2	Fasciculation and Elongation Zeta Factor 2
FMRP	Fragile X Mental Retardation Protein
fps	Frames Per Second
FT	Flow-Through
G-quadruplexes	Guanine Quadruplex RNA Structures
hNXF5	Homo Sapiens NXF5
IP	Immunoprecipitation
IPTG	Isopropyl □-D-1-Thiogalactopyranoside
KHC	Kinesin-1 Heavy Chain
KLC	Kinesin-1 Light Chain
KLC4	Kinesin-1 Light Chain 4
LMT	Linear Motion Tracker
LRR	Leucine-Rich Repeat
MAP	Microtubule-Associated Protein
MAP7	Microtubule-Associated Protein 7
MBP	Maltose-Binding Protein

mNXF2	Mus Musculus NXF2
mNXF7	Mus Musculus NXF7
mRNA	messenger RNA
mRNP	messenger Ribonucleoprotein
MWCO	Molecular Weight Cut-Off
NanoLuc	Nanoluciferase
NGS	Next-Generation Sequencing
NPC	Nuclear Pore Complex
NTF2L	Nuclear Transport Factor 2-Like
NusA	N-Utilization Substance Protein A
NXF1	Nuclear Export Factor 1
OD	Optical Density
ORF	Open Reading Frame
P	Pellet
PAS	Polyadenylation Site
P-bodies	Processing Bodies
PEG	Biotin-Polyethylenglycol
PLL	Poly(L-Lysine)
PTM	Post-Translational Modification
RBD	RNA-Binding Domain
RBP	RNA-Binding Protein
rec-YnH	Recombination Yeast-n-Hybrid
RNP	Ribonucleoprotein
Robl	Roadblock
RRM	RNA Recognition Motif
RS	Arginine/Serine
RT	Room Temperature
RTRAF	RNA Transcription, Translation and Transport Factor Protein
SEC	Size Exclusion Chromatography
SELEX	Systematic Evolution of Ligands by Exponential Enrichment
SN	Supernatant
SRSF3	Serine/Arginine-rich Splicing Factor 3
SUMO3	Small Ubiquitin-Like Modifier 3
TIRF-M	Total Internal Reflection Fluorescence Microscopy
TMR	Tetramethylrhodamin
UBA	Ubiquitin-Associated Domain
UTR	Untranslated Region

Y2H	Yeast-2-Hybrid
ZZ-tag	Protein A Solubility Tag
ΨRRM	Pseudo-RNA Recognition Motif

Preface

In this thesis, I will present the work of my main PhD project, entitled "Understanding the molecular basis of neuronal 3'UTR length-dependent mRNA sorting", which was designed and predominantly carried out in the laboratory of Sebastian Maurer, and then after the Maurer laboratory closed, continued and completed in the laboratory of Thomas Surrey.

The main project of this PhD thesis resulted in two publications: (1) a review of the mRNA transport field as well as (2) a publication describing the specific in vitro reconstitution method developed and used, which will both be discussed thoroughly in the Introduction (chapter 1) and Results section (chapter 4) of this thesis:

1. Rodrigues EC*, Grawenhoff J*, Baumann SJ, Lorenzon N, Maurer SP (2021). Mammalian Neuronal mRNA Transport Complexes: The Few Knowns and the Many Unknowns. Front. Integr. Neurosci. 15:692948. https://doi.org/10.3389/fnint.2021.692948

   *Equal contribution

2. Grawenhoff J*, Baumann S*, Maurer SP (2022). In Vitro Reconstitution of Kinesin-Based, Axonal mRNA Transport. Methods Mol Biol. 2431:547-568. https://doi.org/10.1007/978-1-0716-1990-2_29

   *Equal contribution

A smaller contribution to another project, entitled "APC couples neuronal mRNAs to multiple kinesins, EB1, and shrinking microtubule ends for bidirectional mRNA motility" will not be discussed in this thesis, as it thematically differs from the main PhD project presented:

1. Baumann SJ, Grawenhoff J, Rodrigues EC, Speroni S, Gili M, Komissarov A, Maurer SP (2022). APC couples neuronal mRNAs to multiple kinesins, EB1, and shrinking microtubule ends for bidirectional mRNA motility. PNAS 119(50):e2211536119. https://doi.org/10.1073/pnas.2211536119

1. INTRODUCTION

1.1. What is an mRNA?

Messenger RNA (mRNA) plays a fundamental role in all forms of life. It is a crucial element in the central dogma of biology, serving as an intermediary factor that connects the genetic information encoded in the DNA with the synthesis of proteins. It thereby carries this genetic information from the nucleus to the cytoplasm, where it can be translated into proteins.

Besides the coding region, which contains all necessary information for the synthesis of a protein, mRNAs contain two untranslated regions (UTRs) at each end of the molecule: The 5'UTR is located upstream of the coding region, whereas the 3'UTR is located downstream of it (Figure 1).

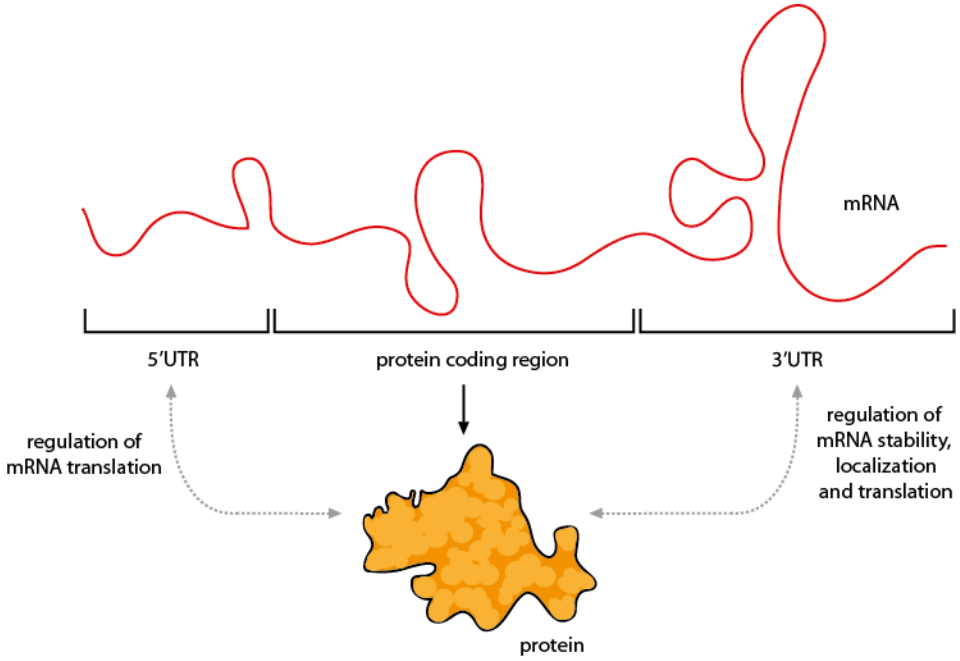

Figure 1: The components of an mRNA. An mRNA consists of a coding region as well as a 5' and 3' untranslated region (UTR). While the coding region contains all information necessary for the synthesis of a protein, the UTRs regulate its stability, localization and translation.

These two UTRs have expanded evolutionary in higher eukaryotes (reviewed in (Chen et al. 2012; Mayr 2016)), can span from a few dozen to thousands of nucleotides and are often highly conserved (Siepel et al. 2005; Xie et al. 2005). They

fulfill different functions in the cell: While 5'UTRs influence the translational regulation of mRNAs, 3'UTRs regulate mRNA stability, mRNA localization, and also mRNA translation to a certain extent (reviewed in (Leppek, Das, and Barna 2018; Mayr 2019)). With the help of its UTRs, an mRNA thus adds an extra layer of regulation to the genetic information, allowing for the fine-tuning and control of protein expression.

1.2. Proteins are translated locally

In order for genetic information to be translated into proteins in the cytoplasm, the cell requires several components and processes, including: (1) the mRNA as a message, (2) the ribosome as a translator of this message, (3) protein regulators such as translation initiation factors, and (4) transfer RNAs as decoders of the message (reviewed in (Shirokikh and Preiss 2018)). Interestingly, in the past decades, it has become increasingly clear that protein synthesis based on these factors is not uniformly distributed throughout the cytoplasm.

The concept of localized translation came about in the 1950s, when two distinct populations of ribosomes were observed under the electron microscope: those that were (1) freely distributed in the cytoplasm as well as those that were (2) bound to the membrane of the endoplasmic reticulum (Palade 1955). Further investigations in the 1970s revealed that protein translation at membranes is not restricted to the endoplasmic reticulum, but also occurs at the inner and outer membranes of mitochondria, facilitating the import of locally synthesized proteins into mitochondria (Kellems, Allison, and Butow 1974; Kellems and Butow 1972).

Since then, local protein synthesis has been described to take place within or in close proximity to various cellular compartments, including peroxisomes, RNA granules (reviewed in (Lashkevich and Dmitriev 2021)), as well as distal regions of highly polarized cells like neurons (reviewed in (Bourke, Schwarz, and Schuman 2023)).

Notably, in all of the described cases, the localization of mRNAs to specific compartments within the cell is a pre-requisite for local translation. It is thus crucial to understand the mechanisms with which mRNA localization is achieved and regulated. Our focus thereby lies in understanding the asymmetric localization of mRNAs in the cytoplasm. In the subsequent sections, I will summarize the current knowledge on cytoplasmic mRNA localization and will propose novel factors and mechanisms that may contribute to and advance our understanding of this fundamental process.

1.3. Principles of mRNA localization

1.3.1. mRNA localization is a conserved mechanism

The earliest report of mRNA localization dates back to 1983, when β-actin mRNA was described to be asymmetrically localized in eggs and embryos of the ascidian Styela plicata (Jeffery, Tomlinson, and Brodeur 1983), participating in cytoplasmic segregation following fertilization, and differential distribution to mesodermal cell lineages during embryogenesis.

Since then, mRNA localization has been observed in all kingdoms of life (reviewed in (Das et al. 2021)), spanning bacteria (Nevo-Dinur et al. 2011), plants (Michaud, Maréchal-Drouard, and Duchêne 2010; Okita and Choi 2002), fungi (Niessing et al. 2018; Shepard et al. 2003) and animals (reviewed in (Holt and Bullock 2009)) (Figure 2). The asymmetric localization of mRNAs fulfills a variety of fundamental functions, several of which can be found in the literature:

a) In Drosophila melanogaster embryos, more than 70% of mRNAs are asymmetrically localized (Lécuyer et al. 2007), playing a crucial role in the spatial patterning of the embryo. Key examples of locally enriched mRNAs include bicoid and oskar mRNAs, which localize to opposite poles, forming the anterior-posterior axis of the embryo (reviewed in (Becalska and Gavis 2009)).

b) In the budding yeast Saccharomyces cerevisiae, ash1 mRNA localization to the nascent cell regulates mating type determination (Long et al. 1997).

c) In Xenopus laevis oocytes, tissue-type determination is dependent on mRNA localization to the vegetal pole (reviewed in (King, Messitt, and Mowry 2005)).

d) In different mammalian cell types, including fibroblasts (Mili, Moissoglu, and Macara 2008), intestinal epithelia cells (Moor et al. 2017) and neurons, mRNA localization plays pivotal roles in cell polarization, migration and differentiation, as well as axonal growth-cone steering and synaptic plasticity (reviewed in (Buxbaum, Haimovich, and Singer 2015; Holt and Schuman 2013; Sutton and Schuman 2006)).

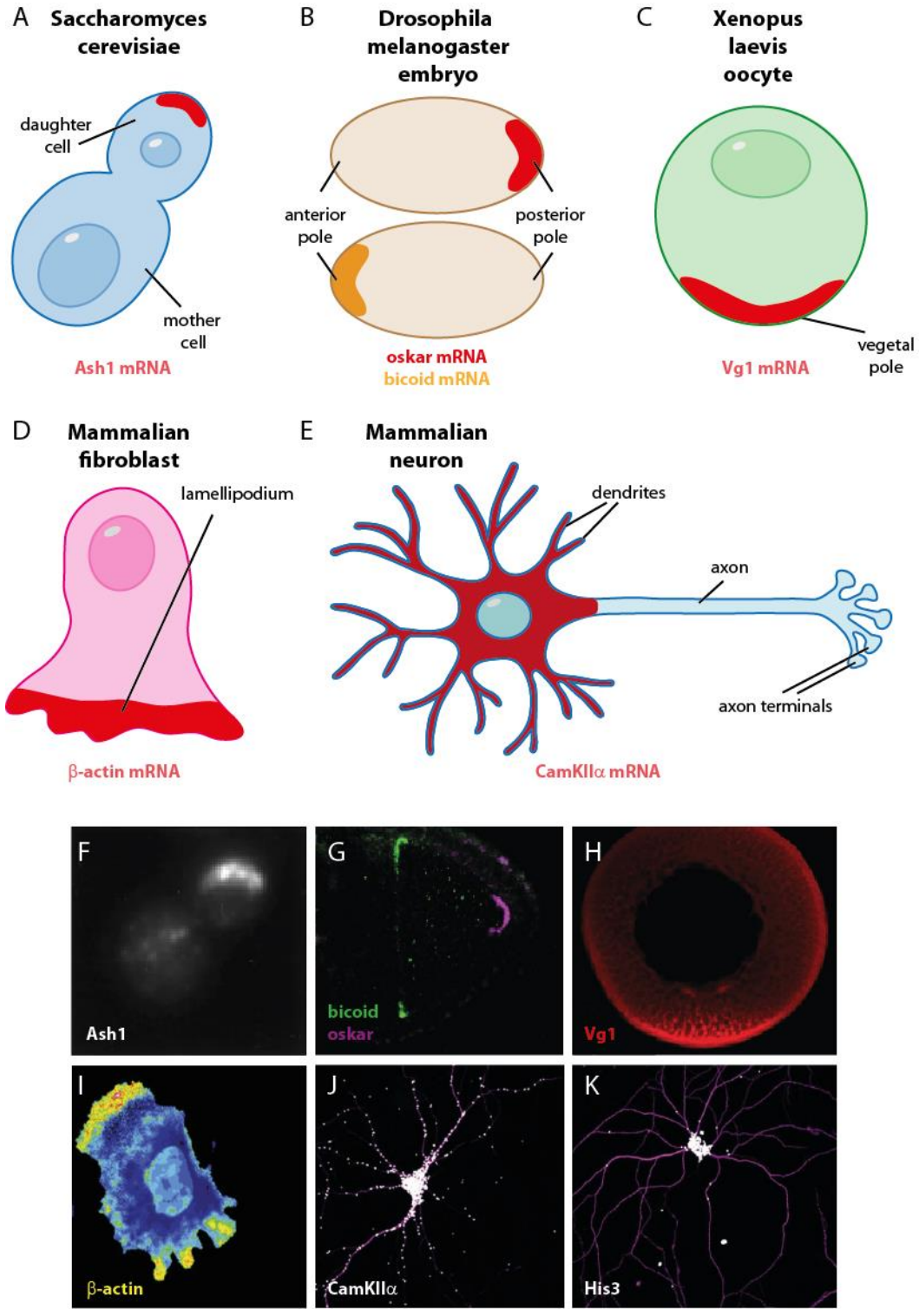

Figure 2: mRNA localization is a conserved mechanism. Examples for mRNA localization in different organisms include **(A)** Ash1 mRNA in the budding yeast Saccharomyces cerevisiae, **(B)** oskar and bicoid mRNAs in the Drosophila melanogaster embryo, **(C)** Vg1 mRNA in the Xenopus

laevis oocyte, **(D)** β-actin mRNA in mammalian embryonic fibroblasts and **(E)** β-actin and CamKIIα mRNAs in mammalian hippocampal neurons. **(F-K)** Microscopy images of different mRNA localization systems: **(F)** Ash1 mRNA in the budding yeast Saccharomyces cerevisiae (image originally from (Long et al. 1997)); **(G)** bicoid and oskar mRNAs in the Drosophila melanogaster oocyte (image originally from (Bullock 2007; Holt and Bullock 2009)); **(H)** Vg1 vegetal localization element RNA in the Xenopus laevis oocyte (image originally from J. Gagnon and K. Mowry (Medioni, Mowry, and Besse 2012)); **(I)** β-actin mRNA in moving mammalian fibroblasts (image originally from (Park et al. 2012)); and **(J-K)** CamKIIα and His3 mRNAs in mammalian hippocampal neurons (image originally from (Fusco et al. 2021)). Whereas CamKIIα mRNA localizes to dendrites, His3 mRNA localizes to the soma.

The localization of mRNAs rather than proteins has several advantages for a cell: (1) it is cost-efficient, as the localization of a single mRNA transcript can result in the translation of over 1,000 protein copies (measured in Escherichia coli (Taniguchi et al. 2011)) in response to local stimuli; (2) local translation of mRNAs at their sites of delivery can lead to the local enrichment of proteins, resulting in the formation of functionalized protein complexes; (3) proteins can have adverse effects in cellular compartments in which they are not intended to localize in; (4) mRNA localization provides an additional layer of temporal regulation, enabling mRNAs to localize to cellular compartments only at a certain developmental stage; and (5) local translation allows for an additional control of protein regulation via specific chaperone-based folding and/or specialized post-translational modifications (PTMs) (reviewed in (Holt and Bullock 2009; Medioni, Mowry, and Besse 2012)).

1.3.2. Multiple mechanisms contribute to mRNA localization

Cells can use different mechanisms to localize mRNAs: (1) diffusion and anchoring, (2) local protection from degradation, and finally (3) active transport (reviewed in (Medioni, Mowry, and Besse 2012; St Johnston 1995)):

1. Diffusing mRNAs can be tethered to subcellular structures or protein complexes to remain in close proximity to sites of local translation. For instance, a cortical actin-based anchoring has been observed for Drosophila melanogaster nanos mRNA (Forrest and Gavis 2003).

2. mRNAs can be protected from RNases or degradation enzymes by localization in a specific compartment. Drosophila melanogaster, for example, uses this mechanism to localize Hsp83 mRNA to the germ plasm in later developmental stages (Ding et al. 1993).

3. Highly polarized cells often make use of active transport along the cytoskeleton to localize transcripts to specific compartments, e.g. β-tubulin mRNA (S.

Baumann et al. 2020; S. J. Baumann et al. 2022) which is transported to axonal growth cones in neurons.

Although all of the aforementioned mechanisms contribute to the asymmetric localization of mRNAs, animal cells primarily rely on active transport of mRNAs along the cytoskeleton. This preference may arise from the likelihood that active transport in animal cells guarantees the fastest and most efficient mechanism of mRNA delivery to sites of local translation (reviewed in (Holt and Bullock 2009)).

1.4. Neuronal mRNA transport

1.4.1. Why do neurons depend on the transport of mRNAs?

Neurons are complex and specialized cells that are characterized by their highly polarized structure. They harbor a variety of functionalized compartments, including the cell body, also known as soma, as well as dendrites (information receivers) and axons (information transmitters). The dendritic and axonal compartments are collectively known as the neuropil which can contain up to 99% of a hippocampal pyramidal neuron's cytoplasm. The axon can grow to a length of hundreds of centimeters, while dendrites are highly branched and can physically extend from the soma by an average length of >10 millimeters (Figure 2(J-K)) (Ishizuka, Cowan, and Amaral 1995).

Intracellular transport plays a fundamental role in the maintenance and function of neurons. The transport of various cellular components, including mitochondria (Henrichs et al. 2020), synaptic ion channels (Barry et al. 2014; Heisler et al. 2014; Nakajima et al. 2012), secretory vesicles (Serra-marques et al. 2020) and mRNAs (S. Baumann et al. 2020; S. J. Baumann et al. 2022) is achieved by motor proteins like kinesin and dynein, utilizing microtubules to deliver their cargoes to precise locations within neuronal compartments.

The transport of mRNAs is of particular importance as it enables neurons to control protein translation in a spatiotemporal manner. By transporting mRNAs to specific subcellular locations, neurons can rapidly respond to external stimuli and build local, specialized protein networks which are implicated in several functions, including dendritic arborization, axonal pathfinding and synaptic plasticity-underlying long-term memory formation (reviewed in (Holt and Schuman 2013)).

Accordingly, the dysregulation of mRNA transport has been connected to neurological disorders like epilepsy (Nakajima et al. 2012) and the fragile X syndrome (Bagni et al. 2012), the most frequent cause of inherited intellectual disability (for further information see (Nobutaka Hirokawa, Niwa, and Tanaka 2010)). Identifying the factors that drive and regulate intracellular mRNA transport is thus of fundamental importance.

1.4.2. The neuronal microtubule cytoskeleton

The proper functioning of mRNA transport in neurons relies on a highly regulated network of cytoskeletal filaments. Besides actin and intermediate filaments, microtubules are a crucial component of the cytoskeletal network as they enable mRNA transport via the microtubule motor proteins kinesin and dynein.

Microtubules are conserved in all eukaryotes and consist of α/β-tubulin heterodimers that polymerize into hollow cylinders. They are canonically composed of 13 protofilaments that are assembled around a hollow core, resulting in rod-like structures that measure a diameter of 25 nm.

Microtubules are structurally polar cytoskeletal filaments whose polarity results from the head-to-tail arrangement of the α/β-tubulin heterodimers in the protofilaments. Whereas β-tubulin is exposed at the microtubule plus end, α-tubulin is exposed at the microtubule minus end. Both microtubule ends are able to grow, however, the plus end is characterized by a faster growth than the minus end (Walker et al. 1988).

A characteristic feature of microtubules is their dynamic instability which was first described in 1984 (Mitchison and Kirschner 1984): Even in an environment with a sufficient concentration of α/β-tubulin heterodimers, microtubules switch stochastically between extended periods of growth and shrinkage. This dynamic property of microtubules is crucial for many neuronal processes such as (1) the dynamic remodeling of the neuropil during development, (2) the guidance of axons to target destinations as well as (3) synaptic plasticity, which is the ability of synapses to adapt in response to activity, and which underlies long-term memory formation (reviewed in (Peña-Ortega, Robles-Gómez, and Xolalpa-Cueva 2022)).

Moreover, microtubules are characterized by their negatively charged surface. The negative charge is caused by the outwards facing C-terminal tails of α- and β-tubulin monomers that are enriched in acidic residues such as glutamic and aspartic acid. These C-terminal tails modulate the affinity of stereospecific interactions of

microtubule-associated proteins (MAPs) with the outer surface of microtubules (reviewed in (Roll-Mecak 2015)). Among a variety of functions in the cell, MAPs can serve as regulators of microtubule dynamics or as motor proteins that are crucial for the transport of mRNAs (reviewed in (Goodson and Jonasson 2018), see section 1.5).

In neurons, the organization of microtubules depends on the specific compartment they are located in. In contrast to axons, where microtubules are organized in a plus-end-out orientation, the polarity in dendrites is mixed, with both plus and minus ends facing outwards (Baas et al. 1988). This enables motor protein-based bidirectional transport of mRNAs from the soma to the periphery (anterograde transport) and from the periphery to the soma (retrograde transport) (Figure 3).

Importantly, there is a “symbiontic” relationship between the cytoskeleton and mRNA in neurons. While the cytoskeleton is fundamental for mRNA transport to the neuropil, it in turn also depends on mRNAs like β2B-tubulin mRNA (S. Baumann et al. 2020; Preitner et al. 2014) for its local remodeling.

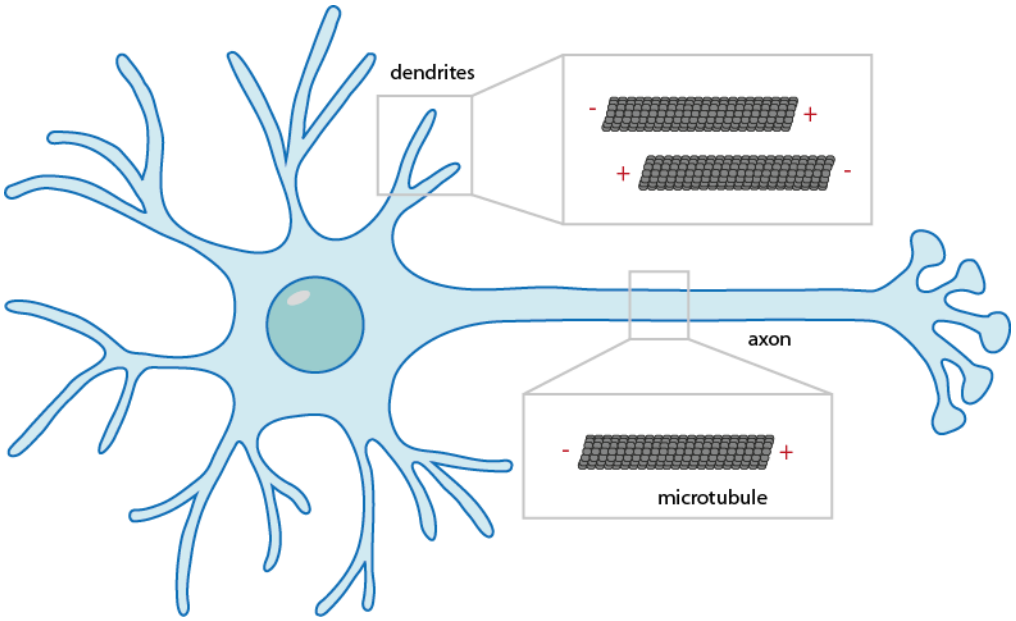

Figure 3: The neuronal microtubule cytoskeleton. In neurons, microtubule polarity differs in axonal and dendritic compartments. Dendritic microtubules show mixed structural polarity, whereas axonal microtubules are unipolar with a plus-end-out organization, allowing both antero- and retrograde transport of mRNA.

1.5. Microtubule motor proteins transport mRNAs

mRNAs are transported along microtubules in the form of messenger ribonucleoprotein (mRNP) complexes via kinesin and dynein (reviewed in (N. Hirokawa 2006)). In the subsequent sections, these two microtubule motor protein families will be introduced, with a specific emphasis on kinesin-1 (Figure 4) which is of particular interest as it serves as the primary motor protein utilized in this thesis.

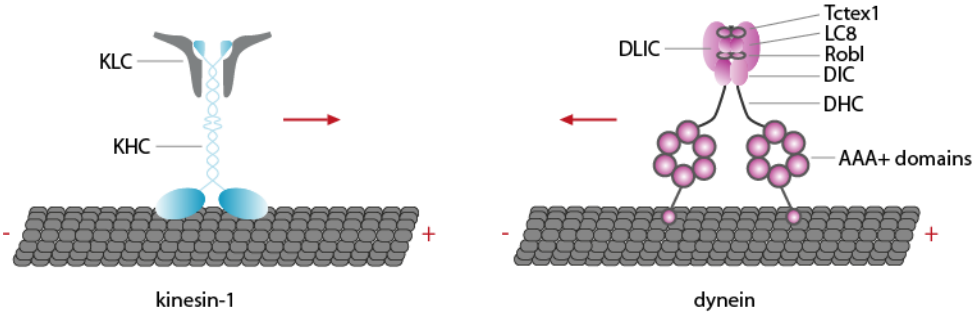

Figure 4: Kinesin-1 and dynein motors. Kinesin-1 and dynein motors transport cargoes along microtubules. Kinesin-1 consists of a heavy chain (KHC) dimer and two identical copies of light chains (KLCs). Like kinesin-1, dynein has two copies of a variety of subunits: the heavy chain (DHC), consisting of six AAA+ domains, the intermediate chain (DIC), the light intermediate chain (DLIC) as well as the three light chains (DLCs) Roadblock (Robl), LC8 and Tctex1. The two motors walk towards opposite ends of microtubules: While kinesin-1 walks to the plus end, dynein walks towards the minus end of microtubules.

1.5.1. Kinesin

Homo sapiens and Mus musculus have a total of 45 genes that encode 14 different classes of kinesin motor proteins. These kinesins can further be classified into three main types of microtubule-dependent motor proteins depending on the location of their motor domain in the polypeptide chain: N-KIFs (N-terminal motor domain), M-KIFs (middle/central motor domain) or C-KIFs (C-terminal motor domain) (Aizawa et al. 1992; Lawrence et al. 2004; Miki et al. 2001). The location of the motor domain confers specific characteristics to the individual kinesin superfamily proteins (KIFs): While N-KIFs move towards the plus ends of microtubules, C-KIFs generally move towards the minus ends of microtubules. In contrast, M-KIFs are adenosine triphosphate (ATP)-dependent microtubule depolymerases. In addition, there are certain kinesins that combine directed motility with a destabilization function as well as those that can crosslink microtubules (reviewed in (Verhey and Hammond 2009)).

Kinesin-1, a highly abundant plus end-directed motor protein, is either present as a dimer, comprising two copies of the kinesin-1 heavy chain (known as KHC or KIF), or as a heterotetramer, consisting of the heavy chain dimer as well as two copies of identical, homologous kinesin-1 light chains (KLCs) (Figure 4) that are encoded by four different genes (KLC1-4). There are three homologous KHC proteins (KIF5A, KIF5B and KIF5C) in mammals which resulted from gene duplication and subsequent diversification events (Miki et al. 2001). They differ in their expression patterns: Whereas KIF5B is ubiquitously expressed, KIF5A and KIF5C are neuron-specific. Mutations in them accordingly result in neurodegenerative and neurodevelopmental pathologies (Crimella et al. 2012; Nicolas et al. 2018; Poirier et al. 2013; Reid et al. 2002; Willemsen et al. 2014).

KHCs are characterized by an N-terminal motor domain, a stalk region and a tail. Whereas the stalk region is crucial for heavy chain dimerization, the tail region is responsible for directly binding cargoes (reviewed in (Nobutaka Hirokawa, Niwa, and Tanaka 2010; Verhey and Hammond 2009)) as well as complex formation with kinesin-1 light chains.

In contrast, the motor domain binds to microtubules and simultaneously functions as an ATPase that enables motility. The motility of kinesin-1 depends on the dimerization of two heavy chains: Release of adenosine diphosphate (ADP) and phosphate subsequent to adenosine triphosphate (ATP) hydrolysis enables the dissociation of one of the two motor domains from the microtubule, whereas the second motor domain remains attached to the lattice (reviewed in (Lee Sweeney and Holzbaur 2018)). A key factor in this process is a short neck-linker element in the C-terminus of the motor domain. A nucleotide-dependent conformational change of this element from a docked to an undocked state (Rice et al. 1999), together with the intramolecular strain generated during active translocation, creates an alternating step-wise movement of the kinesin-1 heavy chain dimers towards the microtubule plus end (Clancy et al. 2011; Milic et al. 2014; Rice et al. 1999; Rosenfeld et al. 2003; Yildiz et al. 2008). The energy from one ATP molecule ultimately results in an 8 nm step (Schnitzer and Block 1997) along the microtubule, which corresponds to the distance between two neighboring tubulin monomers in the microtubule lattice (reviewed in (Herrmann and Aebi 2016)).

Kinesin-1 light chains comprise an N-terminal heptad repeat domain, a tetratricopeptide repeat as well as a C-terminal domain. Whereas the heptad repeat domain is responsible for KHC binding, the tetratricopeptide repeat and C-terminal domains bind to cargoes that are to be transported by kinesin-1 (Pernigo et al. 2013).

In neurons, kinesin-1 plays a crucial role in neuronal function by facilitating the intracellular transport of a wide range of cellular components, including motor proteins (Twelvetrees et al. 2016), mitochondria (Henrichs et al. 2020), synaptic ion channels (Barry et al. 2014; Heisler et al. 2014; Nakajima et al. 2012), secretory vesicles (Serra-marques et al. 2020) and mRNAs (S. J. Baumann et al. 2022; Brendel et al. 2004; Dictenberg et al. 2008; Kanai, Dohmae, and Hirokawa 2004; Mallardo et al. 2003).

In its cargo-free state, however, kinesin-1 is autoinhibited. The autoinhibition comprises contributions of the KHCs as well as the KLCs. KHCs are proposed to be inhibited via an intramolecular interaction between their motor and tail domains (Coy et al. 1999; Dietrich et al. 2008; Friedman and Vale 1999; Kaan, Hackney, and Kozielski 2011; Stock et al. 1999). This interaction is enabled via an isoleucine/alanine/lysine motif in the tail domain (Hackney and Stock 2000; Kaan, Hackney, and Kozielski 2011) as well as a hinge region in the KHC coiled coil stalk domain, resulting in a folding of the KHCs that inhibits their movement along microtubules. Similarly, complex formation with KLCs decreases both binding to microtubules and motility (Friedman and Vale 1999; Verhey et al. 1998). KLCs are either suggested to help maintain the KHC-based autoinhibited state (Cai et al. 2007; Friedman and Vale 1999; Verhey et al. 1998) or are proposed to have a KHC-independent autoinhibition mechanism via an intramolecular interaction between the tetratricopeptide repeat domain and an unstructured region next to it, partially occluding the KLC tryptophan-acidic motif. Cargo binding to this motif is finally proposed to relieve this autoinhibitory interaction, resulting in an overall conformational change of the KLCs (Yip et al. 2016). Newer studies suggest that kinesin-1 motors are only fully activated by an interplay of cargo binding to the KLC and recruitment of the KHCs to microtubules via microtubule-associated protein 7 (MAP7). Besides affecting kinesin-1 landing rate, MAP7 is described to prevent the dissociation of kinesin-1 through transient interactions at the surface of microtubules (Chiba et al. 2022; Ferro et al. 2022; Hooikaas et al. 2019; Monroy et al. 2018).

1.5.2. Dynein

Besides kinesin, dynein represents the other family of microtubule motor proteins. It consists of dynein-1 and dynein-2, which are responsible for cargo transport along microtubules in the cytoplasm or in cilia (Paschal 1987; Paschal and Vallee 1987; Pazour et al. 1999; Porter et al. 1999), respectively. Like kinesin-1, cytoplasmic dynein-1 (hereafter referred to as dynein) transports a variety of cellular cargoes along microtubules, including organelles, vesicles, proteins and mRNAs (Aniento et

al. 1993; Bremner et al. 2009; Pilling et al. 2006; Sanghavi et al. 2013; Sladewski et al. 2018).

Dynein is a large protein complex (~1.4 MDa) which is composed of six subunits that are present in two copies each: the dynein heavy chain (DHC), the intermediate chain, the light intermediate chain as well as the light chains Roadblock, LC8 and Tctex1. The DHC is comprised of a C-terminal domain as well as an N-terminal tail domain. The C-terminal domain consists of a microtubule-binding domain and a motor domain. The latter comprises a ring of six AAA+ domains as well as a linker between the ATP-hydrolyzing AAA1 with the cargo-binding heavy chain tail, which are both important for dynein motility towards the microtubule minus end (Figure 4). The heavy chain tail is responsible for connecting the heavy chain with the intermediate, light intermediate and light chains. These non-catalytic subunits of dynein are involved in cargo recruitment and binding to adaptor proteins (reviewed in (Reck-Peterson et al. 2018)).

In contrast to kinesin-1, dynein is a minus end-directed motor protein (Schroer, Steuer, and Sheetz 1989) which transports neuronal cargoes either in a retrograde fashion from axons to the soma or in a bidirectional fashion in dendrites, consistent with microtubule polarity in these neuronal compartments (Figure 3).

The motility of dynein depends on the combined action of the dimerization of its heavy chain, ATP hydrolysis-dependent conformational changes in the AAA+ ring, as well as bending and straightening of the AAA1-tail linker. ATP binding to the AAA1 domain induces a conformational change, resulting in a weak binding state of dynein which is characterized by the dissociation of one of the two microtubule-binding domains from the microtubule lattice as well as bending of the linker. For the unbound microtubule-binding domain, ATP hydrolysis results in weak rebinding to the microtubule, which is further enhanced upon the release of phosphate. This power stroke results in the straightening of the linker, pulling the tail domain and associated cargo towards the new binding site on the microtubule lattice. Finally, upon the release of ADP, a new cycle of movement is initiated (Lin et al. 2014).

Since dynein is autoinhibited in a cargo-less state, it requires the combined action of its accessory protein complex dynactin as well as an adaptor like protein Bicaudal D2 to ensure its activation, allowing it to deliver cargoes in neurons (McKenney et al. 2014a; Schlager, Hoang, et al. 2014).

Ultimately, the dysregulation of dynein-based transport has been proposed to be of functional relevance concerning several neurological disorders, including the

Parkinson disease-like Perry syndrome, spinal muscular atrophy with lower extremity predominant and hereditary motor neuron disease (reviewed in (Lipka et al. 2013)).

1.6. The drivers of neuronal mRNA localization: RBPs and 3'UTRs

1.6.1. RBPs and zip codes

In line with their high polarity and compartmentalization, neurons possess thousands of localized mRNAs (Cajigas et al. 2012; Gumy et al. 2011; Middleton, Eberwine, and Kim 2019; Zivraj et al. 2010). Despite the abundance of localized mRNAs, the sorting and distribution of these transcripts primarily rely on a limited set of motor proteins. Taking into account that individual transport complexes only harbor one to four copies of mRNAs (S. Baumann et al. 2020; Park et al. 2014; Turner-Bridger et al. 2018), neurons require a specificity factor that recruits these small and defined packages of mRNAs to microtubule motor proteins, priming them for transport to their final destinations in the cell.

Besides motor proteins, mRNA localization therefore additionally depends on specific RNA-binding proteins (RBPs) that form mRNPs with individual mRNAs. The latter control various aspects of an mRNA's life, such as stability, localization and translation. To guide mRNAs to their final location, RBPs interact with short, conserved localization sequences predominantly located in 3'UTRs of mRNA transcripts, also known as zip codes (reviewed in (Buxbaum, Haimovich, and Singer 2015; Chabanon, Mickleburgh, and Hesketh 2006; Martin and Ephrussi 2009)). RBPs recognize these motifs in a sequence-specific manner and/or via a defined secondary structure, hence they serve as adaptors between mRNAs and motor proteins (Figure 5), controlling the precise targeting and localization of a given mRNA in a neuronal cell (for a recent summary of known RBP/zip code pairs see (Engel et al. 2020)).

A well-known example of such a motor/adaptor/zip code system can be found in Drosophila melanogaster: Several localized mRNAs containing the zip code TLS interact with the dynein/dynactin complex via the adaptor proteins Egalitarian and Bicaudal-D (Dienstbier et al. 2009; Goldman et al. 2019).

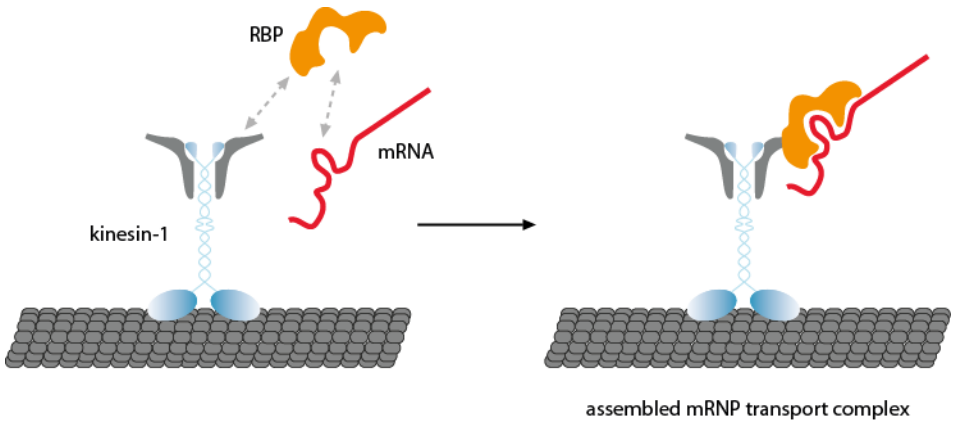

Figure 5: Assembly of an mRNP transport complex. RBPs serve as adaptors between mRNAs and motor proteins by recognizing specific zip codes – short sequence- or structure-based elements in the 3'UTR of an mRNA. The here shown example illustrates the specific recognition of a secondary structure in the 3'UTR of an mRNA via an RBP.

Nonetheless, the currently identified zip code/RBP/motor systems are insufficient to explain the motor protein-dependent localization of thousands of mRNA transcripts in neurons. Further research is crucial to elucidate the mechanisms through which neurons coordinate the precise targeting of thousands of mRNA transcripts, thereby ensuring their translation at the correct place and time, which ultimately enables long-term memory formation.

1.6.2.3'UTR length: A novel localization mechanism?

Recently, the length of the 3'UTR itself has been suggested to serve as an additional mRNA localization mechanism besides the well-known zip code system (Middleton, Eberwine, and Kim 2019; Taliaferro et al. 2016; Tushev, Glock, Heumüller, et al. 2018).

In addition to a general increase in 3'UTR length within the neuronal tissue, neurons are uniquely known to have a high diversity of 3'UTR isoforms (Miura et al. 2013; Tushev, Glock, Heumüller, et al. 2018) resulting from alternative cleavage and polyadenylation. This mechanism, which is estimated to affect around 70% of human mRNAs (Derti et al. 2012), regulates processes such as cellular proliferation, tumorigenicity as well as synaptic plasticity (reviewed in (Tian and Manley 2016)). It comprises two processes: (1) the endonucleolytic cleavage of the nascent mRNA chain during splicing, and (2) the non-templated addition of adenosines (polyA tails) to an mRNA's 3'end. Both processes lead to the generation of alternative 3'UTRs. Splicing influences 3'UTR identity via the generation of alternative last exons, while

most polyadenylation sites can be found in the 3'UTR, leading to isoforms differing in length (also known as tandem 3'UTRs) that are identical in their overlapping regions. Constitutive 3'UTRs thereby consist of the region upstream of the first or proximal polyadenylation site, whereas alternative 3'UTRs arise from the usage of distal polyadenylation sites.

Different 3'UTR isoforms, owing to the absence or presence of regulatory elements (e.g. zip codes/RBP motifs), fulfill different cellular functions and can influence mRNA stability, nuclear export, and subcellular localization. An mRNA's localization is ultimately also able to regulate local translation, as for example for the short and long 3'UTR isoforms of brain-derived neurotrophic factor (BDNF) mRNA, whose localization pattern differs: the former is restricted to the soma, whereas the latter is localized to and translated in dendrites (An et al. 2008).

Recently, the analysis of 3'UTR isoforms and their alternative localization has expanded beyond individual examples like BDNF mRNA. Genome-wide analyses have examined this diversity in brain-derived cell lines (Taliaferro et al. 2016), primary mouse hippocampal neurons (Middleton, Eberwine, and Kim 2019) as well as rat hippocampal slices (Tushev, Glock, Heumüller, et al. 2018). These studies focused on the separation of somatic and neuropil compartments as well as 3'end sequencing of the separate mRNA samples, showing that alternative localization of distinct 3'UTR isoforms is a widespread phenomenon.

Strikingly, two groups recently identified that neuropil-enriched mRNA transcripts have significantly longer 3'UTRs than soma-enriched mRNAs (Middleton, Eberwine, and Kim 2019; Tushev, Glock, Heumüller, et al. 2018) (Figure 6A), whereas non-localized mRNAs are characterized by the shortest 3'UTRs. The differential localization of short vs. long 3'UTRs was exemplified for rat CamKIIα mRNA (Tushev, Glock, Heumüller, et al. 2018). The latter is a highly abundant mRNA in the neuropil (Cajigas et al. 2012; Middleton, Eberwine, and Kim 2019) which codes for the alpha isoform of calcium/calmodulin-dependent protein kinase II, a protein that is crucial for synaptic plasticity and long-term memory formation (Yasuda, Hayashi, and Hell 2022; Zalcman, Federman, and Romano 2018). Strikingly, CamKIIa mRNA is characterized by three tandem 3'UTRs of varying lengths, of which only the longest 3'UTR isoform drives localization of the corresponding transcript to distal regions of dendrites. In contrast, the shorter 3'UTR isoforms restrict its localization to the soma or to proximal regions of dendrites (Tushev, Glock, Heumüller, et al. 2018) (Figure 7).

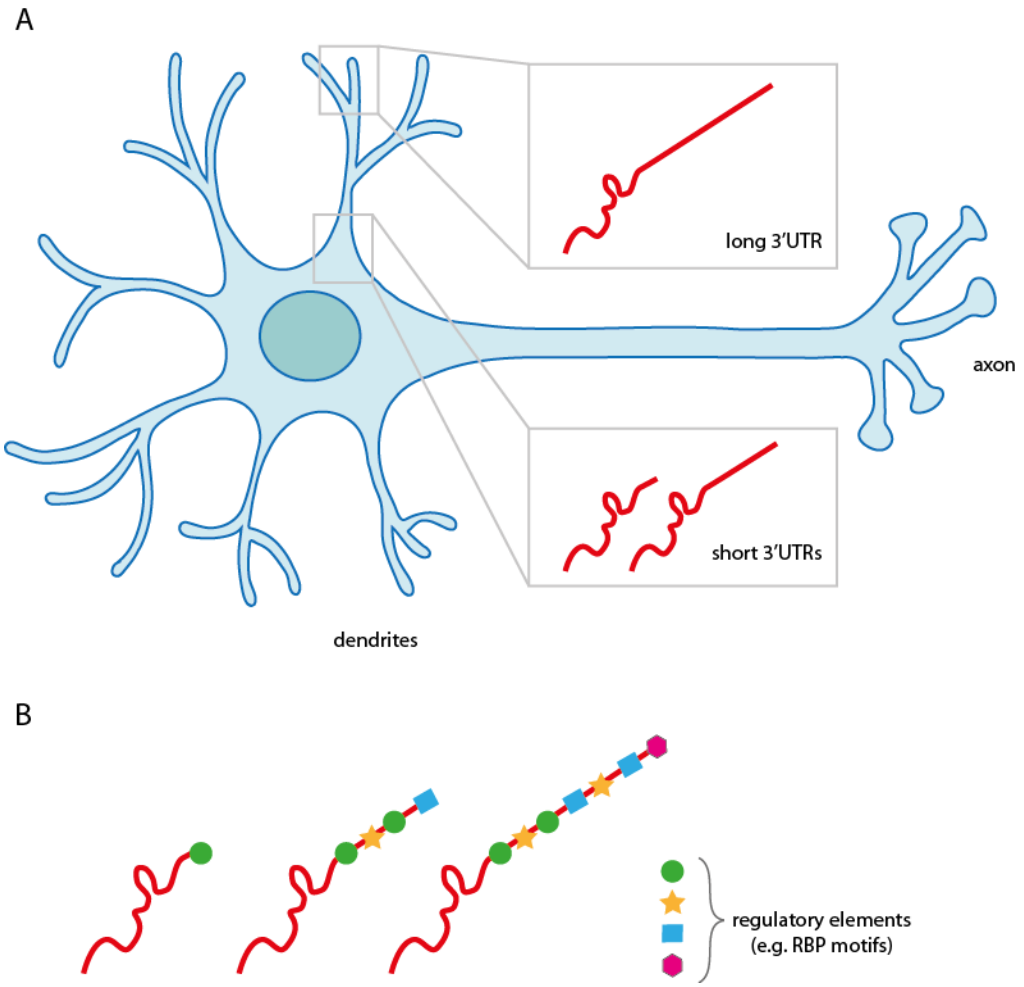

Figure 6: mRNAs are sorted according to 3'UTR length. (A) Tandem 3'UTR isoforms, resulting from differential polyadenylation site selection, are localized to distinct parts of a neuron. Long 3'UTR isoforms localize to distal regions of dendrites, whereas shorter 3'UTR isoforms localize to the soma or proximal regions of dendrites. **(B)** Longer 3'UTR isoforms are not only characterized by novel regulatory elements, but also by repetitive elements that are already present in shorter 3'UTRs.

Interestingly, the Schuman group also looked at the presence of regulatory elements such as RBP motifs in tandem 3'UTR isoforms. While longer isoforms comprise a high number of novel regulatory elements, they also harbor elements that are already present in shorter isoforms. Strikingly, the number of novel elements is lower than expected by chance, whereas the number of repeated elements is higher than expected by chance. Taken together, both the identity and quantity of a specific motif in 3'UTRs of differing length might be crucial factors that determine the localization of a given mRNA transcript (Tushev, Glock, Heumüller, et al. 2018) (Figure 6B).

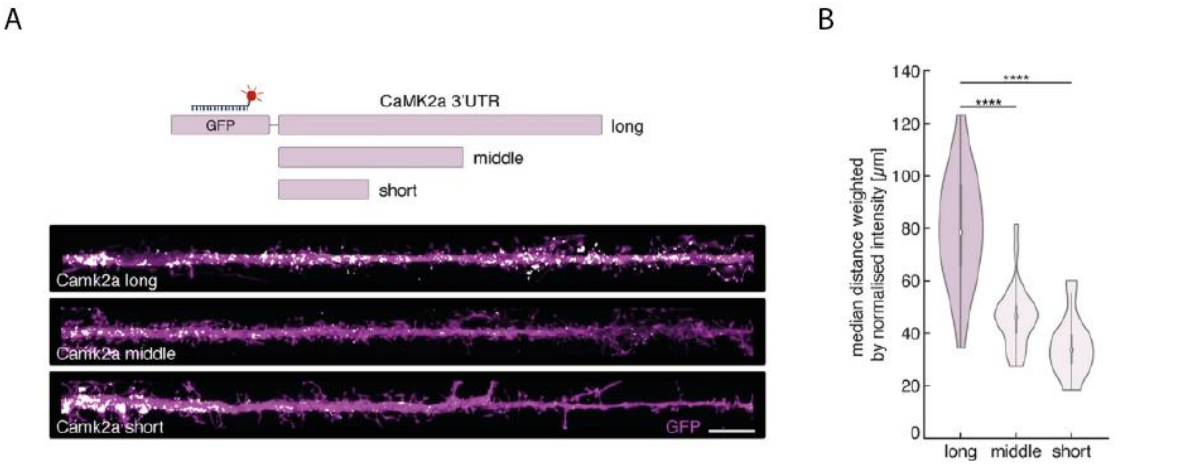

Figure 7: CamKIIα 3'UTR isoforms show distinct localization patterns in neurons. (A) Reporter constructs were generated for the three different tandem 3'UTRs of CamKIIα that were fused to the coding sequence of green fluorescent protein (GFP). Fluorescence in situ hybridization was perfomed for GFP. The image shows dendrites of transfected neurons growing from left (soma, proximal) to right (neuropil, distal). Purple: GFP; White: CamKIIα mRNA. Scalebar: 10 µm. **(B)** Violin plots showing the distance from the soma for the mRNA localization signal of different CamKIIα 3'UTR isoforms. Image adapted from (Tushev, Glock, Heumüller, et al. 2018).

1.7. Methods used to determine neuronal mRNP compositions

Despite decades of research on mRNA transport and localization, the exact mechanisms by which neuronal mRNAs are connected to cellular transport machineries remain unknown. One significant challenge is the lack of techniques that are capable of precisely determining the composition and architecture of neuronal mRNA transport complexes while simultaneously isolating the specific functions of individual factors within these complexes from any pleiotropic effects (see section 1.7.1).

In the first publication resulting from this thesis, we condensed the published findings of the past few decades into a network to visualize those few minimal neuronal mRNP transport complexes that are known to date and that are supported by substantial evidence (Figure 8). The network shows interactions between microtubule motor proteins, RBPs and target mRNAs that were identified in low-throughput biochemical studies. We exclusively focused on those interactions which constitute an entire mRNP transport complex consisting of at least one motor protein, one RBP and one mRNA for which a specific binding sequence (zip code) has been identified. We further weighed the evidence for individual interactions based on (1) the type and quantity of methods which were used to determine them, (2) whether

these interactions are direct or indirect, and finally added information on the binding strength whenever available (Rodrigues et al. 2021).

We defined direct interactions as those that result from (1) yeast-2-hybrid assays (see section 1.7.2), (2) co-immunoprecipitation (co-IP)/pull-down experiments using purified components, (3) reconstituted complexes (see section 1.7.3), (4) isothermal calorimetry, (5) surface plasmon resonance, (6) electrophoretic mobility shift assays, (7) nuclear magnetic resonance, (8) microscale thermophoresis, (9) individual nucleotide resolution – cross-linking immunoprecipitation (iCLIP) and (10) size exclusion chromatography – multiangle light scattering. In contrast, methods reporting indirect interactions typically comprise RNA-IP, co-IP, co-fractionation, and pull-down experiments performed using cell lysates (see section 1.7.1).

Strikingly, as visualized by the dotted lines in Figure 8, many of the interactions shown for the proposed mRNP transport complexes result from indirect evidence. Thus, after decades of research in the neuronal mRNA transport field, to date only a handful of proposed mRNP transport complexes are supported by substantial, more direct evidence. These are visualized by solid lines (Figure 8) and have recently been expanded by a kinesin-1-based mRNP transport system (S. J. Baumann et al. 2022) (Figure 8).

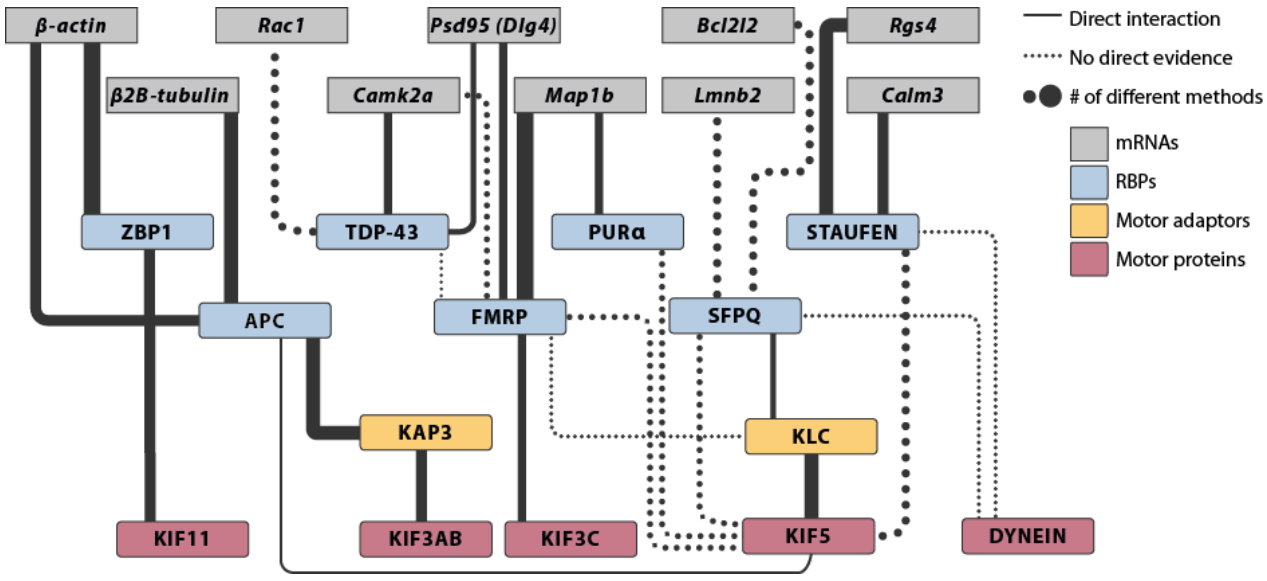

Figure 8: Known interactions between motor proteins, motor adaptors, RBPs and mRNAs. Cytoscape (Cline et al. 2007) network showing interactions between motor proteins, motor adaptors, RBPs and mRNAs described in the literature. The network is restricted to data from low-throughput studies, and only those mRNA interactions for which an RBP motif (zip code) is described are shown.

Continuous lines indicate direct interactions between individual factors, whereas dotted lines refer to interactions based on indirect evidence. The line width gives insights on the number of methods used to describe an individual interaction. Different colors refer to different identities of mRNA transport complex components: motor proteins (red), adaptor proteins (yellow), RBPs (blue) and RNAs (gray). Image adapted from (Rodrigues et al. 2021).

1.7.1. Previous methods and their limitations

In the past, many studies have aimed at determining the architecture and composition of mRNA transport complexes using the following methods: (a) the overexpression or knockdown of proteins, (b) imaging techniques, and (c) affinity purification coupled with mass spectrometric analyses (reviewed in the first publication resulting from this thesis (Rodrigues et al. 2021)). Despite providing useful information on proteins potentially involved in mRNA transport and localization, these methods have limitations which will be discussed below:

(a) Overexpression and knockdown approaches

Formerly, microtubule motor proteins and RBPs were often overexpressed or knocked down to investigate their potential involvement in mRNA transport. However, an important challenge of this approach is isolating the effect of a certain protein on mRNA transport from any pleiotropic effect this protein may have in the cell. For example, fragile X mental retardation protein (FMRP), one of the best-known mRNA-transporting RBPs (Dictenberg et al. 2008; Goering et al. 2020), also regulates nuclear processes (Shah et al. 2020), nuclear mRNA export (Edens et al. 2019; Zhang, Wang, and Huang 2007), and translation regulation (Feng et al. 1997). Furthermore, microtubule motor proteins transport a variety of cargoes besides mRNPs, including other motor proteins (Twelvetrees et al. 2016), mitochondria (Henrichs et al. 2020), axonal and synaptic ion channels (Barry et al. 2014; Heisler et al. 2014; Nakajima et al. 2012), and secretory vesicles (Serra-marques et al. 2020). Thus, the overexpression or knockdown of either class of proteins inevitably affects several cellular processes besides a potential function in mRNA transport. Therefore, the observed phenotypes cannot always be attributed to mRNA transport.

(b) Imaging approaches

Another commonly used method to study mRNA transport involves determining whether microtubule motor proteins, RBPs, and mRNA show co-localization in imaging approaches (Buxbaum et al. 2015). Although giving insights on mRNA transport dynamics, this approach presents both technical and biological challenges. The limited resolution of an optical microscope makes it difficult to

demonstrate direct interactions between individual proteins and mRNAs, as lower resolutions may result in the co-localization of these components by chance (Eliscovich, Shenoy, and Singer 2017). Moreover, an mRNA likely carries many RBPs that remain attached to it during its export, processing, translation, and decay (reviewed in (Müller-McNicoll and Neugebauer 2013)), fulfilling a multitude of functions that are not necessarily required for the transport of a given mRNA, often leading to a false association of these proteins with mRNA transport and localization. Ultimately, imaging approaches can thus show which proteins are trafficked together with mRNAs, but cannot identify the precise factors responsible for mRNA transport

(c) Affinity purification & mass spectrometric analyses

Affinity purification coupled with mass spectrometric analyses represents an alternative approach to determine mRNP composition, which typically yields a high number of target protein interactors. This method, which comprises co-IP and pull-down approaches, has several limitations. For instance, it may not capture transiently interacting proteins and may instead favor strongly binding interactors, leading to a biased list of interactors (Richards, Eckhardt, and Krogan 2021). Additionally, this method cannot differentiate between direct protein-protein interactions and protein-RNA-protein interactions: Often, co-immunoprecipitation and pull-down experiments are performed in the absence of RNase, resulting in the pull-down of several proteins that interact with a target protein via protein-RNA-protein interactions rather than direct protein-protein interactions. As a result, many pulled-down complexes are either sensitive to RNase treatment or are directly performed in the presence of RNase inhibitors (J. F. Chu et al. 2019; Dictenberg et al. 2008; Fukuda et al. 2021; Kanai, Dohmae, and Hirokawa 2004; Mallardo et al. 2003).

1.7.2. rec-YnH: a novel approach overcomes previous limitations

To address the aforementioned constraints, it is essential to employ methods reporting direct protein-protein interactions rather than protein-RNA-protein interactions. Such approaches are fundamental in understanding the minimal components that are required for a given mRNA to be transported.

One of the main methods used for the detection of direct protein interactions is yeast-2-hybrid (Y2H) (Fields and Song 1989). The method (Figure 9A) relies on the expression of a reporter gene that is activated via the binding of a transcription factor. The latter consists of (1) an activation and (2) a DNA-binding domain, which are

independently fused to two proteins (bait and prey) for which an interaction is to be analyzed. The transcription of the reporter gene is only possible if the activation and binding domains are in close proximity to one another, which is dependent on an interaction between the bait and prey proteins. However, this protein-fragment complementation approach is time-consuming and labor-intensive, restricting it to the analysis of a smaller set of potential target protein interactors.

To overcome the latter, the Maurer group has recently developed a novel high-throughput, many-by-many screening approach (recombination yeast-n-hybrid, rec-YnH) (Figure 9C) (Yang et al. 2018), which is based on the yeast-2-hybrid system, in order to identify direct interactions between neuronal microtubule motor proteins and RBPs that may account for functional mRNP transport complexes. In contrast to the yeast-2-hybrid method, which can only be used to test the interaction of a small set of bait and prey proteins at a time, rec-YnH makes use of homologous recombination in yeast in order to efficiently assemble entire bait-prey fusion libraries. This enables the screening of >1 million possible interactions (thousands of bait proteins x thousands of prey proteins). Instead of interaction selection in thousands of plates, as would be the case for yeast-2-hybrid, rec-YnH utilizes liquid-gel culturing for interaction selection. This technique comprises the embedding of individual sets of potential protein interactors within a liquid growth medium. It is commonly used for many-by-many screenings, as it allows the analysis of multiple samples in a single experiment. Interaction partners are subsequently read-out via next-generation sequencing analysis, resulting in protein-protein interaction matrices (Figure 9C).

To validate the obtained rec-YnH results, the Maurer group additionally analyzed selected interactions via the low-throughput NanoBRET (Machleidt et al. 2015) screening approach (unpublished data). The latter is based on bioluminescence resonance energy transfer (BRET) between two fluorophore-linked proteins that are in close proximity to each other (Figure 9B). It is thus complementary to the yeast-2-hybrid method and likewise useful for the analysis of a small set of proteins. Whereas rec-YnH detects interactions in yeast nuclei, the NanoBRET approach detects interactions in the cytoplasm of yeast or mammalian cells. This is an important difference between the two screening approaches, as the focus of this thesis lies on interactions occurring in the cytoplasm, where microtubules and microtubule motor proteins reside.

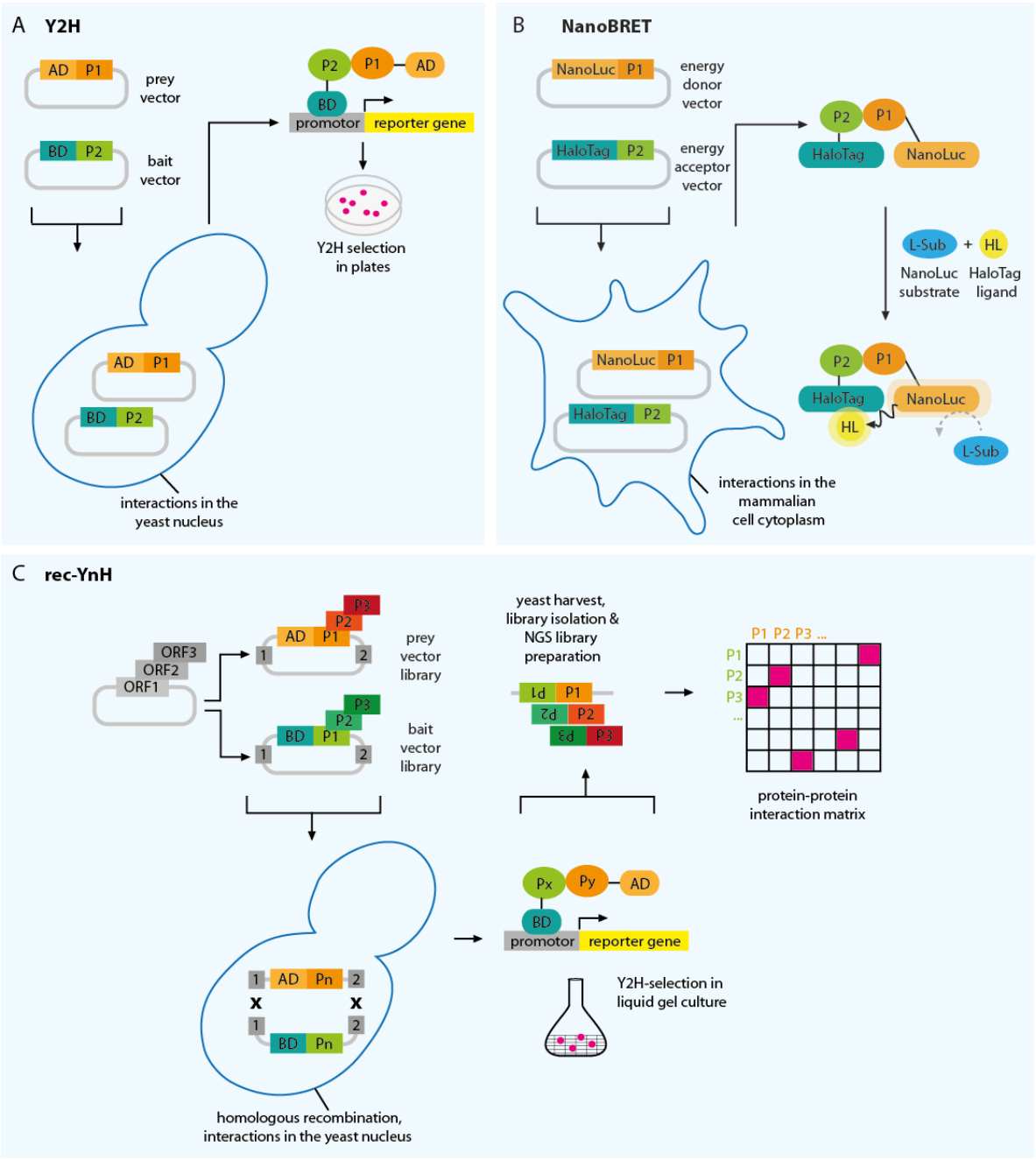

Figure 9: Methods used to detect direct protein-protein interactions. (A) Yeast-2-hybrid (Y2H) is a low-throughput method that relies on the expression of a reporter gene that is activated via the binding of a transcription factor. The latter consists of an activation domain (AD) and a DNA-binding domain (BD), which are independently fused to two proteins (prey and bait, P1 and P2) for which an interaction is analyzed. The transcription of the reporter gene is only possible if the activation and binding domains are in close proximity to one another, which is dependent on an interaction between the prey and bait proteins. **(B)** The low-throughput NanoBRET method utilizes bioluminescence resonance energy transfer (BRET) between two proteins that are fused to fluorophores. Protein 1 (P1) is linked to Nanoluciferase (NanoLuc), while protein 2 (P2) is linked to a HaloTag. When P1 and

P2 interact in the presence of the NanoLuc substrate and HaloTag ligand, the energy transfer from the energy donor (NanoLuc) to the energy acceptor (HaloTag) is enabled. **(C)** rec-YnH is a yeast-2-hybrid-based, high-throughput method to determine direct protein-protein interactions. A large set of open reading frames (ORFs) of the human genome (ORF1, ORF2, ORF3, etc.) is transferred into rec-Y2H screening vectors, creating bait and prey vector libraries that are co-transformed into yeast. Via homologous recombination in yeast, these libraries are fused to generate bait-prey fusion libraries. Interaction selection is performed in liquid gel cultures, and interactions are read out via next-generation sequencing (NGS) analysis, resulting in protein-protein interaction matrices (interactions are indicated in pink).

By validating *selected* rec-YnH interactions using the NanoBRET approach, potential false-positive hits are minimized. The combination of both screening methods thus offers valuable insights into the type of interactions that may be involved in forming functional mRNP complexes.

1.7.3. In vitro reconstitution approaches

Although rec-YnH and NanoBRET screening approaches provide crucial information on direct interactions between motor proteins and RBPs, it is important to reconstitute the proposed mRNP transport complexes to rule out any false positive hits.

One way to do so would be by incubating the individual components with one another and performing gel filtration analyses. Although this method gives insights on interactions within the proposed mRNP transport complexes, high concentrations of individual components are required, weak interactions between them could potentially be missed, and only the average behavior of assembled complexes is represented, as the composition and stoichiometries of potential subcomplexes might not be detected. Furthermore, this method does not provide any information on the transport properties of the assembled complexes.

In contrast, total internal reflection fluorescence microscopy (TIRF-M)-based in vitro reconstitution approaches represent a single-molecule method which (1) requires concentrations in the picomolar-range, (2) can detect stoichiometries of fully assembled mRNP transport complexes as well as subcomplexes, and (3) reports transport properties of the reconstituted mRNP transport system. Importantly, it can be used to prove which *minimal* set of proteins is necessary and sufficient to form a functional mRNP transport complex. In vitro reconstitution approaches have certain advantages over other biochemical methods as well as in vivo imaging approaches (see section 1.7.1), as they provide the precise control over (1) the presence/absence of all system components, (2) the concentrations of individual system components, and (3) a full characterization of the reconstituted system,

including velocities, distances traveled as well as particle sizes and oligomerization states of individual components and fully assembled mRNP complexes.

In the past, this method has been commonly used to analyze microtubule-associated protein (transport) properties (Belyy et al. 2016; Bieling et al. 2010; Chiba et al. 2022; Henrichs et al. 2020; Hooikaas et al. 2019; Maurer et al. 2012; McKenney et al. 2014b; Monroy et al. 2018; Reddy et al. 2016; Schlager, Hoang, et al. 2014; Trokter, Mücke, and Surrey 2012; Twelvetrees et al. 2016). Importantly, the method has also been adapted to investigate mammalian, fly and yeast mRNP transport systems (S. Baumann et al. 2020; S. J. Baumann et al. 2022; Gáspár et al. 2023; Heym et al. 2013; McClintock et al. 2018; Sladewski et al. 2013).

TIRF-M-based in vitro reconstitution approaches usually encompass the immobilization of one component of a given system, with other components of the system added in solution to study their interaction with the immobilized component (Bieling et al. 2010). The immobilized component can either be (1) a specific motor protein in order to measure its velocity in microtubule gliding assays, or (2) microtubules in order to study the dynamics of interacting proteins, including MAPs, motor proteins and mRNP transport complexes.

To meet the specific requirements of studying mRNP transport mechanisms and properties, we adapted existing protocols (Bieling et al. 2010) to develop a suitable TIRF-M-coupled in vitro reconstitution approach (Figure 10) which is described in detail in the second publication resulting from this thesis (Grawenhoff, Baumann, and Maurer 2022)). The approach is based on the immobilization of microtubules and the analysis of motor protein, MAP, RBP/mRNA component interactions and transport properties on the microtubule lattice. It represents one of the main methods used in this thesis, and ultimately provides us with the means to study how purified and fluorescently labeled, recombinant proteins and mRNA (or RNA fragments) come together at the single-molecule level in the context of mRNA transport.

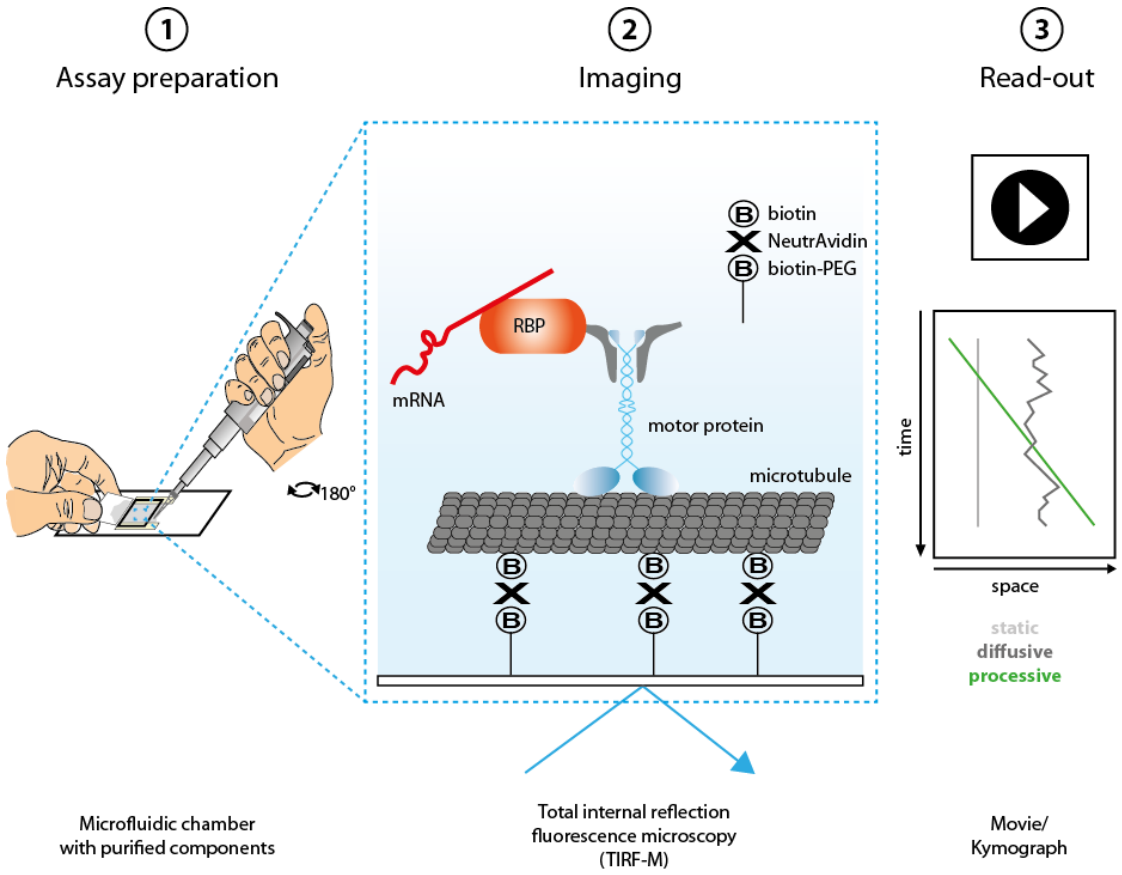

Figure 10: TIRF-M-coupled in vitro reconstitution assay. ~10 µl channels are prepared by attaching biotin-polyethylenglycol (biotin-PEG) coverslips to glass slides with two parallel strips of double-sided tape. Microtubules are assembled in vitro via polymerization of wild type, biotinylated and fluorescently labeled tubulin. They are stabilized and subsequently attached to the coverslips via NeutrAvidin, a deglycosylated avidin that has four biotin binding pockets. A solution containing motor proteins, RBPs and mRNA (or RNA fragments) is then flushed into the channel using a piece of Whatman® paper. TIRF-M allows to visualize the interactions of these system components in close proximity to microtubules. Figure adapted from (Grawenhoff, Baumann, and Maurer 2022).

1.8. rec-YnH network: NXF1 and SRSF3 interact with motor proteins

The rec-YnH screening approach (Yang et al. 2018) revealed numerous novel interactions between microtubule-associated and RNA-binding proteins not found in the existing literature. While some proteins show very few and selective interactions with other proteins, others are hubs for protein interactions, such as the major nuclear export factor (NXF1) of mRNA.

Strikingly, rec-YnH identifies a previously unknown interaction between NXF1 and light chains of both kinesin-1 and dynein, namely the kinesin-1 light chain 4 (KLC4) as well as the dynein light chain Tctex1 (unpublished rec-YnH screen data from the Maurer group, Figure 11). Considering that the NXF1, adaptor serine/arginine-rich splicing factor 3 (SRSF3), is a known regulator of 3'UTR length (see section 1.10.2), this network is of particular interest, as it proposes a yet unconfirmed functional connection between 3'UTR length regulation, mRNA export and microtubule motor protein-dependent mRNA transport.

In this thesis, I thus chose to analyze and characterize the aforementioned rec-YnH network with the help of the developed TIRF-M-coupled in vitro reconstitution approach (see section 1.7.3) in order to assess whether the combination of a motor protein (kinesin-1/dynein), NXF1, SRSF3 and mRNA is necessary and sufficient to form a functional mRNP transport complex.

In the following sections, I will provide an overview of the key rec-YnH network RBPs NXF1 and SRSF3. I will thereby focus on their respective established functions and explore how they might form a functional mRNP transport complex in neurons.

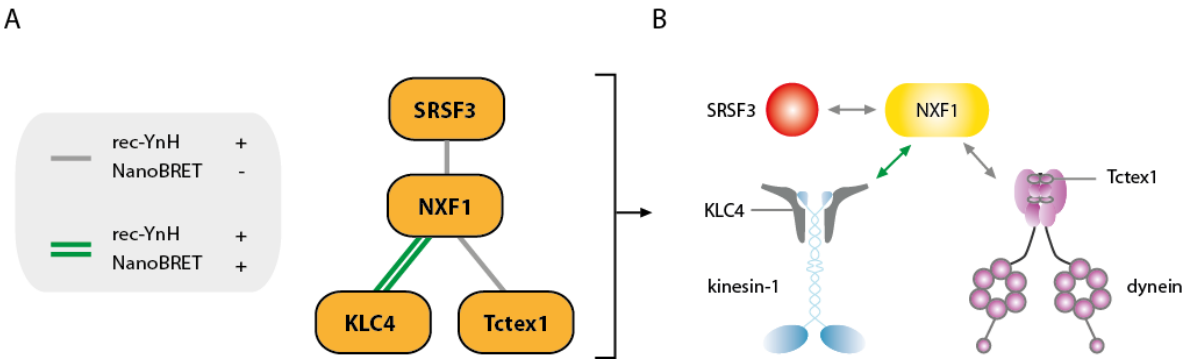

Figure 11: Selected rec-YnH network. (A) Interactions between kinesin-1/dynein light chains and NXF1 were identified via rec-YnH screening and verified via the NanoBRET approach whenever possible. Green: rec-YnH and NanoBRET positive; gray: rec-YnH positive, NanoBRET negative. **(B)** Cartoon representation of the rec-YnH network in (A). This network proposes a yet unconfirmed functional connection between NXF1/SRSF3 and kinesin-1- or dynein-based mRNA transport along microtubules.

1.9. NXF1

1.9.1. Domains and established functions

NXF1 is best-known for its function in the export of a large population of mRNAs (bulk mRNA) from the nucleus to the cytoplasm. It consists of five domains: an RNA-binding domain (RBD), a pseudo-RNA recognition motif (ΨRRM) domain, a leucine-rich repeat (LRR) domain, a nuclear transport factor 2-like (NTF2L) domain and a ubiquitin-associated domain (UBA) (Figure 12A). It has two distinct RNA-binding domains (RBDs) which are both essential for mRNA export (Braun et al. 2001; Hautbergue et al. 2008). With its N-terminal, arginine-rich RBD, it binds to bulk mRNA in an unspecific manner, while the ΨRRM-LRR domains constitute an RBD that specifically binds to mostly retroviral constitutive transport element (CTE) sequences (Teplova et al. 2011). During steady state, the N-terminal RBD is believed to undergo an intramolecular interaction with the NTF2L domain, resulting in the autoinhibition of NXF1, a state in which the N-terminal RBD is hidden and thus unable to bind RNA (Viphakone et al. 2012) (Figure 12B).

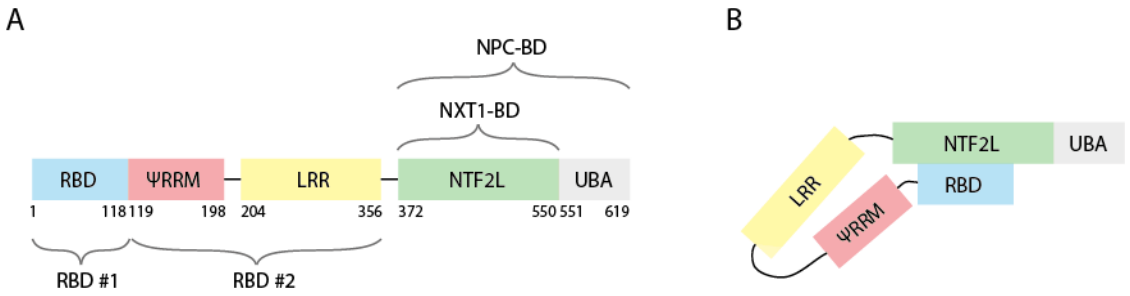

Figure 12: NXF1 domains and autoinhibition. (A) NXF1 consists of five domains: an N-terminal RBD, a pseudo-RNA recognition motif (ΨRRM) domain, a leucine-rich repeat (LRR) domain, a nuclear transport factor 2-like (NTF2L) domain and a ubiquitin-associated domain (UBA). It has two RBDs: an N-terminal RBD and an RBD that is composed of the ΨRRM and LRR. With its NTF2L domain, it binds to its cofactor NXT1 (NXT1-binding domain, NXT1-BD), and the nuclear pore complex (NPC) is bound by both the NTF2L and the UBA domains (NPC-binding domain, NPC-BD). **(B)** NXF1 is autoinhibited in steady state: The N-terminal RBD undergoes an intramolecular interaction with the NTF2L domain. In this state, NXF1 cannot bind to mRNAs and instead requires adaptor proteins to relieve the autoinhibition and to activate mRNA binding.

To relieve autoinhibition, NXF1 requires the binding of adaptors that trigger a conformational change and enable NXF1 to bind mRNA via its N-terminal RBD. There is a multitude of adaptors which bind to mRNA during transcription, splicing and further mRNA processing steps, and subsequently recruit NXF1 to promote the

export of mature mRNA (Hautbergue et al. 2008; Viphakone et al. 2012). The serine/arginine-rich splicing factor family (also known as SR proteins or SRSFs) functions as one of these NXF1 adaptors, with SRSF3 being the most potent adaptor from the SR protein family (Müller-McNicoll et al. 2016).

1.9.2. Is NXF1 involved in mRNA transport in the cytoplasm?

The literature indicates a well-established functional connection between members of the nuclear export factor (NXF) family and the cytoskeleton (reviewed in (Mamon et al. 2017)).

Mus musculus NXF2 (mNXF2), Mus musculus NXF7 (mNXF7) and Homo sapiens NXF5 (hNXF5) have been found to associate with translating ribosomes and have been observed in processing bodies (P-bodies) and neuronal RNA granules, hinting at a potential function of NXF proteins in cytoskeleton-dependent mRNA transport (Jun et al. 2001; Katahira et al. 2008). In addition, mNXF2 was shown to interact with motor proteins and microtubule-associated proteins including Staufen1, KIF9, KIF17 and the dynein light chain 1-like protein (Takano et al. 2007) in yeast-2-hybrid assays. It was also observed to form granules with KIF17 and mRNAs in dendrites of primary neurons, where it moves bidirectionally in a microtubule-dependent fashion (Takano et al. 2007). In addition, the Drosophila melanogaster NXF1 orthologue (dNXF1) is found to be localized in the cytoplasm in SL2 cells (Herold, Klymenko, and Izaurralde 2001) and is observed to be a component of cytoplasmic mRNP granules in neurites of mature Drosophila melanogaster neurons (Yakimova et al. 2016).

Homo sapiens NXF1 (hNXF1, hereafter referred to as NXF1), is predominantly known to localize to the nucleoplasm or the nuclear rim (Bear et al. 1999) as well as the cytoplasmic side of the nuclear pore complex (Ben-Yishay et al. 2019). Nevertheless, several studies suggest that NXF1 can also be found in the cytoplasm, which will be discussed below with respect to mRNA localization.

NXF1 is often described to only be a functional export factor if it is in a complex with its adaptor NXT1, with which it interacts via its NTF2L domain (Katahira et al. 2015). Interestingly though, in an early study, Jin et al. determined that NXF1 – but not its co-factor NXT1 – is associated with polysomes in 293T cells together with CTE-containing viral RNA (Jin et al. 2003), and thus propose that NXF1 plays a cytoplasmic role in the translational regulation of mRNA.

In addition, Saito et al. investigated the interaction between NXF1 and the neuronal RBD HuD and found that both proteins are partially localized to the apical end of neurites and somata of neuronal PC12 cells (Benita Wiatrak,Adriana Kubis-Kubiak 2020; Saito et al. 2004). Considering that HuD binds mRNAs containing AU-rich elements (Caput et al. 1986; Ma, Chung, and Furneaux 1997) which it exports from the nucleus via NXF1, the authors hypothesize that NXF1 could play a role in mRNA localization to neurites via an interaction with adaptor proteins like HuD and SR proteins (Saito et al. 2004).

Finally, in a more recent study performed in HeLa cells, NXF1 and CTE-derived Mason-Pfizer monkey virus RNA were observed to traffic together towards the microtubule-organizing center in a microtubule-dependent fashion (Pocock et al. 2016). Considering that the RNA clusters with microtubule minus ends at the microtubule organizing center, Pocock et al. hypothesize that microtubule motor proteins, in particular minus end-directed dynein, might be involved in NXF1-dependent viral RNA trafficking. The study also revealed that upon reaching the microtubule organizing center, the RNA demonstrates bidirectional transport along microtubules in accordance with the velocity of a plus end-directed motor, leading to the hypothesis that a kinesin might additionally be involved in the process.

In conclusion, several studies have shown that NXF family proteins interact with motor proteins and are localized in RNA granules. NXF1 itself has been shown to localize to the cytoplasm, where it is reported to interact with an mRNA-bound export adaptor and is transported with viral RNA via minus- and plus end-directed motor proteins. The selected rec-YnH network, suggesting for the first time a direct interaction between NXF1 and kinesin-1/dynein light chains, thus agrees well with existing data in the literature. Nevertheless, the direct interaction with microtubule motor proteins has to be validated, and the assembly of NXF1, mRNA and potential additional components within an mRNA transport complex, as well as potential transport properties, remain to be analyzed.

1.10. SRSF3

1.10.1. Domains and established functions

SRSF3 (initially named SRp20 according to its molecular weight of ~20 kDa), a potent NXF1 adaptor protein (Müller-McNicoll et al. 2016), belongs to the family of SR proteins that are conserved in metazoans and plants. They were initially identified as regulators of constitutive and alternative pre-mRNA splicing (reviewed in (Änkö 2014a)) and more recently described to fulfill a multitude of additional

functions in the cell (reviewed in (Slišković, Eich, and Müller-McNicoll 2022)), regulating every step of the mRNA life cycle, including 3'end processing, mRNA export, mRNP packaging, mRNA stability as well as translation.

The SR protein family consists of 12 canonical members that contain an RRM at their N-terminus and a highly unstructured arginine/serine (RS)-rich domain (RS domain) of at least 50 amino acids with an RS content of >40% (Manley and Krainer 2010) at their C-terminus. In addition to the N-terminal RRM, some SR proteins contain a ΨRRM domain (also called RRM homology domain), which is characterized by an atypical RRM fold. SRSF3 is the smallest protein of the SR protein family (Jeong 2017) with only 164 amino acids and an RS content of 69% (Wegener and Müller-McNicoll 2019) (Figure 13A).

SR proteins interact with mRNAs mostly via their RRMs. mRNA-binding specificity is thereby conferred via the number of RRMs, their spacing and the presence or absence of an additional Zn^{2+} knuckle. Interestingly, many binding motifs can be found for individual members of the SR protein family, and their motifs are short and degenerate (reviewed in (Änkö 2014a), see section 1.10.3).

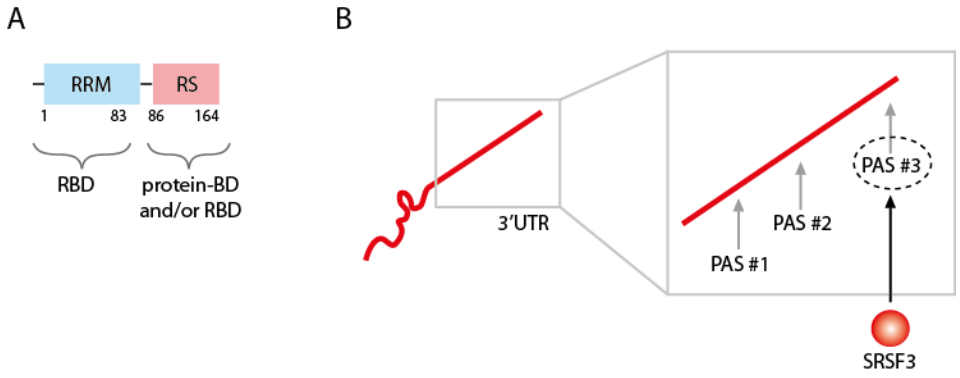

Figure 13: SRSF3 domains and influence on 3'UTR length. (A) SRSF3 has two domains: an RNA recognition motif (RRM) as well as a highly unstructured, arginine- and serine-rich domain (RS domain). The RS domain is mainly important for protein-protein interactions (protein-binding domain (protein-BD)), it can however also interact with mRNA (RBD). In contrast, the RRM is solely responsible for mRNA binding. **(B)** SRSF3 promotes distal polyadenylation site (PAS) selection, resulting in the generation of long 3'UTRs.

In contrast to the RRM, the RS domain is mainly responsible for protein-protein interactions (J. Y. Wu and Maniatis 1993), although it has also been described to interact with mRNA (reviewed in (Hertel and Graveley 2005)). The high amount of serines in the RS domain can be phosphorylated reversibly, and phosphorylation

plays an important role in regulating SR protein activity, subcellular localization and their biological functions. There are two classes of kinases, SRPKs and CLKs, which specifically phosphorylate SR proteins (Aubol et al. 2013): SRPK-mediated phosphorylation in the cytoplasm is essential for the nuclear import of SR proteins as well as their localization to nuclear speckles (Lai, Lin, and Tarn 2001), whereas CLK-mediated hyperphosphorylation in the nucleus is required for SR protein recruitment to transcription sites and the assembly of the spliceosome. Two phosphatases, PP1 and PP2A, dephosphorylate SR protein during splicing, resulting in the release of the spliceosome. The dephosphorylation is furthermore essential for the recruitment of NXF1 (see section1.11.1) and thus crucial for mRNP packaging and the export of mature mRNAs from the nucleus to the cytoplasm (reviewed in (Wegener and Müller-McNicoll 2019)).

1.10.2. SRSF3 regulates 3'UTR length

Two SR proteins have recently emerged as regulators of 3'UTR length by influencing the choice of proximal or distal polyadenylation sites. Via two mechanisms, SRSF3 promotes distal polyadenylation site selection, resulting in the generation long 3'UTRs (Figure 13B): Firstly, it directly counteracts SRSF7, another SR protein family member which promotes the generation of short 3'UTRs, and secondly, it maintains high levels of cleavage factor Im, the absence of which decreases 3'UTR length (Schwich et al. 2021).

The alternative choice of polyadenylation site is thought to influence the export efficiency of a given mRNA. By promoting distal polyadenylation site selection, SRSF3 increases the abundance of regulatory motifs (see section 1.6.2) and potential NXF1 binding sites, facilitating NXF1-based export of SRSF3/mRNA complexes (Müller-McNicoll et al. 2016).

1.10.3. SRSF3 motifs in neuropil-localized mRNAs

Besides being important for NXF1-mediated mRNA export, there are several indications in the literature hinting at a potential function of SRSF3 in accompanying mRNAs from the nucleus to distal locations in the neuropil.

In a massively parallel reporter assay for mRNA localization, the Moor group recently analyzed ~50,000 sequences and 3'UTRs of more than 300 genes, and determined that 3'UTR-dependent localization is the result of either (1) defined localization elements encoded in a 3'UTR or (2) a broader localization potential derived from the

contribution of several sequences in a given 3'UTR. In order to test whether RBPs are the drivers of localization via these localized or dispersed motifs, they mutated individual sequences, one of which contains the core motif CNYC (C: cytosine; N: any nucleotide; Y: cytosine or uracil; see section 1.11.2) recognized by SRSF3. In both analyzed cell lines, CAD and Neuro-2a, the wild type sequence containing UCUUCU (core SRSF3 motif underlined) was significantly enriched in the neurite fraction. The mutation of this sequence resulted in a significant decrease in neurite enrichment (Mikl et al. 2021), suggesting a function of SRSF3 in the targeting of mRNAs to the neuropil.

In a different study, Middleton et al. assessed the dendritic targeting capacity of differentially expressed/localized mRNAs, specifically focusing on identifying known RBP motifs that might be drivers of dendritic mRNA localization. Strikingly, they report that the highest enrichment for dendritic vs. somatic localization was observed for the sequence AUCAWCG (W: adenine or uracil, core SRSF3 motif underlined) (Middleton, Eberwine, and Kim 2019). Interestingly, this motif was also more enriched than guanine quadruplex RNA structures (G-quadruplexes) which have previously been implicated in promoting dendritic localization (Subramanian et al. 2011) and are often found in the 3'UTR of well-known dendritically localizing mRNAs such as BDNF and CamKIIα mRNAs. Based on this observation, Middleton et al. suggest that SRSF3, via potential motif inclusion and recruitment of NXF1, might be involved in at least the early steps of dendritic mRNA localization (Middleton, Eberwine, and Kim 2019).

In conclusion, SRSF3 is an RBP that promotes the generation of long 3'UTRs to which it recruits NXF1, resulting in the export of NXF1/SRSF3/mRNA complexes from the nucleus to the cytoplasm. Different groups have reported an enrichment of the core SRSF3 motif in neuropil-localized mRNAs, deletion of which results in their accumulation in the soma. This leads to the hypothesis that SRSF3 may play a crucial role in guiding mRNAs to distal compartments in neurons. Nevertheless, whether NXF1/SRSF3/mRNA complexes can be transported along the microtubule cytoskeleton via motor proteins, as well as potential transport properties of this proposed complex, remain to be analyzed.

1.11. Interactions between NXF1/SRSF3-mRNP components

1.11.1. How do NXF1 and SRSF3 interact?

The association between NXF1 and SRSRF3 is postulated to take place subsequent to the completion of nuclear splicing, as the splicing-dependent dephosphorylation of SRSF3 is necessary for its interaction with NXF1 (Y. Huang, Yario, and Steitz 2004; Lai and Tarn 2004). This indicates the presence of a control mechanism that ensures the selective transport of only mature mRNA from the nucleus to the cytoplasm.

The interaction between SR proteins and NXF1 has been investigated by several groups and is generally described as a direct interaction (Hargous et al. 2006; Yingqun Huang et al. 2003; Lai and Tarn 2004; Tintaru et al. 2007), although mostly determined using indirect methods (see section 1.7.1).

In pull-down experiments, Huang et al. show that immobilized NXF1 interacts with SRSF3 in HeLa cell nuclear extract. They further report that the N-terminal region of NXF1 (aa 1-362) is responsible for this interaction (Yingqun Huang et al. 2003) (Figure 14). Of note, pull-down experiments were performed in the presence of RNase A, suggesting that mRNA is not necessary for this interaction to occur.

Similarly, based on pull-down experiments using immobilized NXF1/NXT1 and SRSF3 synthesized in rabbit reticulocyte lysate, Hargous et al. report that the interaction between NXF1 and SRSF3 is dependent on the linker between the SRSF3 RRM and RS domains, a short stretch of arginine-rich residues (EKRSRNR) (Figure 14). Mutation of the arginine residues prevented an interaction between SRSF3 and NXF1, which was further confirmed via co-immunoprecipitation. Of note, pull-down experiments were conducted in the presence of RNase, while co-immunoprecipitation experiments were performed following alkaline phosphatase and RNase treatment (Hargous et al. 2006). These findings provide support to the notion that mRNA is not required for bridging the interaction between NXF1 and dephosphorylated SRSF3.

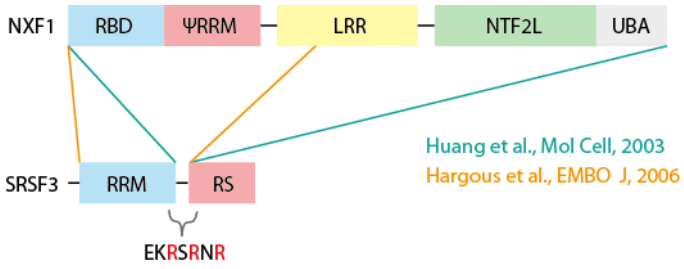

Figure 14: The interaction between NXF1 and SRSF3. The NXF1/SRSF3 interaction is often described as direct. Based on pull-down experiments (Hargous et al. 2006; Yingqun Huang et al. 2003), the N-terminal region of NXF1 is proposed to interact with the linker between the RRM and RS domain of SRSF3, more specifically with the arginine residues (marked in red) in the linker sequence.

1.11.2. How do SRSF3 and NXF1 interact with bulk mRNA?

Due to their functional differences, individual SR proteins were long believed to bind mRNA in a sequence-specific manner. Various techniques, such as systematic evolution of ligands by exponential enrichment (SELEX), (i)CLIP (reviewed in (Jeong 2017)) as well as nuclear magnetic resonance spectroscopy approaches (Hargous et al. 2006) have since been used to identify SR protein motifs.

In accordance with SELEX approaches (Cavaloc et al. 1999; Schaal and Maniatis 1999) that revealed the consensus SRSF3 motif CYYC (C: cytosine; Y: pyrimidine), more recent iCLIP studies led to the identification of a matching core motif, CNYC (C: cytosine; N: any nucleotide; Y: pyrimidine) (Änkö et al. 2012; Müller-McNicoll et al. 2016). The unspecific recognition of distinct nucleotides in the motif explains the diversity of the reported SRSF3 binding sequences (reviewed in (Änkö 2014a)): nuclear magnetic resonance spectroscopy-derived solution structures of the SRSF3 RRM in complex with the 4 nucleotide RNA sequence CAUC (Hargous et al. 2006) have shown that only the 5'cytosine is recognized in a specific manner, whereas the 3'cytosine is favored over other nucleotides at this position. Both of them are stabilized in the β–sheet of the SRSF3 RRM via hydrogen bond formation. The remaining nucleotides, on the other hand, are barely stabilized, allowing for interchangeable nucleotides at positions 2 and 3.

Interestingly, recent iCLIP data shows that NXF1 and SRSF3 bind to the 3'UTR of mRNAs in close proximity to each other (within a 60 nucleotide window). Consistent with this, the interaction of NXF1 and SRSF3 in pull-down studies is lost upon prolonged treatment with RNase, favoring the hypothesis that the NXF1/SRSF3 interaction is stabilized by mRNA (Müller-McNicoll et al. 2016), although previous

studies reported an mRNA-independent interaction between the two proteins (Hargous et al. 2006; Yingqun Huang et al. 2003) (see section 1.11.1). Finally, in vivo iCLIP data provided additional insights into the recruitment of NXF1 to 3'UTRs by SRSF3 in cells: The binding motif of NXF1 was found to be highly similar to that of SRSF3 in 3'UTRs, while it differed in other regions of the mRNA (Müller-McNicoll et al. 2016). Considering that SRSF3 predominantly binds to the 3'UTR of mRNAs, this suggests that SRSF3 recruits NXF1 to these SRSF3 binding sites in 3'UTRs.

In conclusion, NXF1 is proposed to interact with the RRM-RS linker of SRSF3, confirming the direct interaction between NXF1 and SRSF3 found in the rec-YnH screen. This interaction is likely stabilized by mRNA, considering that (1) NXF1 and SRSF3 bind in close proximity to each other in the 3'UTR of mRNAs and (2) the interaction is lost upon prolonged RNase treatment. The NXF1/SRSF3/mRNA complex that travels from the nucleus to the cytoplasm thus comprises interactions of all components with each other, forming a stable mRNP complex.

1.12. Why study the selected rec-YnH network?

Overall, the direct interactions identified in the selected rec-YnH network (see section 1.8, Figure 11), comprising light chains of kinesin-1 and dynein, the export factor NXF1 and the 3'UTR length regulator SRSF3, combine previously reported interactions (NXF1-SRSF3) with newly identified interactions (KLC4/Tctex1-NXF1). Both types of interactions are either supported by substantial evidence or match observations made in previous studies (see sections 1.9.2 and 1.11.1):

a) The interaction between NXF1 and SRSF3 has been analyzed by several groups (Hargous et al. 2006; Yingqun Huang et al. 2003; Müller-McNicoll et al. 2016), and is proposed to be a direct interaction that is stabilized by mRNA (Müller-McNicoll et al. 2016).

b) NXF1 has been implicated in bidirectional viral RNA trafficking (Pocock et al. 2016) and other NXF family proteins have been reported to (1) interact with motor proteins, (2) be present in RNA granules, (3) be involved in (bidirectional) mRNA transport (Herold, Klymenko, and Izaurralde 2001; Jun et al. 2001; Katahira et al. 2008; Takano et al. 2007; Yakimova et al. 2016).

Based on the selected rec-YnH network, NXF1 is proposed to be the central factor connecting microtubule motor proteins with SRSF3/mRNA complexes, and would thus represent a novel, yet unconfirmed motor/mRNA adaptor. Furthermore, NXF1

links mRNA transport to SRSF3 which has been suggested to regulate 3'UTR length and mRNA localization in previous studies (see sections 1.10.2 and 1.10.3):

a) SRSF3 promotes the generation of long 3'UTRs to which it remains bound to during NXF1 recruitment and export from the nucleus to the cytoplasm (Müller-McNicoll et al. 2016).

b) SRSF3 motifs are enriched in neuropil-localized mRNAs, and deletion of sequences that include the core SRSF3 motif results in their accumulation in the soma (Middleton, Eberwine, and Kim 2019; Mikl et al. 2022).

Hence, if confirmed by further analyses, this rec-YnH network would represent the first reported link between 3'UTR length regulation, mRNA export and mRNA localization, making it an exciting network to study in the context of mRNA transport.

2. MOTIVATION

The precise localization of neuronal mRNAs is a fundamental process that has fascinated researchers for decades, as it serves as the first step in ensuring the local translation of proteins at defined sites within the neuron.

Although neurons harbor thousands of localized mRNAs (Cajigas et al. 2012; Gumy et al. 2011; Middleton, Eberwine, and Kim 2019; Zivraj et al. 2010), there is only a limited amount of motor proteins that can transport these mRNAs. In the mRNA localization field, it thus remains to be understood (1) how these mRNAs are selectively packaged and precisely delivered within neurons; (2) whether there are specific, yet unknown adaptor proteins that connect specific mRNAs to motor proteins; and (3) which factors define the final destination of an mRNA within neurons.

To date, the exact mechanisms with which neuronal mRNAs are coupled to motor proteins and reach their final destination remain mostly unknown. Numerous publications have reported a multitude of proteins that are suggested to be involved in mRNA transport, however, the employed methods predominantly report indirect interactions and are not able to disentangle pleiotropic effects from actual functions in mRNA transport. The identification of direct interactions and the reconstitution of these interactions are thus necessary to verify whether and how the associated proteins are involved in mRNA transport.

The recently developed rec-YnH interaction screen (Yang et al. 2018) revealed a network that suggests direct interactions between the light chains of microtubule motor proteins kinesin-1 and dynein, the main nuclear export factor of bulk mRNA, NXF1, and a 3'UTR length regulator, SRSF3. The established functions of the individual network components suggest an mRNA transport system (Figure 15) in which (1) SRSF3 promotes the generation of long 3'UTRs in the nucleus, (2) NXF1 is recruited to these long 3'UTRs, (3) NXF1 exports the SRSF3/mRNA complexes from the nucleus to the cytoplasm, (4) NXF1/SRSF3/mRNA complexes are recruited to microtubule motor proteins via the NXF1/light chain interaction, and (5) microtubule motor proteins transport the NXF1/SRSF3/mRNA complexes to their final destination in the neuropil. As both NXF1 and SRSF3 are suggested to bind to the 3'UTR of mRNAs at neighboring positions while simultaneously interacting with one another, we hypothesize that the transported mRNP is stable and can thus reach distal destinations within neurons.

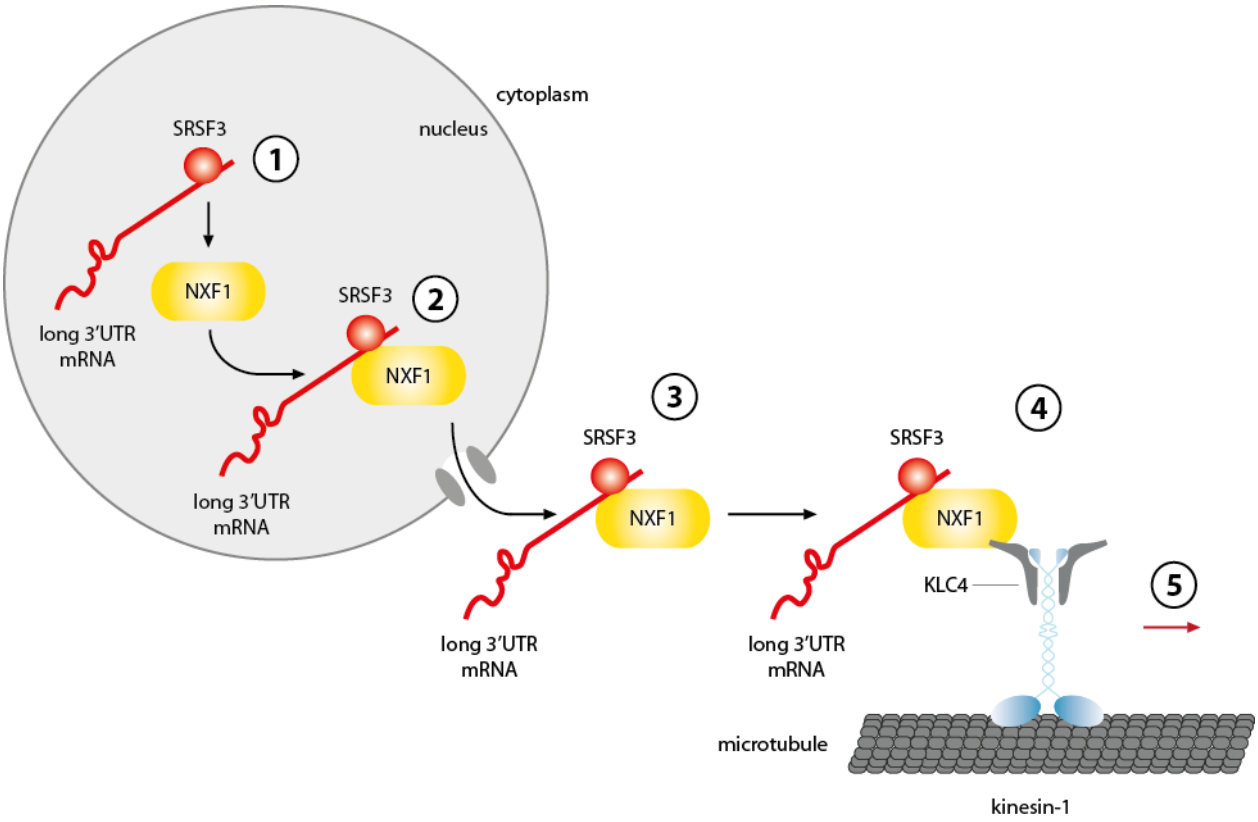

Figure 15: Proposed mRNA transport system based on the selected rec-YnH network. The assembly of the proposed mRNA transport system is suggested to follow these steps: (1) SRSF3 promotes the generation of long 3'UTRs in the nucleus, (2) NXF1 is recruited to these long 3'UTRs, (3) NXF1 exports the SRSF3/mRNA complex from the nucleus to the cytoplasm, (4) NXF1/SRSF3/mRNA complexes are recruited to microtubule motor proteins (here exemplified for kinesin-1) via the NXF1/light chain interaction, (5) microtubule motor proteins transport the NXF1/SRSF3/mRNA complexes to their final destination in the neuropil.

As described above, TIRF-M-coupled in vitro reconstitution approaches represent a very useful method to validate whether a given network comprises the *minimal* factors both necessary and sufficient for the formation of a functional mRNP transport complex.

In this thesis, I was hence interested in answering the following questions using the developed TIRF-M-coupled in vitro reconstitution approach (Grawenhoff, Baumann, and Maurer 2022):

1) Is NXF1 transported by microtubule motor proteins?

2) Are NXF1 and SRSF3 co-transported by microtubule motor proteins?

3) Are NXF1/SRSF3 the minimal components that tether mRNAs to microtubule motor proteins?

4) Which SRSF3 motifs are recognized by the proposed mRNP transport complex?

5) Do the NXF1/SRSF3/mRNA complexes remain stable or fall apart during motor protein-based transport?

In the following sections, I will describe the work accomplished in order to address these questions.

3. MATERIALS & METHODS

3.1. Cloning

Cloning of all protein constructs was performed by Magüi Gili (Maurer group). For individual protein constructs, the N- or C-terminal placements of solubility, purification and/or fluorescent labeling tags were determined based on literature information on protein domains implicated in the interaction with other proteins. Additionally, to minimize the number of constructs generated, protein constructs were generally designed with fluorescent labeling tags that were separated from the core proteins via protease cleavage sites. This enabled the expression and purification of both fluorescently labeled and unlabeled proteins using the same construct.

3.1.1. NXF1(-SNAP)

The *Nxf1* coding region was PCR-amplified from a codon-optimized version of human *Nxf1* (accession no.: NM_006362.5) and inserted by Gibson assembly into a pCoofy17 backbone vector for expression in E. coli. This resulted in a recombinant *Nxf1* gene N-terminally flanked by a Protein A solubility tag (ZZ-tag) and the HRV-3C protease cleavage site, as well as C-terminally flanked by the TEV protease cleavage site, a linker sequence (ILGAPSGGGATAGAGGAGGPAGLIN), a self-labeling protein tag (SNAP-tag), another HRV-3C protease cleavage site and a His-tag. The final construct was validated by sequencing of the entire open-reading frame and named pCoofy17_ZZ-3C-NXF1-TEV-HL-SNAP-3C-His.

3.1.2. (SNAP-)SRSF3

The *Srsf3* coding region was PCR-amplified from a codon-optimized version of mouse *Srsf3* (accession no.: NM_013663.5) and inserted by Gibson assembly into a pCoofy17 backbone vector for expression in E. coli. This resulted in 3 different constructs: (1) a recombinant *Srsf3* gene N-terminally flanked by an N-utilization substance protein A (NusA) solubility tag and the small ubiquitin-like modifier 3 (SUMO3) protease cleavage site, as well as C-terminally flanked by the HRV-3C protease cleavage site and a Twin-Strep-tag; (2) a recombinant *Srsf3* gene N-terminally flanked by a maltose-binding protein (MBP) solubility tag and the SUMO3 protease cleavage site, as well as C-terminally flanked by the HRV-3C protease cleavage site and a Twin-Strep-tag; and (3) a recombinant *Srsf3* gene N-terminally flanked by a NusA solubility tag, the SUMO3 protease cleavage site and a SNAP-

tag, as well as C-terminally flanked by the HRV-3C protease cleavage site and a Twin-Strep-tag. The final constructs were validated by sequencing of the entire open-reading frame and named pCoofy17_NusA-SUMO3-SRSF3-3C-Strep, pCoofy17_MBP-SUMO3-SNAP-SRSF3-3C-Strep and pCoofy17_NusA-SUMO3-SNAP-SRSF3-3C-Strep.

3.1.3. (SNAP-)FEZ2

The *Fez2* coding region was PCR-amplified from a codon-optimized version of mouse *Fez2* (accession no.: NM_001285940.1) and inserted by Gibson assembly into a pCoofy17 backbone vector for expression in E. coli. This resulted in a recombinant *Fez2* gene N-terminally flanked by a Protein A solubility tag (ZZ-tag), the HRV-3C protease cleavage site, a SNAP-tag, the SUMO3 protease cleavage site, as well as C-terminally flanked by another HRV-3C protease cleavage site and a Twin-Strep-tag. The final construct was validated by sequencing of the entire open-reading frame and named pCoofy17_ZZ-3C-SNAP-SUMO3-FEZ2-3C-Strep.

3.1.4. RTRAF(-SNAP)

The *Rtraf* coding region was PCR-amplified from a codon-optimized version of mouse *Rtraf* (accession no.: NM_026528.3) and inserted by Gibson assembly into a pCoofy17 backbone vector for expression in E. coli. This resulted in a recombinant *Rtraf* gene N-terminally flanked by a NusA solubility tag, a SUMO3-tag, as well as C-terminally flanked by a linker sequence (ILGAPSGGGATAGAGGAGGPAGLIN), a SNAP-tag, an HRV-3C protease cleavage site and a Twin-Strep-tag. The final construct was validated by sequencing of the entire open-reading frame and named pCoofy17_NusA-SUMO3-RTRAF-HL-SNAP-3C-Strep.

3.1.5. NudT21(-SNAP)

The *NudT21* coding region was PCR-amplified from a codon-optimized version of mouse *NudT21* (accession no.: NM_026623.3) and inserted by Gibson assembly into a pCoofy17 backbone vector for expression in E. coli. This resulted in a recombinant *NudT21* gene N-terminally flanked by a Protein A solubility tag (ZZ-tag) and an HRV-3C protease cleavage site, as well as C-terminally flanked by a TEV protease cleavage site, a linker sequence (ILGAPSGGGATAGAGGAGGPAGLIN), a SNAP-tag, another HRV-3C protease cleavage site and a His-tag. The final construct was validated by sequencing of the entire open-reading frame and named pCoofy17_ZZ-3C-NudT21-TEV-HL-SNAP-3C-His.

3.1.6. (SNAP-)KIF5A

The *Kif5a* coding region was PCR-amplified from a codon-optimized version of mouse *Kif5a* (accession no.: NP_001034089.1) and inserted by Gibson assembly into a pLIB backbone vector from the biGBac system for expression in Spodoptera frugiperda insect cells. This resulted in a recombinant *Kif5a* gene N-terminally flanked by a Twin-Strep-tag, an HRV-3C protease cleavage site, a SNAP-tag, a linker sequence (ILGAPSGGGATAGAGGAGGPAGLIN) and a TEV protease cleavage site. The final construct was validated by sequencing of the entire open-reading frame and named pLIB_Strep-3C-SNAP-HL-TEV-KIF5A.

3.1.7. KLC4 / KLC4-SNAP

The *Klc4* coding region was PCR-amplified from a codon-optimized version of mouse *Klc4* (accession no.: NM_029091.3) and inserted by Gibson assembly into a pLIB backbone vector from the biGBac system for expression in Spodoptera frugiperda insect cells. This resulted in 2 different constructs: (1) a recombinant *Klc4* gene C-terminally flanked by a TEV protease cleavage site, a linker sequence (ILGAPSGGGATAGAGGAGGPAGLIN), a SNAP-tag, an HRV-3C protease cleavage site and a His-tag; and (2) a recombinant *Klc4* gene without any additional solubility, affinity or fluorescent labeling tags. The final constructs were validated by sequencing of the entire open-reading frame and named pLIB_KLC4-TEV-HL-SNAP-3C-His and pLIB_KLC4.

3.2. Protein expression

All recombinant proteins used in this work were expressed either in E. coli strains or Spodoptera frugiperda cells. Protein expression in Spodoptera frugiperda cells was performed by Magüi Gili (Maurer group). In general, two versions of each wild type protein were expressed: (1) the unmodified protein lacking any further tags, and (2) the wild type version of the protein modified with an additional SNAP-tag that was later labeled with fluorescent dyes.

3.2.1. Expression of NXF1(-SNAP)

BL21-AI™ One Shot™ Chemically Competent E. coli (Invitrogen) were transformed with the corresponding plasmid (pCoofy17_ZZ-3C-NXF1-TEV-HL-SNAP-3C-His) for the expression of NXF1 and NXF1-SNAP, respectively. Protein expression in LB medium supplemented with kanamycin was induced via the addition of 0.5 mM

isopropyl β-D-1-thiogalactopyranoside (IPTG) and 0.2% L-arabinose at an optical density $(OD)_{600}$=0.8 for 16 h at 200 rpm, 18°C. Bacteria were harvested by centrifugation (4,000 x g, 4°C, 20 min), and pellets were stored at -80°C.

3.2.2. Expression of SRSF3 and SNAP-SRSF3

Since bacterial expression conditions yielding soluble full-length SRSF3 could not be found in literature (Hargous et al. 2006; Yingqun Huang et al. 2003), different parameters for the expression of SRSF3 were tested in a small-scale expression test using 2 ml LB cultures supplemented with kanamycin. These parameters included 2 different E. coli strains (BL21-CodonPlus(DE3)-RIL and Rosetta™ (DE3)pLysS), 2 N-terminal solubility tags (MBP-tag and NusA-tag (Raran-kurussi and Waugh 2012; Raran-Kurussi and Waugh 2014)) as well as 3 different expression conditions with varying IPTG concentrations, temperatures and total expression times: (1) 1 mM IPTG, 37°C, 3 h; (2) 0.5 mM IPTG, 25°C, 5 h; (3) 0.1 mM IPTG, 18°C, 16 h. For each of the conditions, 1 ml samples were taken, sonicated (with a small tip) using a Sonicator (Branson) (amplitude: 37%, 0.3 s pulse on/ 0.3 s pulse off, room temperature) and subsequently analyzed via SDS-PAGE and Coomassie staining.

For the large-scale expression of SRSF3, Rosetta™(DE3)pLysS Competent Cells (Novagen) were transformed with the corresponding plasmids (pCoofy17_NusA-SUMO3-SRSF3-3C-Strep/ and pCoofy17_NusA-SUMO3-SNAP-SRSF3-3C-Strep) for the expression of SRSF3 and SNAP-SRSF3, respectively. Protein expression in LB medium supplemented with kanamycin was induced via the addition of 0.1 mM IPTG at an OD_{600}=0.5 for 16 h at 200 rpm, 18°C. Bacteria were harvested by centrifugation (4,000 x g, 4°C, 20 min), and pellets were stored at -80°C.

3.2.3. Expression of (SNAP-)FEZ2

BL21-CodonPlus(DE3)-RIL E. coli (Agilent) were transformed with the corresponding plasmid (pCoofy17_ZZ-3C-SNAP-SUMO3-FEZ2-3C-Strep) for the expression of FEZ2 and SNAP-FEZ2, respectively. Protein expression in LB medium supplemented with kanamycin was induced via the addition of 0.5 mM IPTG at an OD_{600}=0.8 for 16 h at 200 rpm, 18°C. Bacteria were harvested by centrifugation (4,000 x g, 4°C, 20 min), and pellets were stored at -80°C.

3.2.4. Expression of RTRAF(-SNAP)

BL21-CodonPlus(DE3)-RIL E. coli (Agilent) were transformed with the corresponding plasmid (pCoofy17_NusA-SUMO3-RTRAF-HL-SNAP-3C-Strep) for the expression of RTRAF and RTRAF-SNAP, respectively. Protein expression in LB medium supplemented with kanamycin was induced via the addition of 0.5 mM IPTG at an OD_{600}=0.8 for 16 h at 200 rpm, 18°C. Bacteria were harvested by centrifugation (4,000 x g 4°C, 20 min), and pellets were stored at -80°C.

3.2.5. Expression of NudT21(-SNAP)

BL21-AI™ One Shot™ Chemically Competent E. coli (Invitrogen) were transformed with the corresponding plasmid (pCoofy17_ZZ-3C-NudT21-TEV-HL-SNAP-3C-His) for the expression of NudT21 and NudT21-SNAP, respectively. Protein expression in LB medium supplemented with kanamycin was induced via the addition of 0.5 mM IPTG and 0.2% L-arabinose at an OD_{600}=0.8 for 16 h at 200 rpm, 18°C. Bacteria were harvested by centrifugation (4,000 x g, 4°C, 20 min), and pellets were stored at -80°C.

3.2.6. Expression of KIF5A HC

800 ml Sf21 II cell suspension at 1.5x10e6 cells/ml were infected with 800 µl of a V1 Baculovirus (pLIB_Strep-3C-SNAP-HL-TEV-KIF5A) and incubated in a 2 l flask in a shaker-incubator (100 rpm, 27ºC, 3 days). Cells were harvested by centrifugation (2,000 x g, 4ºC, 15 min), resuspended in cold 1x PBS and centrifuged again (2,000 x g, 4ºC, 15 min). The supernatant was discarded and the pellet was frozen in liquid N_2 and stored at -80ºC.

3.2.7. Co-Expression of (SNAP-)KIF5A HC and KLC4

800 ml Sf21 III cell suspension at 1.5x10e6 cells/ml were infected with 800 µl of a V1 Baculovirus (pLIB_Strep-3C-SNAP-HL-TEV-KIF5A) and with 400 µl of a V1 Baculovirus (pLIB_KLC4) and incubated in a 2 l flask in a shaker-incubator (100 rpm, 27ºC, 3 days). Cells were harvested by centrifugation (2,000 x g, 4ºC, 15 min), resuspended in cold 1x PBS and centrifuged again (2,000 x g, 4ºC, 15 min). The supernatant was discarded and the pellet was frozen in liquid N_2 and stored at -80ºC.

3.2.8. Co-Expression of KIF5A HC and KLC4-SNAP

600 ml Sf21 II cell suspension at 2x10e6 cells/ml were infected with 800 µl of a V1 Baculovirus (pLIB_Strep-3C-KIF5A) and with 1000 µl of a V1 Baculovirus (pLIB_KLC4-TEV-HL-SNAP-3C-His) and incubated in a 2 l flask in a shaker-incubator (100 rpm, 27ºC, 3 days). Cells were harvested by centrifugation (2,000 x g, 4ºC, 15 min), resuspended in cold 1x PBS and centrifuged again (2,000 x g, 4ºC, 15 min). The supernatant was discarded and the pellet was frozen in liquid N_2 and stored at -80ºC.

3.3. Purification of recombinant proteins

3.3.1. Purification of NXF1 and NXF1-SNAP

3.5-5 g of pelleted BL21-AI™ One Shot™ Chemically Competent E. coli (Invitrogen) with the corresponding plasmid for the expression of ZZ-NXF1-SNAP-His were resuspended in 40 ml NXF1-LEGF buffer (100 mM NaPi, 400 mM KCl, 5 mM $MgCl_2$, 0.001% Brij-35, 0.7 mM β-mercaptoethanol (BME), pH 7.2) supplemented with 1 EDTA-free cOmplete™ protease inhibitor tablet (Sigma) and DNase I (Roche). Cells were lysed by sonication (4 min total: 20 s pulse on/ 30 s pulse off, 50% amplitude, 4°C), and cell debris was pelleted by centrifugation (184,000 x g, 45 min, 4°C). The supernatant was applied to a 5 ml HisTrap Chelating HP column (Cytiva) pre-charged with Co^{2+} and pre-equilibrated with NXF1-LEGF buffer at 4°C using a peristaltic pump. The column was washed with 30 column volumes (CV) of NXF1-Wash buffer (100 mM NaPi, 400 mM KCl, 5 mM $MgCl_2$, 0.001% Brij-35, 0.7 mM BME, 25 mM imidazole, pH 7.2), and ZZ-NXF1-SNAP-His was eluted with NXF1-elution buffer (100 mM NaPi, 400 mM KCl, 5 mM $MgCl_2$, 0.001% Brij-35, 0.7 mM BME, 400 mM imidazole). The eluted ZZ-NXF1-SNAP-His was incubated either with His-tagged PreScission and His-tagged TEV proteases (Biomolecular Screening & Protein Technologies Unit, CRG) for the purification of NXF1 or solely with His-tagged 3C PreScission (Biomolecular Screening & Protein Technologies Unit, CRG) for the purification of NXF1-SNAP. After incubation for 16 h at 4°C, both protein samples were concentrated using 30 kDa molecular weight cut-off (MWCO) filters (Merck) and were subsequently ultra-centrifuged (280,000 x g, 15 min, 4°C) to remove potential aggregates. NXF1 and NXF1-SNAP were finally purified via size exclusion chromatography (SEC) using a Superdex® 200 Increase 10/300 GL column (Cytiva) equilibrated with NXF1-LEGF buffer. Protein-containing fractions were pooled and further concentrated using 30 kDa MWCO filters (Merck). NXF1-SNAP was fluorescently labeled using SNAP-Cell® TMR-Star (NEB) with a ratio of 1:3 NXF1-SNAP:dye at 4°C for 16 h in the presence of 2 mM DTT. Non-conjugated dye was removed using a 10 ml Zeba™ Spin Desalting Column (Thermo Fisher Scientific), and NXF1-SNAP was ultra-centrifuged (280,000 x g, 15 min, 4°C) to

remove potential aggregates. Final labeling ratio and protein concentration were determined using a NanoDrop™ One/OneC Microvolume UV-Vis Spectrophotometer, and NXF1-SNAP aliquots were flash-frozen and stored in liquid N_2.

3.3.2. Purification of SRSF3

7-10 g of pelleted Rosetta™(DE3)pLysS Competent Cells (Novagen) with the corresponding plasmid for the expression of NusA-SRSF3-Strep were resuspended in 50 ml SRSF3-LEGF buffer (100 mM NaPi, 600 mM KCl, 3 mM $MgCl_2$, 0.7 mM BME, 50 mM L-arginine, 50 mM L-glutamate, pH 7.4) supplemented with 1 cOmplete™ ULTRA EDTA-free protease inhibitor tablet (Sigma) and DNase I (Thermo Fisher Scientific). Cells were lysed by sonication (4 min total: 20 s pulse on/ 30 s pulse off, 50% amplitude, 4°C), and cell debris was pelleted by centrifugation (184,000 x g, 45 min, room temperature (RT)). The supernatant was applied to a 5 ml StrepTrap HP column (Cytiva) pre-equilibrated with SRSF3-LEGF buffer at RT using a peristaltic pump. The column was washed with 30 CV of SRSF3-LEGF buffer, and removal of the NusA-tag was performed by on-column cleavage with His-tagged SENP2 protease (Biomolecular Screening & Protein Technologies Unit, CRG) for 1 h at RT. The cleaved Strep-tag and His-tagged SENP2 protease were then removed by a 22 CV wash step using SRSF3-LEGF buffer. Finally, SRSF3 was eluted from the StrepTrap HP column via an on-column cleavage of its Strep-tag via His-tagged PreScission protease (Biomolecular Screening & Protein Technologies Unit, CRG) for 1 h at RT. To remove the His-tagged PreScission protease during SRSF3 elution with SRSF3-LEGF buffer, a 1 ml HisTrap FF column pre-equilibrated with SRSF3-LEGF buffer was attached to the StrepTrap HP column. The eluted SRSF3 was concentrated with Amicon Ultra-15 10 kDa MWCO filters (Merck) and ultra-centrifuged (280,000 x g, 15 min, RT) to remove potential aggregates. Final protein concentration was determined using a NanoDrop™ One/OneC Microvolume UV-Vis Spectrophotometer, and SRSF3 aliquots were flash-frozen and stored in liquid N_2.

3.3.3. Purification of SNAP-SRSF3

7-10 g of pelleted Rosetta™(DE3)pLysS Competent Cells (Novagen) with the corresponding plasmid for the expression of NusA-SUMO3-SNAP-SRSF3-Strep were resuspended in 50 ml SNAP-SRSF3-LEGF buffer (100 mM NaPi, 600 mM KCl, 3 mM $MgCl_2$, 0.7 mM BME, 50 mM L-arginine, 50 mM L-glutamate, 5 mM EDTA, pH 7.4) supplemented with 1 cOmplete™ ULTRA EDTA-free protease inhibitor tablet (Sigma) and DNase I (Roche). Cells were lysed by sonication (4 min total: 20 s pulse

on/ 30 s pulse off, 50% amplitude, 4°C), and cell debris was pelleted by centrifugation (184,000 x g, 45 min, RT). The supernatant was applied to a 5 ml StrepTrap HP column (Cytiva) pre-equilibrated with SNAP-SRSF3-LEGF buffer at RT using a peristaltic pump. The column was washed with 30 CV of SNAP-SRSF3-LEGF buffer, and removal of the NusA-SUMO3-tag was performed by on-column cleavage with His-tagged SENP2 protease (Biomolecular Screening & Protein Technologies Unit, CRG) for 1 h at RT. The cleaved Strep-tag and His-tagged SENP2 protease were then removed by a 30 CV wash step using SNAP-SRSF3-LEGF buffer. Finally, SNAP-SRSF3 was eluted from the StrepTrap HP column via an on-column cleavage of its Strep-tag via His-tagged PreScission protease (Biomolecular Screening & Protein Technologies Unit, CRG) for 1 h at RT. To remove the His-tagged PreScission protease during SNAP-SRSF3 elution with SNAP-SRSF3-LEGF buffer, a 5 ml HisTrap excel column pre-equilibrated with SRSF3-LEGF buffer was attached to the StrepTrap HP column. The eluted SRSF3 was concentrated with Amicon Ultra-15 30kDa MWCO filters (Merck), and SNAP-SRSF3 was fluorescently labeled using SNAP-Surface® Alexa Fluor® 647 (NEB) with a ratio of 1:1.5 SNAP-SRSF3:dye at RT for 3 h in the presence of 2 mM DTT. Non-conjugated dye was removed using a 5 ml Zeba™ Spin Desalting Column (Thermo Fisher Scientific), and SNAP-SRSF3 was ultra-centrifuged (280,000 x g, 15 min, RT) to remove potential aggregates. Final labeling ratio and protein concentration were determined using a NanoDrop™ One/OneC Microvolume UV-Vis Spectrophotometer, and SNAP-SRSF3 aliquots were flash-frozen and stored in liquid N_2.

3.3.4. Purification of FEZ2

3.5-5 g of pelleted BL21-AI™ One Shot™ Chemically Competent E. coli (Invitrogen) with the corresponding plasmid for the expression of ZZ-SNAP-SUMO3-FEZ2-Strep were resuspended in 40 ml FEZ2-LEGF buffer (100 mM NaPi, 600 mM KCl, 5 mM $MgCl_2$, 5 mM DTT, pH 7.0) supplemented with 1 cOmplete™ ULTRA EDTA-free protease inhibitor tablet (Sigma) and DNase I (Roche). Cells were lysed by sonication (3 min total: 20 s pulse on/ 30 s pulse off, 50% amplitude, 4°C), and cell debris was pelleted by centrifugation (184,000 x g, 45 min, 4°C). The supernatant was applied to a 5 ml StrepTrap HP column (Cytiva) pre-equilibrated with FEZ2-LEGF buffer at 4°C using a peristaltic pump. The column was washed with 40 CV of FEZ2-LEGF buffer, and removal of the ZZ-SNAP-SUMO3-tag was performed by on-column cleavage with His-tagged SENP2 protease (Biomolecular Screening & Protein Technologies Unit, CRG) for 1 h at RT. The cleaved ZZ-SNAP-SUMO3-tag and His-tagged SENP2 protease were then removed by an 80 CV wash step using FEZ2-LEGF buffer. Finally, FEZ2 was eluted from the StrepTrap HP column (Cytiva) via an on-column cleavage of its Strep-tag via His-tagged PreScission protease

(Biomolecular Screening & Protein Technologies Unit, CRG) for 2.5 h at 4°C. To remove the His-tagged PreScission protease during FEZ2 elution with FEZ2-LEGF buffer, a 1 mL HisTrap excel column pre-equilibrated with FEZ2-LEGF buffer was attached to the StrepTrap HP column. The eluted FEZ2 was concentrated with Amicon Ultra-15 10 kDa MWCO filters (Merck) and ultra-centrifuged (280,000 x g, 15 min, 4°C) to remove potential aggregates. FEZ2 was further purified via SEC using a Superdex® 200 Increase 10/300 GL (Cytiva) equilibrated with FEZ2-LEGF buffer, and protein-containing fractions were pooled and further concentrated using Amicon Ultra-15 30kDa MWCO filters (Merck). Final protein concentration was determined using a NanoDrop™ One/OneC Microvolume UV-Vis Spectrophotometer, and FEZ2 aliquots were flash-frozen and stored in liquid N_2.

3.3.5. Purification of SNAP-FEZ2

7-10 g of pelleted BL21-AI™ One Shot™ Chemically Competent E. coli (Invitrogen) with the corresponding plasmid for the expression of ZZ-SNAP-SUMO3-FEZ2-Strep were resuspended in 40 ml SNAP-FEZ2-LEGF buffer (100 mM NaPi, 500 mM KCl, 5 mM $MgCl_2$, 5 mM DTT, pH 7.0) supplemented with 1 cOmplete™ ULTRA EDTA-free protease inhibitor tablet (Sigma) and DNase I (Roche). Cells were lysed by sonication (3 min total: 20 s pulse on/ 30 s pulse off, 50% amplitude, 4°C), and cell debris was pelleted by centrifugation (184,000 x g, 45 min, 4°C). The supernatant was applied to a 5 ml StrepTrap HP column (Cytiva) pre-equilibrated with SNAP-FEZ2-LEGF buffer at 4°C using a peristaltic pump. The column was washed with 35 CV of SNAP-FEZ2-LEGF buffer, and ZZ-SNAP-SUMO3-FEZ2-Strep was eluted using SNAP-FEZ2-LEGF buffer supplemented with 5 mM desthiobiotin. The ZZ-tag was removed via cleavage in solution using His-tagged PreScission protease (Biomolecular Screening & Protein Technologies Unit, CRG) for 16 h at 4°C, and SNAP-SUMO3-FEZ2 was subsequently fluorescently labeled using SNAP-Surface® Alexa Fluor® 647 (NEB) with a ratio of 1:1.5 SNAP-SUMO3-FEZ2:dye at 4°C for 16 h in the presence of 2 mM DTT. Non-conjugated dye was removed using a 5 ml Zeba™ Spin Desalting Column (Thermo Fisher Scientific), and SNAP-SUMO3-FEZ2 was ultra-centrifuged (280,000 x g, 15 min, 4°C) to remove potential aggregates. SNAP-SUMO3-FEZ2 was then further purified via SEC using a Superdex® 200 Increase 10/300 GL column (Cytiva) equilibrated with SNAP-FEZ2-LEGF buffer. Protein-containing fractions were pooled and further concentrated using Amicon Ultra-15 30kDa MWCO filters (Merck). Final labeling ratio and protein concentration were determined using a NanoDrop™ One/OneC Microvolume UV-Vis Spectrophotometer, and SNAP-SUMO3-FEZ2 aliquots were flash-frozen and stored in liquid N_2.

3.3.6. Purification of RTRAF-SNAP

2.5 g of pelleted BL21-CodonPlus(DE3)-RIL E. coli (Agilent) with the corresponding plasmid for the expression of NusA-SUMO3-RTRAF-SNAP-Strep were resuspended in 40 ml RTRAF-LEGF buffer (100 mM NaPi, 700 mM KCl, 0.001% Brij-35, 3 mM $MgCl_2$, 0.7 mM BME, 50 mM L-arginine, 50 mM L-glutamate, pH 7.2) supplemented with 1 cOmplete™ ULTRA EDTA-free protease inhibitor tablet (Sigma) and DNase I (Roche). Cells were lysed by sonication (3 min total: 20 s pulse on/ 30 s pulse off, 50% amplitude, 4°C), and cell debris was pelleted by centrifugation (184,000 x g, 45 min, 4°C). The supernatant was applied to a 5 ml StrepTrap HP column (Cytiva) pre-equilibrated with RTRAF-SNAP-LEGF buffer at 4°C using a peristaltic pump. The column was washed with 40 CV of RTRAF-LEGF buffer, and removal of the NusA-SUMO3-tag was performed by on-column cleavage with His-tagged SENP2 protease (Biomolecular Screening & Protein Technologies Unit, CRG) for 16 h at 4°C. The cleaved NusA-SUMO3-tag and His-tagged SENP2 protease were then removed by a 60 CV wash step using RTRAF-LEGF buffer. RTRAF was eluted from the StrepTrap HP column (Cytiva) using RTRAF-LEGF buffer supplemented with 5 mM desthiobiotin, and concentrated with Amicon Ultra-15 10 kDa MWCO filters (Merck). In order to reload RTRAF-SNAP-Strep onto the StrepTrap HP column and to thereby wash out remaining SENP2 protease and the NusA-SUMO3-tag, desthiobiotin was removed from the buffer using PD 10 Desalting Columns (Sigma). The column was washed with 92 CV RTRAF-LEGF buffer, and RTRAF-SNAP was finally eluted via on-column cleavage using His-tagged PreScission protease (Biomolecular Screening & Protein Technologies Unit, CRG) for 16 h at 4°C. To remove the His-tagged PreScission protease during RTRAF elution with RTRAF-LEGF buffer, a 1 ml HisTrap excel column pre-equilibrated with RTRAF-LEGF buffer was attached to the StrepTrap HP column. The eluted RTRAF-SNAP was concentrated with Amicon Ultra-15 10 kDa MWCO filters (Merck), and RTRAF-SNAP was fluorescently labeled using SNAP-Surface® Alexa Fluor® 647 (NEB) with a ratio of 1:1.5 RTRAF-SNAP:dye at 15°C for 2 h in the presence of 2 mM DTT. Non-conjugated dye was removed using a 5 ml Zeba™ Spin Desalting Column (Thermo Fisher Scientific), and RTRAF-SNAP was ultra-centrifuged (280,000 x g, 15 min, 4°C) to remove potential aggregates. Final labeling ratio and protein concentration were determined using a NanoDrop™ One/OneC Microvolume UV-Vis Spectrophotometer, and RTRAF-SNAP aliquots were flash-frozen and stored in liquid N_2.

3.3.7. Purification of NudT21

3.5-5 g of pelleted BL21-AI™ One Shot™ Chemically Competent E. coli (Invitrogen) with the corresponding plasmid for the expression of ZZ-NudT21-SNAP-His were resuspended in 50 ml NudT21-LE buffer (50 mM Tris-HCl, 500 mM NaCl, 5 mM $MgCl_2$, 5 mM imidazole, 5% glycerol, 0.7 mM BME, pH 8.0) supplemented with 1 cOmplete™ ULTRA EDTA-free protease inhibitor tablet (Sigma) and DNase I (Roche). Cells were lysed with a French press (3x, 10,000 PSI, 4°C), and cell debris was pelleted by centrifugation (184,000 x g, 45 min, 4°C). The supernatant was applied to a 5 ml HisTrap Chelating HP column (Cytiva) pre-charged with $NiSO_4$ and pre-equilibrated with NudT21-LE buffer at 4°C using a peristaltic pump. The column was washed with 20 CV of NudT21-LE buffer, 5 CV of NudT21-Wash buffer (50 mM Tris-HCl, 500 mM NaCl, 5 mM $MgCl_2$, 15 mM imidazole, 5% glycerol, 0.7 mM BME, pH 8.0), and ZZ-NudT21-SNAP-His was eluted with NudT21-Elution buffer (50 mM Tris-HCl, 500 mM NaCl, 5 mM $MgCl_2$, 300 mM imidazole, 5% glycerol, 0.7 mM BME, pH 8.0). ZZ-NudT21-SNAP-His was then concentrated using Amicon Ultra-15 30 kDa MWCO filters (Merck), and the NudT21-Elution buffer was exchanged with NudT21-GF buffer (50 mM Tris-HCl, 300 mM NaCl, 5% glycerol, 2 mM DTT) using PD 10 Desalting Columns (Sigma). ZZ-NudT21-SNAP-His was further purified via SEC using a Superdex® 200 Increase 10/300 GL column (Cytiva), and the ZZ-tag and His-tag were removed by cleavage in solution via GST-tagged recombinant HRV-3C protease (SPEED BioSystems) and GST-tagged TEV protease (Biomolecular Screening & Protein Technologies Unit, CRG) for 16 h at 4°C. ZZ-NudT21-SNAP-His was concentrated using Amicon Ultra-15 30 kDa MWCO filters (Merck), and ultra-centrifuged (280,000 x g, 15 min, 4°C) to remove potential aggregates. ZZ-NudT21-SNAP-His was further purified via SEC using a Superdex® 200 Increase 10/300 GL column (Cytiva), and protein-containing fractions were pooled. Final protein concentration was determined via Bradford protein assay (Protein Assay Dye Reagent Concentrate, Bio-Rad), and NudT21 aliquots were flash-frozen and stored in liquid N_2.

3.3.8. Purification of NudT21-SNAP

3.5-5 g of pelleted BL21-AI™ One Shot™ Chemically Competent E. coli (Invitrogen) with the corresponding plasmid for the expression of ZZ-NudT21-SNAP-His were resuspended in 50 ml NudT21-LE buffer (50 mM Tris-HCl, 500 mM NaCl, 5 mM $MgCl_2$, 5% glycerol, 5 mM DTT, pH 8.0) supplemented with 1 cOmplete™ ULTRA EDTA-free protease inhibitor tablet (Sigma) and DNase I (Roche). Cells were lysed with a French press (3x, 10,000 PSI, 4°C), and cell debris was pelleted by centrifugation (184,000 x g, 45 min, 4°C). The supernatant was applied to a 5 ml

HisTrap Excel column pre-equilibrated with NudT21-SNAP-LE buffer at 4°C using a peristaltic pump. The column was washed with 20 CV of NudT21-LE buffer, 20 CV of NudT21-SNAP-Wash buffer (50 mM Tris-HCl, 1000 mM NaCl, 5 mM $MgCl_2$, 10 mM imidazole, 5% glycerol, 5 mM DTT, pH 8.0), and ZZ-NudT21-SNAP-His was eluted with NudT21-SNAP-Elution buffer (50 mM Tris-HCl, 500 mM NaCl, 5 mM $MgCl_2$, 300 mM imidazole, 5% glycerol, 5 mM DTT, pH 8.0). ZZ-NudT21-SNAP-His was then concentrated using Amicon Ultra-15 30 kDa MWCO filters (Merck), and the NudT21-SNAP-Elution buffer was exchanged with NudT21-SNAP-GF buffer (50 mM Tris-HCl, 300 mM NaCl, 5% glycerol, 2 mM DTT) using PD 10 Desalting Columns (Sigma). ZZ-NudT21-SNAP-His was re-loaded onto a 1 ml HisTrap Excel column pre-equilibrated with NudT21-SNAP-LE buffer at 4°C using a peristaltic pump, washed 3x with 15 CV NudT21-SNAP-Wash buffer supplemented with 10, 20 or 30 mM imidazole, and eluted with NudT21-SNAP-Elution buffer. ZZ-NudT21-SNAP-His was concentrated using Amicon Ultra-15 30 kDa MWCO filters (Merck), and fluorescently labeled using SNAP-Surface® Alexa Fluor® 647 (NEB) with a ratio of 1:1.5 NudT21-SNAP:dye at 4°C for 16 h in the presence of 2 mM DTT. Non-conjugated dye was removed using a 5 ml Zeba™ Spin Desalting Column (Thermo Fisher Scientific), and the ZZ-tag and His-tag were cleaved in solution via His-tagged PreScission protease (Biomolecular Screening & Protein Technologies Unit, CRG) for 1 h at 15°C. NudT21-SNAP was concentrated using Amicon Ultra-15 30 kDa MWCO filters (Merck), and ultra-centrifuged (280,000 x g, 15 min, 4°C) to remove potential aggregates. NudT21-SNAP was further purified via SEC using a Superdex® 200 Increase 10/300 GL column (Cytiva). Final labeling ratio was determined using a NanoDrop™ One/OneC Microvolume UV-Vis Spectrophotometer, while final protein concentration was determined via Bradford protein assay (Protein Assay Dye Reagent Concentrate, Bio-Rad). NudT21-SNAP aliquots were flash-frozen and stored in liquid N_2.

3.3.9. Purification of KIF5A HC and SNAP-KIF5A HC

3.5 g of pelleted cells obtained from 800 ml of Sf21 insect cell culture with the corresponding plasmid for the expression of Strep-SNAP-KIF5A HC were resuspended in 50 ml KIF5A HC-LEGF buffer (80 mM NaPi, 400 mM KCl, 5 mM $MgCl_2$, 0.001% Brij-35, 2.5 mM DTT, 0.1 mM ATP, pH 7.2) supplemented with 1 cOmplete™ ULTRA EDTA-free protease inhibitor tablet (Sigma) and DNase I (Roche). Cells were lysed with a Dounce homogenizer (2x 40 times, on ice), and cell debris was pelleted by centrifugation (184,000 x g, 45 min, 4°C). The supernatant was applied to a 5 ml StrepTrap HP column pre-equilibrated with KIF5A HC-LEGF buffer at 4°C using a peristaltic pump. The column was washed with 40 CV of KIF5A HC-LEGF buffer, and Strep-SNAP-KIF5A HC was eluted with KIF5A HC-LEGF Elution buffer (50 mM HEPES-NaOH, 50 mM arginine, 50 mM glutamate, 250 mM

glucose, 500 mM KCl, 5 mM $MgCl_2$, 2.5 mM DTT, 1 mM EDTA, 0.001% Brij-35, 10 mM ATP, 15 mM desthiobiotin, pH 8.0). KIF5A HC was then concentrated using Amicon Ultra-15 30kDa MWCO filters (Merck), and desthiobiotin was removed using PD 10 Desalting Columns (Sigma). The eluted Strep-SNAP-KIF5A HC was either incubated with His-tagged PreScission and His-tagged TEV proteases (Biomolecular Screening & Protein Technologies Unit, CRG) for the purification of KIF5A or solely with His-tagged 3C PreScission (Biomolecular Screening & Protein Technologies Unit, CRG) for the purification of SNAP-KIF5A. After incubation for 16 h at 4°C, both proteins were applied to separate 1 ml StrepTrap HP columns (Cytiva) to remove potentially uncleaved protein. SNAP-KIF5A HC was fluorescently labeled using SNAP-Surface® Alexa Fluor® 647 (NEB) with a ratio of 1:1.5 SNAP-KIF5A HC:dye at 15°C for 2 h in the presence of 2 mM DTT. Non-conjugated dye was removed using a 5 ml Zeba™ Spin Desalting Column (Thermo Fisher Scientific). KIF5A HC and SNAP-KIF5A HC were concentrated using Amicon Ultra-15 30 kDa MWCO filters (Merck), and ultra-centrifuged (280,000 x g, 15 min, 4°C) to remove potential aggregates. Both proteins were further purified via SEC using a Superose® 6 Increase 10/300 GL (Cytiva), and protein-containing fractions were pooled. The concentrations of KIF5A HC and SNAP-KIF5A HC were determined by SDS-PAGE analysis in comparison to a BSA standard, and labeling ratio was finally determined using a NanoDrop™ One/OneC Microvolume UV-Vis Spectrophotometer. Purity of both proteins was determined via SDS-PAGE, and KIF5A HC and SNAP-KIF5A HC aliquots were flash-frozen and stored in liquid N_2.

3.3.10. Purification of KIF5A/KLC4

3.5 g of pelleted Sf21 cells with the corresponding plasmid for the co-expression of Strep-SNAP-KIF5A HC and KLC4 were resuspended in 40 ml KIF5A HC/KLC4-LEGF buffer (80 mM NaPi, 250 mM KCl, 5 mM $MgCl_2$, 0.001% Brij-35, 2.5 mM DTT, 2.5 mM EDTA, 0.1 mM ATP, pH 7.2) supplemented with 2 cOmplete™ ULTRA EDTA-free protease inhibitor tablets (Sigma) and DNase I (Roche). Cells were lysed with a Dounce homogenizer (2x 40 times, on ice), and cell debris was pelleted by centrifugation (184,000 x g, 45 min, 4°C). The supernatant was applied to a 5 ml StrepTrap HP column (Cytiva) pre-equilibrated with KIF5A/KLC4-LEGF buffer at 4°C using a peristaltic pump. The column was washed with 20 CV of KIF5A/KLC4-LEGF buffer, the Strep-SNAP-KIF5A/KLC4 complex was eluted with KIF5A/KLC4-LEGF buffer supplemented with 10 mM desthiobiotin, and desthiobiotin was then removed using PD 10 Desalting Columns (Sigma). The eluted Strep-SNAP-KIF5A/KLC4 complex was incubated with His-tagged TEV protease (Biomolecular Screening & Protein Technologies Unit, CRG) for 16 h at 4°C for the purification of KIF5A/KLC4. The KIF5A/KLC4 complex was then concentrated using Amicon Ultra-15 30kDa MWCO filters (Merck), and ultra-centrifuged (280,000 x g, 15 min, 4°C) to remove

potential aggregates. The KIF5A/KLC4 complex was further purified via SEC using a Superdex® 200 Increase 10/300 GL column (Cytiva). It was then concentrated using Amicon Ultra-4 30kDa MWCO filters (Merck) and final protein concentration was determined via Bradford protein assay (Protein Assay Dye Reagent Concentrate, Bio-Rad). Purity of the complex was determined via SDS-PAGE, and KIF5A/KLC4 aliquots were flash-frozen and stored in liquid N_2.

3.3.11. Purification of SNAP-KIF5A/KLC4

3.5 g of pelleted Sf21 cells with the corresponding plasmid for the co-expression of Strep-SNAP-KIF5A HC and KLC4 were resuspended in 40 ml SNAP-KIF5A HC/KLC4-LEGF buffer (80 mM NaPi, 200 mM KCl, 5 mM $MgCl_2$, 0.001% Brij-35, 2.5 mM DTT, 2.5 mM EDTA, 0.1 mM ATP, pH 7.2) supplemented with 1 cOmplete™ ULTRA EDTA-free protease inhibitor tablet (Sigma) and DNase I (Roche). Cells were lysed with a French press (2x, 2,500 PSI, 4°C), and cell debris was pelleted by centrifugation (184,000 x g, 45 min, 4°C). The supernatant was applied to a 5 ml StrepTrap HP column (Cytiva) pre-equilibrated with SNAP-KIF5A HC/KLC4-LEGF buffer at 4°C using a peristaltic pump. The column was washed with 40 CV of SNAP-KIF5A HC/KLC4-LEGF buffer, the Strep-SNAP-KIF5A HC/KLC4 complex was eluted with SNAP-KIF5A HC/KLC4-LEGF buffer supplemented with 10 mM desthiobiotin, and the His-tag was cleaved in solution via His-tagged PreScission protease (Biomolecular Screening & Protein Technologies Unit, CRG) for 1 h at 20°C. The SNAP-KIF5A HC/KLC4 complex was then concentrated using Amicon Ultra-15 30kDa MWCO filters (Merck), and ultra-centrifuged (280,000 x g, 15 min, 4°C) to remove potential aggregates. The SNAP-KIF5A/KLC4 complex was further purified via SEC using a Superdex® 200 Increase 10/300 GL column (Cytiva), and fluorescently labeled using SNAP-Surface® Alexa Fluor® 647 (NEB) with a ratio of 1:1.5 SNAP-KIF5A HC/KLC4:dye at 4°C for 16 h in the presence of 2 mM DTT. Non-conjugated dye was removed using a 5 ml Zeba™ Spin Desalting Column (Thermo Fisher Scientific), and final protein concentration was determined via Bradford protein assay (Protein Assay Dye Reagent Concentrate, Bio-Rad). Since only the KIF5A HC is SNAP-tagged, the concentration of the latter was determined by SDS-PAGE in comparison to a BSA standard, and labeling ratio was finally determined using a NanoDrop™ One/OneC Microvolume UV-Vis Spectrophotometer. Purity of the complex was determined via SDS-PAGE, and AF647-KIF5A HC/KLC4 aliquots were flash-frozen and stored in liquid N_2.

3.3.12. Purification of KIF5A/KLC4-SNAP

4.5 g of pelleted Sf21 cells with the corresponding plasmid for the co-expression of Strep-KIF5A and KLC4-SNAP-His were resuspended in 40 ml KIF5A/KLC4-SNAP-LEGF buffer (80 mM NaPi, 200 mM KCl, 5 mM $MgCl_2$, 0.001% Brij-35, 2.5 mM DTT, 2.5 mM EDTA, 0.1 mM ATP, pH 7.2) supplemented with 1 cOmplete™ ULTRA EDTA-free protease inhibitor tablet (Sigma) and DNase I (Roche). Cells were lysed with a Dounce homogenizer (2x 30 times, 4°C), and cell debris was pelleted by centrifugation (184,000 x g, 45 min, 4°C). The supernatant was applied to a 5 ml HisTrap Excel column (Cytiva) pre-equilibrated with KIF5A/KLC4-SNAP-LEGF buffer at 4°C using a peristaltic pump. The column was washed with 26 CV of KIF5A/KLC4-SNAP-His Wash buffer (80 mM NaPi, 200 mM KCl, 5 mM $MgCl_2$, 0.001% Brij-35, 2.5 mM DTT, 2.5 mM EDTA, 0.1 mM ATP, 10 mM imidazole, pH 7.2), and a 1 ml StrepTrap HP column equilibrated with KIF5A/KLC4-SNAP-His Elution buffer (80 mM NaPi, 200 mM KCl, 5 mM $MgCl_2$, 0.001% Brij-35, 2.5 mM DTT, 2.5 mM EDTA, 0.1 mM ATP, 400 mM imidazole, pH 7.2) was attached to its bottom. The columns were washed with 6 CV of KIF5A/KLC4-SNAP-His Elution buffer, and the Strep-KIF5A/KLC4-SNAP-His complex was eluted with KIF5A/KLC4-SNAP-LEGF buffer supplemented with 5 mM desthiobiotin. The His- and Strep-tags were cleaved in solution via His-tagged PreScission protease (Biomolecular Screening & Protein Technologies Unit, CRG) for 18 h at 4°C. The KIF5A/KLC4-SNAP complex was then concentrated using Amicon Ultra-15 30 kDa MWCO filters (Merck), and ultra-centrifuged (280,000 x g, 15 min, 4°C) to remove potential aggregates. The KIF5A/KLC4-SNAP complex was further purified via SEC using a Superdex® 200 Increase 10/300 GL column (Cytiva), and fluorescently labeled using SNAP-Surface® Alexa Fluor® 647 (NEB) with a ratio of 1:1.5 KIF5A/KLC4-SNAP:dye at 4°C for 16 h in the presence of 2 mM DTT. Non-conjugated dye was removed using a 5 ml Zeba™ Spin Desalting Column (Thermo Fisher Scientific), and final protein concentration was determined via Bradford protein assay (Protein Assay Dye Reagent Concentrate, Bio-Rad). Since only KLC4 is SNAP-tagged, the concentration of the latter was determined by SDS-PAGE in comparison to a BSA standard, and labeling ratio was finally determined using a NanoDrop™ One/OneC Microvolume UV-Vis Spectrophotometer. Purity of the complex was determined via SDS-PAGE, and KIF5A/KLC4-SNAP aliquots were flash-frozen and stored in liquid N_2.

3.4. Purification of bovine brain tubulin

Tubulin was purified from bovine brains according to a published protocol (Castoldi and Popov 2003). In brief, the protocol consists of two consecutive cycles of tubulin

polymerization and depolymerization in a high-molarity PIPES buffer, resulting in the efficient removal of contaminant MAPs. Purity of depolymerized tubulin was determined via SDS-PAGE, tubulin concentration was determined using a NanoDrop™ One/OneC Microvolume UV-Vis Spectrophotometer, and tubulin aliquots were flash-frozen and stored in liquid N_2.

3.5. Biotinylation and fluorescent labeling of bovine tubulin

For subsequent usage in TIRF-M-based in vitro motility assays, purified bovine tubulin was labeled using ATTO 390 NHS-ester (ATTO-TEC GmbH) or biotinylated using EZ-Link™ NHS-Biotin (Thermo Fisher Scientific). Both reactions were performed according to a published protocol (Hyman et al. 1991) with modifications. In general, the procedures include fluorescent labeling and biotinylation, respectively, of polymerized tubulin, resulting in a protection of those residues that are required for tubulin assembly into microtubules. The modification of bovine brain tubulin is performed at a high pH to enable the reaction of NHS-ester activated biotin and fluorescent dyes with primary amines of tubulin. Additionally, functional tubulin is separated from dysfunctional or aggregated tubulin with the help of two consecutive cycles of tubulin polymerization and depolymerization. The complete modification procedure is described below.

130 µM tubulin were polymerized in pre-warmed B80 buffer (80 mM PIPES-KOH, 3 mM $MgCl_2$ 1 mM EGTA, pH 6.8) in a total volume of 4 ml. 3 ml pre-warmed glycerol were added, and the mixture was incubated for 40 min at 37°C. Polymerized tubulin was then layered on a 9 ml warm high pH cushion (100 mM HEPES-NaOH, 3 mM $MgCl_2$, 1 mM EGTA, 60% (v/v) glycerol, pH 8.2), and microtubules were pelleted by centrifugation using a 70 Ti rotor (Beckman Coulter) (40,000 rpm, 45 min, 35°C, slow acceleration/deceleration). The supernatant above the cushion was removed and the supernatant/cushion interface was washed twice with 1.5 ml warm labeling buffer (100 mM HEPES-NaOH, 2 mM $MgCl_2$, 1 mM EGTA, 40% (v/v) glycerol, 0.5 mM GTP, pH 8.2). The microtubule pellet was then resuspended in 1.5 ml warm labeling buffer with a cut pipette tip. Assuming a polymerization efficiency of 70%, 243 µM tubulin were then either biotinylated using a 25-fold molar excess of EZ-Link™ NHS-Biotin (Thermo Fisher Scientific) or fluorescently labeled using a 25-fold molar excess of ATTO 390 NHS-ester (ATTO-TEC GmbH) in the presence of 2 mM GTP in warm labeling buffer in a total volume of 4.5 ml. The mixture was incubated for 20-40 min at 37°C, and then layered on a 1 ml warm low pH cushion (80 mM PIPES-KOH, 3 mM $MgCl_2$ 1 mM EGTA, 60% (v/v) glycerol, pH 6.8). Microtubules were pelleted by centrifugation using a TLA 100.3 rotor (Beckman Coulter) (80,000 rpm, 30 min, 35°C, slow acceleration/deceleration). The supernatant above the cushion

was removed, and the supernatant/cushion interface was washed twice with warm B80 buffer. Microtubules were then resuspended in 1.5 ml cold depolymerization buffer (50 mM glutamate-KOH, 1 mM EGTA) and incubated on ice for 30 min. Depolymerized tubulin was centrifuged in a 120.2 rotor (Beckman Coulter) (80,000 rpm, 10 min, 2°C, slow acceleration/deceleration). After removal of potential aggregates, the tubulin-containing supernatant was subjected to a second polymerization step: Tubulin was polymerized in the presence of 2 mM GTP in warm B80 buffer in a total volume of 4 ml. ½ volumes of pre-warmed glycerol were added, and the mixture was incubated at 37°C for 30 min. Polymerized tubulin was then again layered on a warm low pH cushion, and microtubules were pelleted by centrifugation using a TLA 100.3 rotor (Beckman Coulter) (80,000 rpm, 30 min, 35°C, slow acceleration/deceleration). The supernatant above the cushion was removed, and the supernatant/cushion interface was washed twice with warm B80 buffer. Microtubules were then resuspended in 0.2 ml cold depolymerization buffer (50 mM glutamate-KOH, 1 mM EGTA) and incubated on ice for 30 min. Depolymerized tubulin was centrifuged in a 120.2 rotor (Beckman Coulter) (80,000 rpm, 10 min, 2°C, slow acceleration/deceleration). After removal of potential aggregates, the tubulin-containing supernatant was recovered, and tubulin concentration (and labeling ratio of fluorescent tubulin) was determined using a NanoDrop™ One/OneC Microvolume UV-Vis Spectrophotometer. Purity of biotinylated and fluorescent tubulin, respectively, was determined via SDS-PAGE, and tubulin aliquots were flash-frozen and stored in liquid N_2.

3.6. Polymerization and stabilization of microtubules

Microtubules for in vitro motility assays were polymerized from bovine brain tubulin with a stochastic incorporation of ATTO 390 (ATTO-TEC GmbH)-labeled and biotinylated tubulin: 36 µM unlabeled tubulin were mixed with 14 µM ATTO 390-labeled and 10 µM biotinylated tubulin, and the mixture was incubated in BRB80 (80 mM PIPES-KOH, 2 mM MgCl2, 1 mM EGTA, pH 6.8) in the presence of 4 mM GTP for 25 min at 37°C in a total volume of 50 ul. 400 ul pre-warmed BRB80 supplemented with 20 µM taxol (Sigma) were added, and the mixture was incubated for 60 min at 37°C. Polymerized microtubules were then pelleted by centrifugation (20,000 x g, 5 min, RT), and microtubules were carefully resuspended in 50 µl BRB80 supplemented with 20 µM taxol.

3.7. TIRF-M-coupled in vitro reconstitution assays

TIRF-M-coupled in vitro reconstitution assays including motility chamber preparation, in vitro motility assays as well as the analysis of TIRF-M data were

performed and analyzed as extensively described in (Grawenhoff, Baumann, and Maurer 2022) with minor modifications. The procedures will be briefly summarized in the following sections.

3.7.1. Motility chamber preparation

Motility chambers with a volume of ~10 ul were prepared as described previously (Bieling et al. 2010). Glass cover slips functionalized with biotin-PEG (Microsurfaces Inc, USA) were attached to glass slides previously washed in 1 M NaOH, H_2O and EtOH as well as passivated with poly(L-lysine)-PEG (PLL(20)-g[3.5]-PEG(2), PLL-PEG, SuSos AG) using 2 parallel strips of double-sided tape. Motility chambers were additionally passivated for 5 min on ice by flushing with 5% (w/v) Pluronic F-127 in TIRF-M assay buffer (90 mM HEPES, 10 mM PIPES, 2.5 mM $MgCl_2$, 1.5 mM EGTA, 15 mM BME, pH 6.95) supplemented with 50 µg/ml κ-casein, and subsequently flushed with 25 µg/ml Neutravidin (Invitrogen) in TIRF-M assay buffer containing 200 µg/ml κ-casein. The motility chambers were washed immediately with TIRF-M assay buffer and placed at RT for 3 min. Taxol-stabilized microtubules diluted in RT TIRF-M assay buffer were added to the motility chambers and incubated for an additional 3 min to ensure their successful coupling to the biotinylated coverslips via interaction with NeutrAvidin.

3.7.2. In vitro motility assays

Prior to motility chamber passivation and preparation, in vitro motility assay components were pre-diluted and pre-incubated on ice 18 ± 1 min in TIRF-M assay buffer supplemented with 1.2% PEG-3350 (Sigma), and 0.5 U/µl SUPERase•In™ RNase Inhibitor (Invitrogen). Individual pre-incubation mixes include motor proteins, RBPs and RNA (purchased from IBA Lifesciences) in nM to µM range (note: (SNAP-)SRSF3 was always added to the pre-incubation mix immediately before adding it to the final RT motility buffer due to its purification at room temperature). Pre-incubation mixes were then diluted 65-fold into the final motility buffer (TIRF-M assay buffer supplemented with 0.32 mg/ml glucose oxidase (SERVA), 0.275 mg/ml catalase (Sigma), 50 mM glucose (Sigma), 50 µg/ml β-casein and 0.12% methylcellulose (Sigma)). Protein and RNA concentrations for individual assays are described in figure legends. TIRF-M motility mixes were finally added to motility chambers containing pre-immobilized microtubules, and chambers were sealed with nail polish for imaging of 5 min movies at 30 ± 1°C.

3.7.3. TIRF-M

Microscopy data was acquired using a custom-built TIRF microscope (TILL Photonics) using a 100x 1.49 N.A. objective lens (Olympus) and four laser lines: 405 nm, 488 nm, 561 nm, 639 nm. Individual laser powers as well as exposure times and acquisition frame rates were kept constant for all experiments in order to ensure comparability between different experiment sets/conditions. Before acquiring microscopy data, all channels were aligned by recording images with TetraSpeck™ Microspheres (0.1 µm, fluorescent blue/green/orange/dark red, Invitrogen) in all channels on a daily basis. Triple color imaging was achieved by alternate recording of two distinct channels corresponding to laser lines 561 nm and 639 nm. Movies were recorded with four frames per second (FPS, 250 ms or 125 ms exposure per channel). ATTO 390-labeled microtubules in each experiment were recorded as single snapshots (800 ms exposure) immediately before and after alternating time-lapse movies via laser line 405 nm. This “snapshot (405 nm) / time-lapse (alternating 561 nm and 639 nm) / snapshot (405 nm)” protocol was chosen due to the fast bleaching of the ATTO 390 dye in comparison to other fluorescent dyes, and enabled a control of microtubule positioning before and after time-lapse recordings. Double color imaging was achieved by a similar protocol with two snapshots (laser line 405 nm, 800 ms exposure) for the imaging of ATTO 390-labeled microtubules immediately before and after imaging with a single laser line (561 nm or 639 nm / 250 ms or 125 ms exposure).

3.7.4. Analysis of TIRF-M data

To analyze the dynamic properties of kinesin-1-RBP as well as kinesin-1-RBP-RNA complexes (kinesin-1 ribonucleoproteins (kinesin-1 RNPs)), TIRF-M movies were analyzed with the FIJI plug-in TrackMate, as described previously (Grawenhoff, Baumann, and Maurer 2022) and commonly used for single-molecule tracking (S. Baumann et al. 2020; S. J. Baumann et al. 2022). TrackMate enables the tracking of particles at single-molecule intensity, and for all TIRF-M-based experiments and conditions, entire movies (5 min) and field of views (60 x 60 µm) were analyzed. Single particles were detected with the help of the Difference of Gaussian (DoG) detector by setting the Estimated Blob Diameter to 800 nm. Intensity thresholds depend on laser wavelength, laser power and fluorophore concentration, and were typically set to 25-40 nm. Trajectories of kinesin-1-RBP complexes and kinesin-1-RNPs were analyzed using the Linear Motion Tracker (LMT) with pre-defined settings (Maximal Linking Distance=600 nm, Maximal Gap-Closing Distance=600 nm, Maximal Frame Gap=2). Although no diffusive movement of kinesin-1 could be detected, several RBPs showed diffusive behavior on microtubules in the absence

of kinesin-1. To exclude these diffusive events from the analysis, only trajectories with a Maximum Distance Traveled > 4,000 nm were taken into account. All parameters used for the analysis of dynamic properties of kinesin-1-RBP complexes as well as kinesin-1-RNPs were kept constant between experiment sets, so that different conditions could be compared.

3.8. Mass photometry

The potential interaction of different proteins as well as monomeric or multimeric states of individual proteins and were analyzed via mass photometry using a One MP mass photometer (Refeyn). Proteins were diluted in their respective RT purification buffers or RT TIRF-M assay buffer to a final concentration of 10 – 20 nM in a sample well (3 mm diameter, Refeyn) pre-assembled on a glass sample carrier slide (Refeyn) and placed in the mass photometer for immediate imaging. If more than one protein was analyzed, proteins were pre-incubated on ice or at RT for ~ 10 min at a 10-fold higher concentration to facilitate interactions. Molecular weights of individual proteins or protein complexes were assigned via comparison with calibration probes with known molecular weights in each buffer. Background intensities generated by the different buffers used were subtracted for each experiment.

4. KINESIN-1 AND DYNEIN CAN INTERACT WITH NXF1

4.1. Results

The aim of this thesis was to analyze whether the selected rec-YnH network interactions (Figure 11), comprising microtubule motor protein light chains and the RBPs NXF1 and SRSF3, can result in the formation of a complex that transports mRNA along microtubules.

To determine how individual factors within the complex interact with one another, we opted for an in vitro reconstitution approach with single-molecule sensitivity.

4.1.1. NXF1 harbors kinesin-1 and dynein light chain interaction motifs

To understand how NXF1 might interact with the kinesin-1 and dynein light chains KLC4 and Tctex1, respectively, we first analyzed whether NXF1 harbors any known interaction motifs.

The dynein light chain Tctex1 is reported to interact with a variety of target proteins via an R/K-R/K-x-x-R/K consensus sequence (x: any amino acid) (Mok, Lo, and Zhang 2001). We hence analyzed the NXF1 amino acid sequence and were able to find this motif twice: One Tctex1 motif is found in its RRM (K^{22}-K^{23}-K^{24}-G^{25}-R^{26}), whereas the second motif is located in its ΨRRM (R^{128}-K^{129}-Y^{130}-D^{131}-K^{132}).

Although target recognition via kinesin-1 light chains is not fully understood, there are a few interaction motifs that have been identified in previous studies. Kinesin-1 light chain 2 (KLC2), for example, is reported to interact with a target protein, C-Jun N-terminal kinase interacting protein (JIP3), via a hydrophobic patch in the leucine zipper of the latter (Ala^{437}-Leu^{438}-Val^{441}-Leu^{445}-Ile^{446}), thereby relieving kinesin-1 autoinhibition (Cockburn et al. 2018). The KLC2 hydrophobic amino acid residues that interact with JIP3 are highly conserved in all kinesin-1 light chains, including KLC4. Interestingly, we found that NXF1 harbors a hydrophobic patch (Ala^{171}-Leu^{172}-Val^{175}-Ile^{179}-Leu^{180}) in its ΨRRM that is highly similar to the JIP3 hydrophobic patch. Alternatively, KLCs are also reported to interact with several other proteins (Aoyama et al. 2009; Araki et al. 2007; Dodding et al. 2011; Kawano et al. 2012; Konecna et al. 2006; Rosa-Ferreira and Munro 2011; Schmidt et al. 2009) via a tryptophan-acidic motif (Pernigo et al. 2013), in which the central tryptophan is flanked by acidic amino acid residues such as glutamate and aspartate (e.g. EWD). Interestingly, analysis of the NXF1 amino acid sequence revealed that it also harbors two of these tryptophan-

acidic motifs (E^{583}-W^{584} and W^{594}-D^{595}) in its NTF2L and ubiquitin-associated domains, respectively.

Besides harboring two dynein light chain interaction motifs, NXF1 thus also harbors two KLC4 interaction motifs that could account for the identified rec-YnH-based interaction between NXF1 and kinesin-1/dynein.

4.1.2. Development of a TIRF-M-based in vitro reconstitution approach

To study the novel rec-YnH-based interactions, we developed an in vitro reconstitution approach (Grawenhoff, Baumann, and Maurer 2022) which is based on previously published methods (Bieling et al. 2010) and has been successfully employed in other studies from the Maurer group (S. Baumann et al. 2020; S. J. Baumann et al. 2022). This approach (see section 1.7.3 and Figure 16 for a detailed explication) includes the preparation of biotinylated TIRF-M chambers (Supplementary Figure 1) in which fluorescently labeled, biotinylated and taxol-stabilized microtubules (Figure 17) are immobilized via NeutrAvidin, a deglycosylated avidin that has four biotin binding pockets. Microtubule motor proteins (kinesin-1 and dynein) as well as RBPs and mRNAs are then added to these TIRF-M chambers, and can subsequently be analyzed for their interaction with microtubules and/or one another.

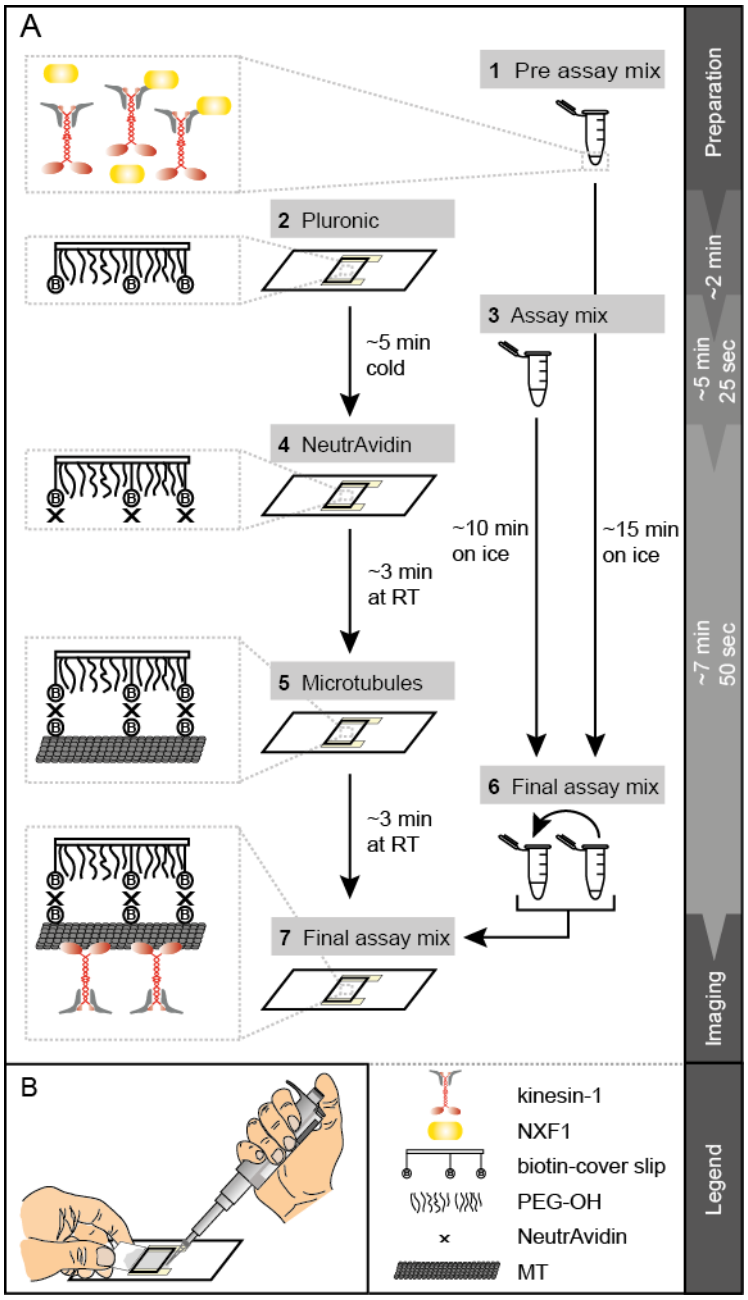

Figure 16: Schematic representation of the individual steps performed in TIRF-M in vitro reconstitution experiments. (A) Preparation proceeds according to the numbered steps: (1) Proteins imaged in each TIRF-M experiment are pre-incubated on ice for ~15 min to increase the propensity of complex formation (when >1 protein is used, in this case kinesin-1 and NXF1). In the meantime, TIRF-M chambers are passivated (2) and the assay mix is prepared (3). The assay mix includes the reagents ATP, glucose, oxygen scavengers as well as blocking and crowding agents (compare with section 3.7.2). After adding NeutrAvidin to the TIRF-M chambers (4), fluorescent and biotinylated microtubules (see Figure 17) are flown into the TIRF-M chambers (5). After an incubation time of ~3 min at room temperature (RT), the pre assay mix is added to the assay mix, forming the final assay mix (6) that is added to the TIRF-M chambers (7). The chambers are then immediately

sealed and imaged for 5 min. **(B)** Schematic representation of how individual mixes are added into TIRF-M chambers. Image originally from (Grawenhoff, Baumann, and Maurer 2022).

In a first test, we analyzed whether polymerized and taxol-stabilized microtubules, consisting of unmodified as well as fluorescently labeled and biotinylated bovine tubulin (Figure 17), were stable within the typical imaging time of 5 min. We therefore performed a TIRF-M experiment in which we imaged microtubules at the beginning (0 sec) and at the end of each 5 min movie (300 sec). TIRF-M images show that microtubules are stable and remain at the same position to which they initially attached (Figure 17B), confirming that the developed TIRF-M in vitro reconstitution approach is suitable for the analysis of motor protein motility and potential RBP/mRNA transport along microtubules.

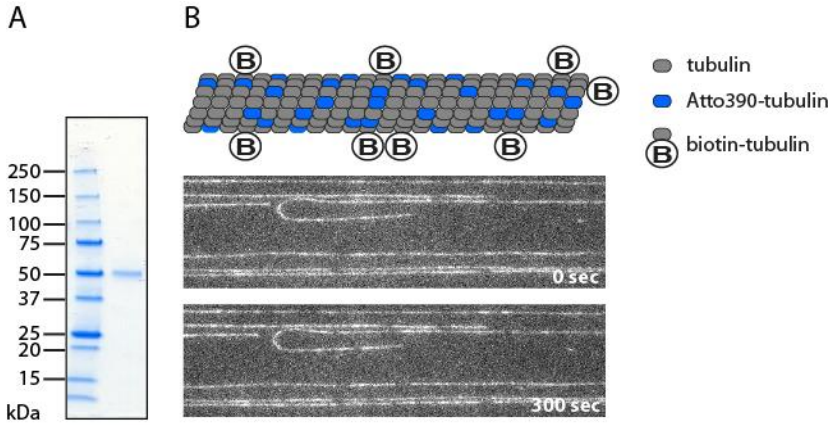

Figure 17: Microtubule purity and stability. (A) Coomassie-stained SDS-PAGE gel of purified α- and β-tubulin monomers. The latter migrate at the expected molecular weight of 55 kDa. **(B)** Top: Schematic of microtubules used in TIRF-M in vitro reconstitution assays. They consist of a mixture of unmodified, fluorescently labeled (Atto390) and biotinylated bovine tubulin. Bottom: Taxol-stabilized microtubules are stable over the imaging period of 5 min. For simplicity, microtubules in subsequent figures are represented only with unmodified bovine tubulin, although the experimental setup for every performed experiment is identical to the here presented microtubule assembly.

4.1.3. Purification of microtubule motor proteins

Having confirmed the stability of microtubules in the in vitro reconstitution experiments, the next step in testing the novel rec-YnH-based interactions consisted in obtaining purified microtubule motor proteins and testing their activity in vitro reconstitution assays.

The dynein complex was kindly provided by Andrea Tassinari (Maurer group). For the kinesin-1 heterotetramer, we chose to express and purify the neuron-specific

KIF5A heavy chain isoform (Kanai et al. 2000) in combination with KLC4. Three heterotetramers were purified: unlabeled kinesin-1 heterotetramer (KIF5A/KLC4, purified by Silvia Speroni (Maurer group)), heavy chain-labeled kinesin-1 heterotetramer (AF647-KIF5A/KLC4, purified by Silvia Speroni (Maurer group)) and light chain-labeled kinesin-1 heterotetramer (KIF5A/KLC4-AF647, purified in this thesis).

Cloning, expression and purification protocols for all three kinesin-1 heterotetramers are explained in detail in sections 3.1, 3.2 and 3.3. Each of the co-expressed heterotetramers contained tags improving solubility (ZZ-tag), as well as enabling both affinity chromatography (His- and Strep-tags) and fluorescent labeling (SNAP-tag), all of which were cleavable via 3C and TEV proteases. The unlabeled heterotetramer (KIF5A/KLC4) and the heavy chain-labeled heterotetramer (AF647-KIF5A/KLC4) were purified by Strep-tag affinity chromatography, pulling exclusively on Strep-tagged (SNAP-)KIF5A HC, resulting in the purification of heterotetramers by complex formation of (SNAP-)KIF5A HC with KLC4. Since this protocol led to an excess of KIF5A HC over KLC4 (Figure 18C), the protocol for the purification of the light chain-labeled heterotetramer (KIF5A/KLC4-AF647) was adjusted: A His-tag was added to the KLC4 construct to enable an additional immobilized metal ion affinity chromatography step besides the Strep-tag affinity chromatography step.

Using this double affinity chromatography approach, which is demonstrated in Figure 18A-B, we tried to prevent the co-purification of KIF5A HC dimers lacking KLC4 (or KLC4-AF647 monomers). Yet, for all three kinesin-1 heterotetramers, the excess of (SNAP-)KIF5A HC over KLC4(-SNAP) can be observed throughout the purifications, as visualized by the size exclusion chromatograms (Supplementary Figure 2) as well as in the final preparations, as shown in the SDS-PAGE analyses (Figure 18C). The higher KIF5A HC yield becomes especially visible in the KIF5A/KLC4-AF647 size exclusion chromatogram, in which the AF647 signal (corresponding to KLC4) is present in a smaller side peak next to the main absorption peak at 280 nm. Accordingly, SDS-PAGE analysis shows that KLC4 is gradually lost in the size exclusion chromatography fractions eluting in the main 280 nm absorbance peak (Figure 18B).

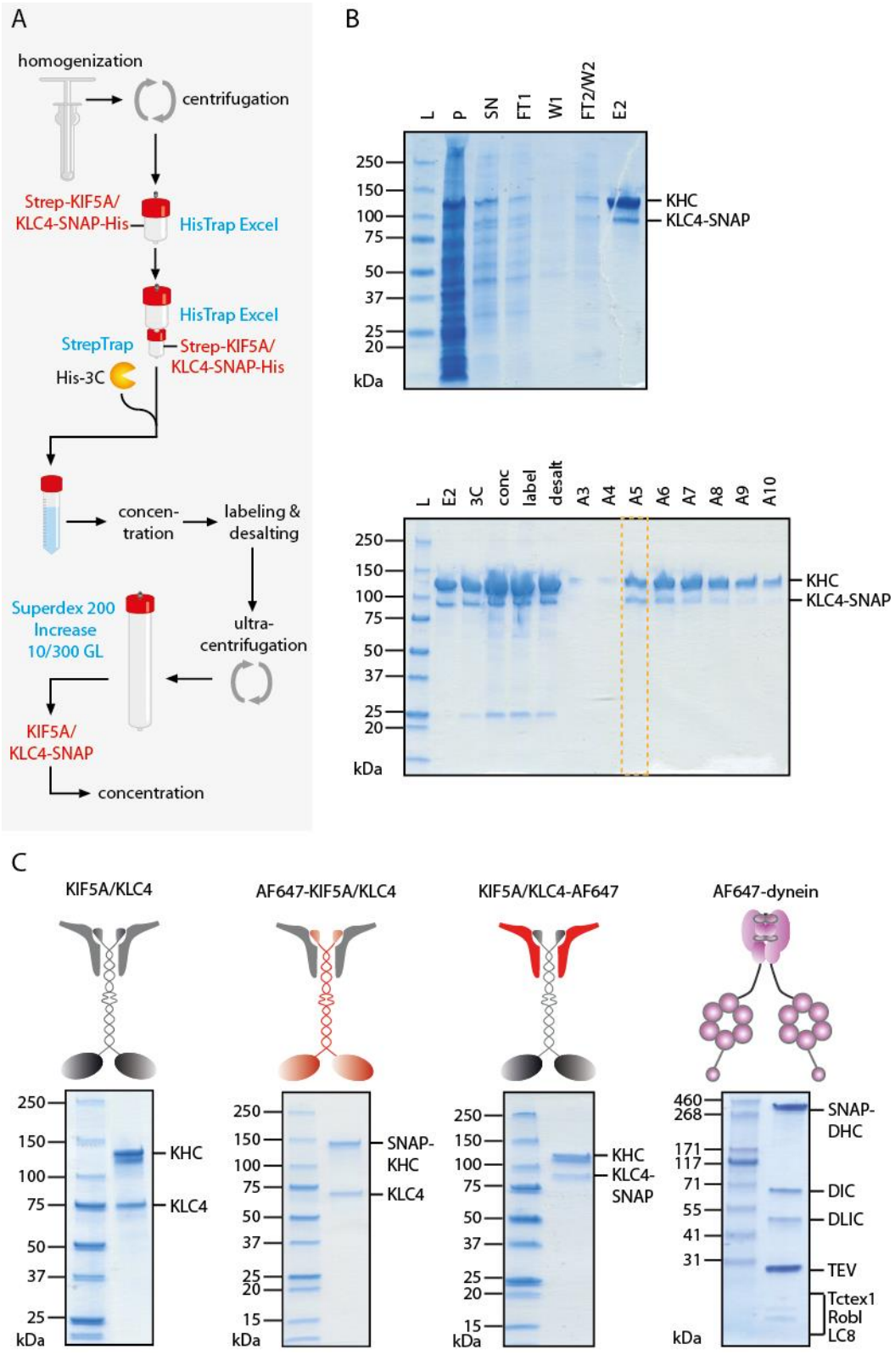
A
homogenization
centrifugation
Strep-KIF5A/
KLC4-SNAP-His
HisTrap Excel
HisTrap Excel
StrepTrap
Strep-KIF5A/
KLC4-SNAP-His
His-3C
concen-
tration
labeling &
desalting
Superdex 200
Increase
10/300 GL
ultra-
centrifugation
KIF5A/
KLC4-SNAP
concentration
B
L
P
SN
FT1
W1
FT2/W2
E2
250
150
100
75
50
37
25
20
kDa
KHC
KLC4-SNAP
L
E2
3C
conc
label
desalt
A3
A4
A5
A6
A7
A8
A9
A10
250
150
100
75
50
37
25
20
kDa
KHC
KLC4-SNAP
C
KIF5A/KLC4
AF647-KIF5A/KLC4
KIF5A/KLC4-AF647
AF647-dynein
250
150
100
75
50
37
25
kDa
KHC
KLC4
250
150
100
75
50
37
25
20
15
kDa
SNAP-
KHC
KLC4
250
150
100
75
50
37
25
20
15
kDa
KHC
KLC4-
SNAP
460
268
171
117
71
55
41
31
kDa
SNAP-
DHC
DIC
DLIC
TEV
Tctex1
Robl
LC8

Figure 18: Purification of microtubule motor proteins. Three different kinesin-1 heterotetramers (KIF5A/KLC4, AF647-KIF5A/KLC4 and KIF5A/KLC4-AF647) were purified. (**A**) The purification protocol used for the purification of KIF5A/KLC4-AF647. **(B)** Coomassie-stained SDS-PAGE gels show the purification of KIF5A/KLC4-SNAP according to (A). L: molecular weight protein ladder, P: pellet, SN: supernatant, FT1: flow-through (HisTrap Excel column), W1: wash (HisTrap Excel column), FT2/W2: flow-through/wash (StrepTrap HP column), E2: elution (StrepTrap HP column), 3C: PreScission protease (3C) cleavage, conc: concentration, ultrac: ultracentrifugation, label: labeling with AF647 dye, desalt: desalting, A3-A10: fractions in size exclusion chromatography. The dashed orange rectangle shows which samples were chosen for further purification following size exclusion chromatography. The corresponding size exclusion chromatogram is shown in Supplementary Figure 2 together with the chromatograms of the other two kinesin-1 heterotetramers. **(C)** Final Coomassie-stained SDS-PAGE gel showing the three purified kinesin-1 heterotetramers as well as AF647-dynein. KIF5A/KLC4-AF647 was purified in this thesis, whereas AF647-KIF5A/KLC4 and KIF5A/KLC4 were purified by Silvia Speroni (Maurer group). AF647-dynein was obtained from Andrea Tassinari (Maurer group).

To verify whether the final preparations of the three kinesin-1 complexes comprise heterotetramers consisting of two copies of KIF5A HC as well as two copies of KLC4, mass photometry analyses were performed. Mass photometry is a novel tool used to analyze the oligomeric state of proteins on a single-molecule basis. The method relies on the ability of proteins to scatter light, resulting in distinct mass photometry contrasts that can be directly correlated with a protein's molecular mass (Supplementary Figure 4). The obtained mass photometry results for all three purified kinesin-1 complexes (Supplementary Figure 5) show the presence of heterotetramer peaks. Of note, each purification sample also includes minor (1) lower molecular mass peaks corresponding to (SNAP-)KHC dimers and uncomplexed KLC4(-SNAP) as well as (2) higher molecular mass peaks corresponding to (SNAP-)KHC tetramers.

Finally, in SDS-PAGE analyses, both (SNAP-)KIF5A HC and KLC4(-SNAP) migrated at their expected molecular weights (Figure 18C). Interestingly, (SNAP-)KIF5A HC migrates as a double band (especially visible for the purified, unlabeled KIF5A/KLC4 heterotetramer) whenever the resolution is sufficient. To exclude the possibility of having co-purified a contaminant or a fragment, we confirmed via mass spectrometric analyses (data not shown) that the amino acid sequence of the protein in the second KIF5A HC band is identical to the first, and thus possibly results from distinct posttranslational modifications.

4.1.4. Kinesin-1 and dynein show distinct processivities in TIRF-M assays

Having purified kinesin-1 and dynein, we next analyzed whether the individual motor protein complexes are functional and processive. We expected both microtubule

motor proteins to be autoinhibited as described in the literature (see section 1.5.1). Initial TIRF-M experiments (Figure 19) confirmed that both microtubule motor proteins were able to bind to microtubules. In our experiments, dynein appears to be predominantly autoinhibited, with its motility characterized mostly by diffusion with occasional directed events. Contrary to our expectations (see section 1.5.1), microtubule-bound kinesin-1 does not appear to be autoinhibited, as visualized by processive movement of AF647-KIF5A/KLC4. To exclude the possibility that the SNAP-tag, which was placed at the N-terminus of the KIF5A heavy chain of the kinesin-1 heterotetramer construct (AF647-KIF5A/KLC4), had an effect on motility, we also tested a C-terminally SNAP-tagged heterotetramer (KIF5A-AF647/KLC4, data not shown), similar to the C-terminally mScarlet-tagged kinesin-1 used by the McKenney group (Chiba et al. 2022). Both of our kinesin-1 heterotetramer preparations showed a similar motility phenotype, suggesting that the placement of fluorescent tags does not influence motility of recombinant kinesin-1.

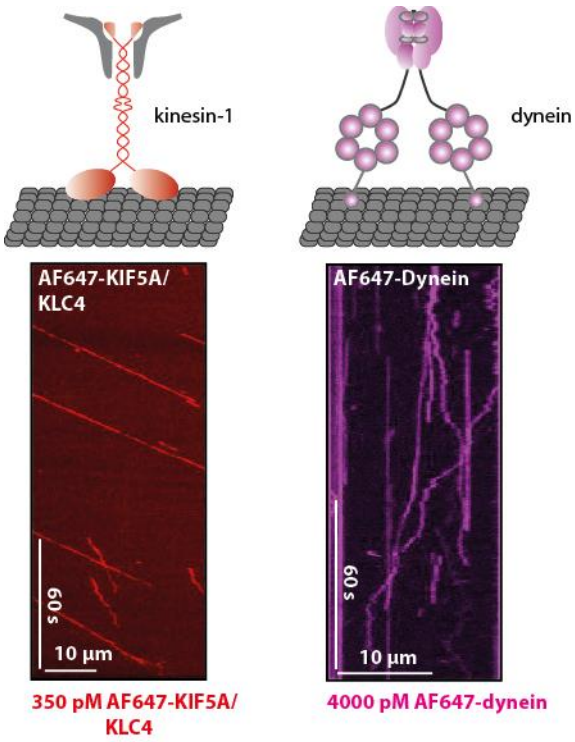

Figure 19: Kinesin-1 and dynein motility. TIRF-M in vitro reconstitution experiments were performed to test whether kinesin-1 and dynein bind to microtubules and are processive. Kymographs show that kinesin-1 (left) is processive, while dynein (right) is diffusing on microtubules. The applied concentrations are indicated below the kymographs.

We further measured the velocity and run length of the purified AF647-KIF5A/KLC4 heterotetramer in these initial exploratory experiments. Kinesin-1 was processively

moving along microtubules with a mean speed of ~1400 nm/s and a median run length of ~7.5 µm.

Of note, the kymographs of both microtubule motor proteins (Figure 19) display processive and diffusive events with similar fluorescence intensities, suggesting a homogeneity of the oligomeric states of the microtubule-bound motor protein complexes.

4.1.5. Purification of NXF1

Having established that kinesin-1 and dynein can bind to microtubules and that they move either in a processive or diffuse manner along them, we next cloned, expressed and purified NXF1. NXF1 was fused to an N-terminal solubility tag (the IgG-binding domain of protein A, ZZ domain) (Inouye and Sahara 2008) separated by a PreScission protease (3C) cleavage site. At its C-terminus, NXF1 was fused to a TEV protease cleavage site, a linker sequence (HL), a SNAP-tag, a 3C- and a His-tag (ZZ-3C-NXF1-TEV-HL-SNAP-3C-His). This construct was initially purified via affinity chromatography, and then split into two samples for the purification of (1) NXF1 and (2) NXF1-SNAP.

(1) For the purification of NXF1, PreScission (3C) as well as TEV proteases were used to cleave the N-terminal ZZ- as well as the C-terminal HL-SNAP-His fusion tag. NXF1 was then concentrated, ultracentrifuged to remove potential aggregates, and subjected to size exclusion chromatography.

(2) For the purification of NXF1-SNAP, only PreScission protease (3C) was used to cleave the N-terminal ZZ-tag. NXF1-SNAP was then concentrated and ultracentrifuged to remove potential aggregates. It was subjected to size exclusion chromatography, and its SNAP-tag was labeled with tetramethylrhodamin (TMR) dye.

A schematic overview of the NXF1(-SNAP) purification is provided in Figure 20, and the size exclusion chromatograms of the individual NXF1 and NXF1-SNAP purifications can be found in Supplementary Figure 3. Of note, as reported previously (Golovanov et al. 2004), NXF1 is characterized by poor solubility and further precipitates over time. This issue had previously been solved by adding 50 mM arginine and 50 mM glutamate to the purification buffer (Golovanov et al. 2004), however, the addition of these amino acids had an opposite effect on the solubility of NXF1 in our hands. We thus excluded them in the final purification buffers. Additionally, the TMR dye used for the labeling of NXF1-SNAP further decreased

solubility in our hands. In contrast to the purification of kinesin-1, we therefore decided to label NXF1-SNAP subsequent to size exclusion chromatography. Delaying the labeling step increased the yield of purified NXF1 by a factor of 5. Finally, we note that it is important to perform the purification with a low amount of starting material (~3-5 g of E. coli), as higher concentrations of NXF1 led to a higher propensity to precipitate, resulting in an overall lower yield.

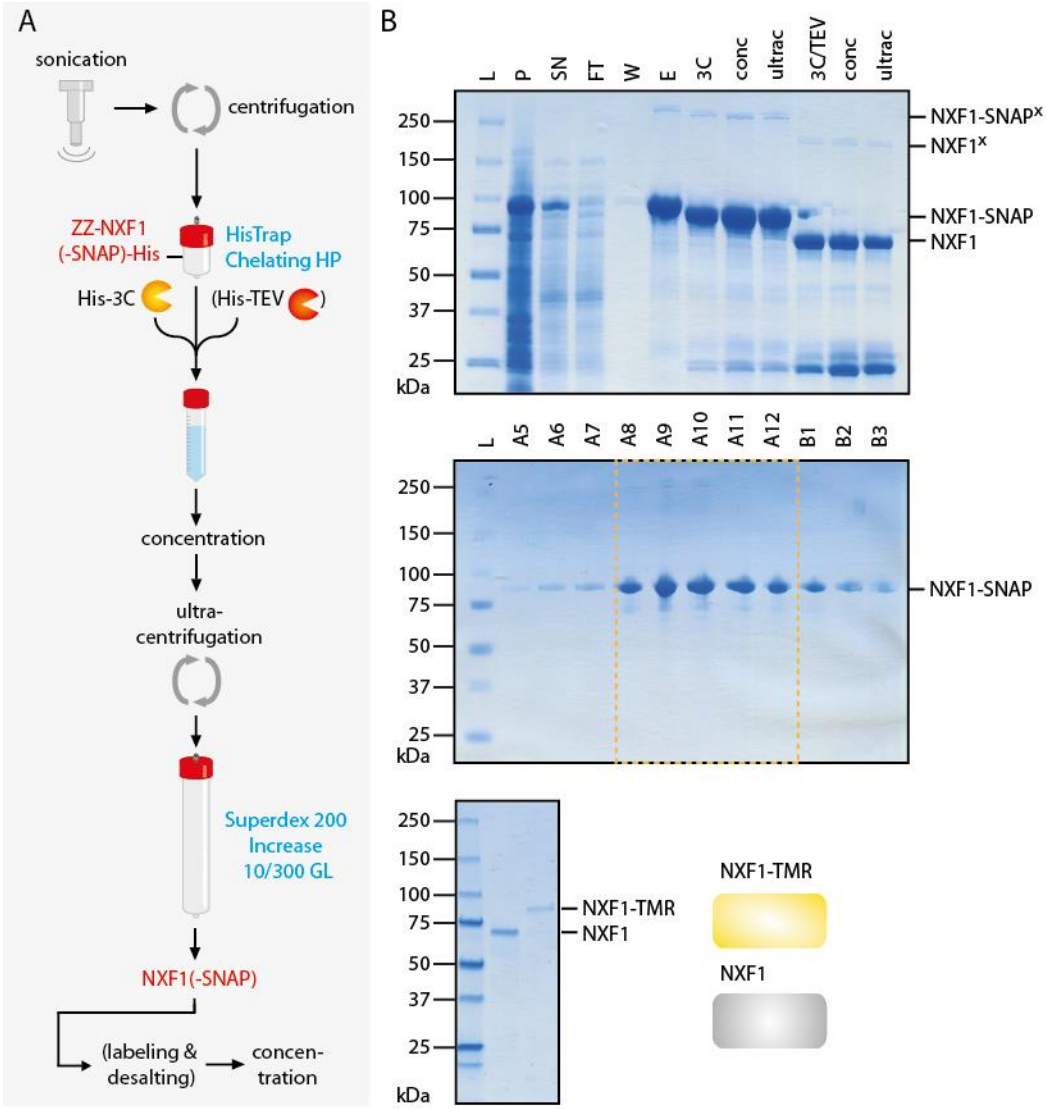

Figure 20: Purification of NXF1(-SNAP). NXF1 and NXF1-SNAP were purified according to the protocol shown in **(A)**. **(B)** Coomassie-stained SDS-PAGE gels show the purification of NXF1 and NXF1-SNAP according to (A). The upper gel shows the first steps in the purification of NXF1 and NXF1-SNAP, including 3C- and TEV protease-mediated cleavage of ZZ-NXF1(-SNAP)-His. The middle gel exemplifies the elution of NXF1-SNAP in different fractions during size exclusion chromatography. The bottom gel shows purified NXF1 and NXF1-SNAP. L: molecular weight protein

ladder, P: pellet, SN: supernatant, FT: flow-through, W: wash, 3C: PreScission protease (3C) cleavage, conc: concentration, ultrac: ultracentrifugation, 3C/TEV: 3C and TEV cleavage, A5-B3: fractions in size exclusion chromatography.

SDS-PAGE analysis (Figure 20B) confirms the purity of NXF1 and NXF1-TMR which both run as single bands at their expected molecular weights of 71.0 kDa and 93.1 kDa, respectively. The oligomerization states of NXF1 and NXF1-TMR were further analyzed using mass photometry (Supplementary Figure 6). As NXF1 is reported to homodimerize (Matzat, Berberoglu, and Lévesque 2008), we expected it to be dimeric. Our mass photometry results show that more than half of the purified NXF1 is dimeric, with a smaller peak corresponding to the mass of the NXF1 monomer. The ability of NXF1 to oligomerize is further confirmed by SDS-PAGE analysis (Figure 20), where oligomers that do not dissociate in reducing conditions and the presence of detergent can be observed at higher concentrations.

4.1.6. NXF1 interacts with motor proteins kinesin-1 and dynein

Having purified NXF1 and NXF1-TMR, we next set out to test whether NXF1 interacts with kinesin-1 and dynein in TIRF-M-coupled in vitro reconstitution experiments. Considering that microtubule-bound kinesin-1 is active in our experiments, we expected NXF1 to be transported by kinesin-1. In contrast, as dynein shows diffusive behavior, we expected NXF1 to co-diffuse with dynein.

In initial TIRF-M experiments, both kinesin-1 and dynein occasionally interacted with NXF1: NXF1 was transported by kinesin-1 (Figure 21A) and co-diffused along microtubules in a complex with dynein (Figure 21B). However, in these initial exploratory experiments, the propensity of each microtubule motor protein to interact with NXF1 was low.

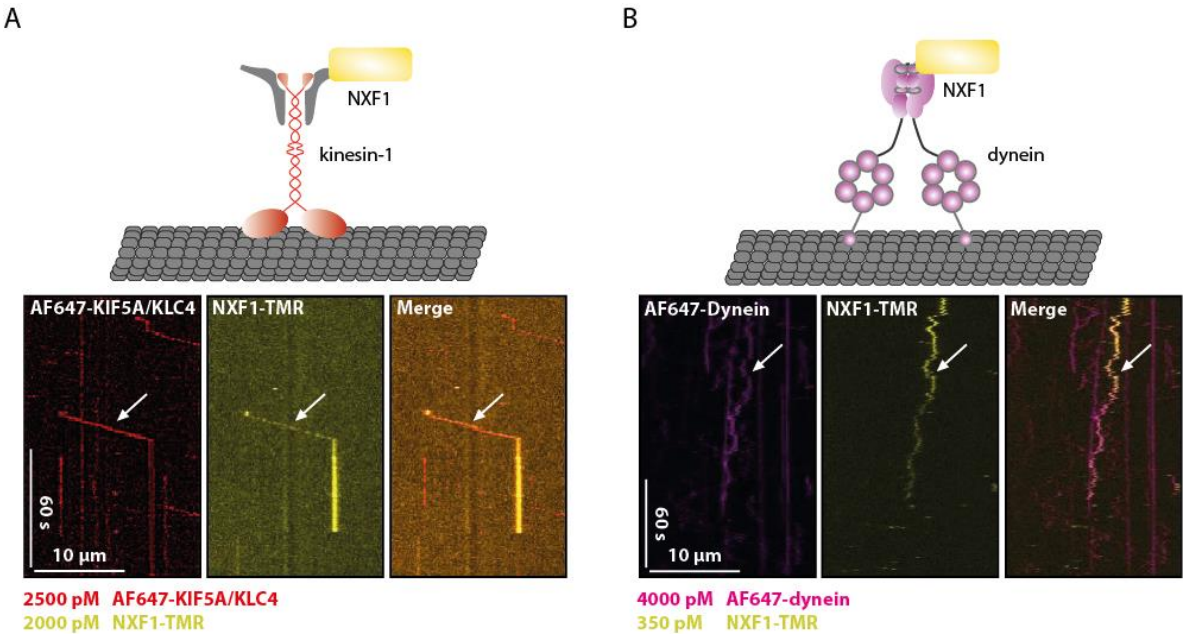

Figure 21: NXF1 occasionally interacts with microtubule motor proteins. Kymographs show that **(A)** kinesin-1 occasionally transports NXF1 and that **(B)** NXF1 occasionally co-diffuses with dynein. Arrows indicate an overlap between the AF647-KIF5A/KLC4 or AF647-dynein signals with the NXF1-TMR signal. The individual and merged channels of NXF1-TMR as well as AF647-KIF5A/KLC4 and AF647-dynein, respectively, are shown. The applied concentrations are indicated below the kymographs.

4.2. Discussion

The aim of the work presented in this chapter was to purify the individual components of the selected rec-YnH network, including microtubule motor proteins and NXF1, as well as to perform a first characterization of their functionalities and interactions.

4.2.1. Initial characterization of kinesin-1 and dynein

The first step in analyzing the novel rec-YnH interactions was to obtain the microtubule motor proteins dynein and kinesin-1. We therefore expressed and purified three kinesin-1 heterotetramers: unlabeled heterotetramer (KIF5A/KLC4), heavy chain-labeled heterotetramer (AF647-KIF5A/KLC4) and light chain-labeled heterotetramer (KIF5A/KLC4-AF647). The single affinity chromatography protocol we initially chose for the purification of the unlabeled and heavy chain-labeled heterotetramer, respectively, resulted in a higher yield of (AF647-)KIF5A HC compared to KLC4. We thus adapted the purification protocol of light chain-labeled KIF5A/KLC4-AF647 to contain a sequential affinity chromatography step (Figure

18A-B) with distinct affinity tags on the kinesin-1 light and heavy chain, respectively. Nevertheless, the excess of KIF5A HC over KLC4 could not be reduced, comparable to the other two heterotetramer preparations (Figure 18C).

A similar lower yield of kinesin-1 light vs. heavy chain can also been observed in SDS-PAGE analyses of kinesin-1 heterotetramer (KIF5A/KLC1) purifications in recent studies (Chiba et al. 2022; Tan et al. 2023). The inability to reduce the excessive amount of KIF5A HC in comparison to KLC4 possibly results from an oligomerization of the kinesin-1 heavy chain. Accordingly, KIF5A HC homotetramers and individual counts of higher order oligomers can be observed in our mass photometric analyses (Supplementary Figure 5) of the three different kinesin-1 heterotetramer preparations. This is in agreement with a recent study by the McKenney group, in which purified KIF5A HC had a 20% higher mass than the calculated mass for a KIF5A HC dimer, and KIF5A had a higher propensity to form HC oligomers in vitro than KIF5B and KIF5C isoforms (Chiba et al. 2022).

Furthermore, SDS-PAGE analyses show that KIF5A HC migrated as two bands (Figure 18C) although their amino acid sequences were found to be identical by mass spectrometric analyses. The double band has been observed previously for KIF5A, KIF5B and KIF5C HC isoforms (Chiba et al. 2022), and has been attributed to either higher oligomeric states that do not dissociate under reducing conditions and in the presence of detergent or a distinct posttranslational modification of KIF5A HC during expression in insect cells. In their recent preprint, Tan and colleagues further report two size exclusion chromatography peaks, which they suggest correspond to two different folding patterns of the KIF5B HC isoform: an extended state, corresponding to activated KIF5B HC, or a compact state, corresponding to the autoinhibited form (Tan et al. 2023). Two potential different folding states of the KIF5A HC could thus alternatively explain the presence of the double band in SDS-PAGE analyses, suggesting that only a certain fraction of KIF5A HC is active in our experiments.

Finally, the presence of a mass peak corresponding to the molecular weight of KLC4 dimers in mass photometric analyses (Supplementary Figure 5) suggests that recombinant kinesin-1 preparations might differ from in vivo complexes, as dimerization of KLCs has not been reported previously. A dimerization of KLCs could also explain why heterotrimers consisting of two KIF5A HCs and one KLC4 are not detected in our mass photometric analyses (Supplementary Figure 5).

In conclusion, the purification of kinesin-1 heterotetramers consisting of two copies of KIF5A HC and two copies of KLC4 was successful, even if accompanied by some

uncomplexed KIF5A HC oligomers and KLC4 dimers. Considering that kinesin-1 light chains do not bind to microtubules in the absence of KIF5A HCs, the presence of KLC4 dimers will not affect the analysis of kinesin-1 motility and NXF1 transport. It might be important for adjusting the concentration of NXF1 in in vitro reconstitution assays though, as uncomplexed KLC4 might bind to NXF1 in solution, depleting it from the pool that can bind to microtubule-bound KIF5A/KLC4 heterotetramers. Nevertheless, after an initial analysis of AF647-KIF5A/KLC4 heterotetramer (or AF647-KIF5A HC oligomer) motility, the light chain-labeled KIF5A/KLC4-AF647 heterotetramer can then be used to determine the percentage of (co-)transported NXF1, NXF1/SRSF3 or NXF1/SRSF3/RNA complexes, respectively, as these are expected to exclusively bind to light chain-containing KIF5A/KLC4 heterotetramers and not to KIF5A HC dimers/oligomers (see section 1.8).

4.2.2. Differential activity and processivity of kinesin-1 and dynein

To test the functionality of kinesin-1 and dynein, their activities were examined in TIRF-M-coupled in vitro reconstitution experiments. Considering that we used full-length recombinant KIF5A HC (and not constitutively active tail-truncated versions such as K560 (Chiba et al. 2022; Ferro et al. 2022; Hooikaas et al. 2019) or K460 (Chiba et al. 2022; Shimizu et al. 2000)) in combination with KLC4, we expected kinesin-1 to be autoinhibited (Coy et al. 1999; Dietrich et al. 2008; Friedman and Vale 1999; Kaan, Hackney, and Kozielski 2011; Stock et al. 1999). Contrary to our expectations, the microtubule-bound KIF5A/KLC4 heterotetramer is processive in our in vitro reconstitution experiments.

A similar processivity phenotype was recently described by the McKenney group (Chiba et al. 2022) for KIF5A HC homodimers and KIF5A/KLC1 heterotetramers, and could potentially be explained by the extended (activated) vs. compact (autoinhibited) folding states that Tan et al. described for the KIF5B heavy chain in their recent preprint (Tan et al. 2023). In gliding assays performed by the McKenney group, in which KIF5A HC dimers and KIF5A/KLC1 heterotetramers are non-specifically attached to a glass surface, both kinesin-1 preparations were able to slide microtubules along the glass surface, confirming that recombinant KIF5A is an active motor (Chiba et al. 2022). Furthermore, in single-molecule assays similar to our TIRF-M-based reconstitution assay, they were able to show that recombinant KIF5A HC dimers and KIF5A/KLC1 heterotetramers have a high processivity: Out of all MT-bound complexes, 70% of KIF5A HC dimers and 41% of KIF5A/KLC1 heterotetramers were processive, while the remaining dimers and heterotetramers were either static or diffusive. Yet, landing rates were reduced by >100-fold and further 7-fold, respectively, compared to the constitutively active, truncated K460

kinesin-1 variant (Chiba et al. 2022). Hence, kinesin-1 autoinhibition appears to primarily inhibit microtubule binding. Once bound to microtubules, a big fraction of these motors is active, aligning with the processivity phenotype observed for our kinesin-1 preparations.

In contrast to kinesin-1, dynein is diffusive in our in vitro reconstitution experiments. This observation is in agreement with the literature, in which dynein is reported to be autoinhibited in the absence of its accessory protein complex dynactin and an adaptor protein such as Bicaudal D2 (McKenney et al. 2014b; Schlager, Serra-Marques, et al. 2014). In contrast to kinesin-1, the autoinhibition does not affect microtubule binding in our experiments, but rather the ability of dynein to processively walk along microtubules.

While the mean velocity of ~1400 nm/s of the here purified recombinant KIF5A/KLC4 heterotetramers is similar to the reported range (1182 ± 187 nm/s for KIF5A HC dimers and 1051 ± 176 nm/s for KIF5A/KLC1 heterodimers (Chiba et al. 2022), the median run length of ~7.5 µm (Figure 19) we measured in our first test experiments was significantly higher than the average run length of ~1 µm determined in previous studies for tail-truncated or full-length kinesin homodimers or KIF5A/KLC1 heterotetramers, respectively (Chiba et al. 2022; Seitz and Surrey 2006; Thorn, Ubersax, and Vale 2000; Verbrugge, Van Den Wildenberg, and Peterman 2009). Considering that mass photometric analyses (Supplementary Figure 5) detected the presence of higher order oligomers such as KIF5A HC tetramers, it is possible that these long run events are caused by oligomers, as also suggested in a recent study (Chiba et al. 2022). In any case, the higher run length of the KIF5A/KLC4 heterotetramer complexes matches the run length the Maurer group has previously observed for KIF5A HC in the absence of KLCs (S. J. Baumann et al. 2022), and might depend on experimental conditions.

4.2.3. Kinesin-1 and dynein occasionally interact with NXF1

To be able to analyze the rec-YnH-based interaction between kinesin-1/dynein and NXF1, we purified NXF1. In solution, the majority of purified recombinant NXF1 is dimeric, whereas about ~33% of NXF1 is monomeric (Supplementary Figure 6). Although NXF1 is mostly characterized as a heterodimer with its adaptor NXT1, recombinant NXF1 has also been described to homodimerize in the absence of mRNA (Matzat, Berberoglu, and Lévesque 2008), aligning with the observed NXF1 dimerization in our experiments.

In initial qualitative TIRF-M-coupled in vitro reconstitution experiments, we could show that NXF1 occasionally interacted with kinesin-1 and dynein (Figure 21). A previous study had already suggested a role of kinesin-1 and dynein in the microtubule-dependent bidirectional movement of NXF1/viral RNA complexes to and around the microtubule-organizing center (Pocock et al. 2016). We here further extend this observation by identifying that the link between NXF1 and microtubule motor proteins is a direct interaction, even though happening only occasionally in initial exploratory experiments.

In cells, NXF1 itself is predicted to be autoinhibited (Viphakone et al. 2012) in the absence of SRSF3, a state in which it cannot bind mRNA. The autoinhibition comprises an intramolecular interaction between the N-terminal RRM and the C-terminal NTF2L domain of NXF1 (Müller-McNicoll et al. 2016; Viphakone et al. 2012). The only accessible NXF1 domain for interaction with microtubule motor proteins would thus theoretically be the ubiquitin-associated domain. Considering that we detected kinesin-1 and dynein light chain binding motifs mostly outside of the ubiquitin-associated domain, the NXF1 domains that are “hidden” during autoinhibition possibly remain accessible for interaction with motor proteins. Alternatively, the few NXF1 proteins in these exploratory experiments that interact with microtubule motor proteins might not be autoinhibited, similar to the equilibrium of autoinhibited vs. processive kinesin-1 dimers and heterotetramers reported previously (Chiba et al. 2022; Tan et al. 2023).

In conclusion, we have here shown the first evidence of a direct interaction between two major microtubule motor proteins dynein/kinesin-1 and the major nuclear export factor of mRNAs, NXF1, even if the interaction was observed only occasionally in these exploratory experiments.

In the following sections, we will analyze whether kinesin-1 is capable of transporting complexes of NXF1, its cofactor SRSF3 as well as RNA along microtubules with the help of TIRF-M-coupled in vitro reconstitution approaches.

5. NXF1 & SRSF3 CAN BE CO-TRANSPORTED BY KINESIN-1

5.1. Results

Having shown that kinesin-1 and dynein interact with NXF1 (even if only occasionally in initial, exploratory experiments), we next set out to determine whether SRSF3 interacts with motor protein-bound NXF1, resulting in either co-transport or co-diffusion via kinesin-1 and dynein, respectively.

Since full-length SRSF3 had not been expressed in a soluble manner in E. coli previously due to its intrinsic insolubility (Hargous et al. 2006; Yingqun Huang et al. 2003), our first aim was to identify an expression condition that yielded soluble SRSF3 and SNAP-tagged SRSF3, respectively.

5.1.1. Finding suitable expression conditions for (SNAP-)SRSF3

In accordance with previous groups (Hargous et al. 2006; Yingqun Huang et al. 2003), we also chose to express (SNAP-)SRSF3 in E. coli, as expression in this host offers various advantages over the expression in other cell types such as insect or human cells. Expression in E. coli does not only typically yield a high amount of the protein of interest, it is also simple, cost-effective and rapid. Furthermore, there are multiple E. coli strains to choose from, for example, the BL21-CodonPlus(DE3)-RIL and Rosetta™ (DE3)pLysS strains that additionally code for tRNAs that are rare in E. coli, namely arginine, isoleucine, leucine, proline and glycine. The Rosetta™ (DE3)pLysS strain further expresses T7 lysozyme which is used to prevent the leaky expression of proteins prior to the induction of protein expression.

The combination of these advantages enabled us to compare several different parameters for the expression of (SNAP-)SRSF3 in E. coli:

(1) Different N-terminal solubility tags: Maltose-binding protein (MBP) and N-utilization substance protein A (NusA) (Raran-Kurussi and Waugh 2014);

(2) Different E. coli strains: BL21-CodonPlus(DE3)-RIL and Rosetta™ (DE3)pLysS;

(3) Different expression conditions: (a) 18 °C, 16 h, 0.1 mM IPTG; (b) 25°C, 5 h, 0.5 mM IPTG; (c) 37°C, 3 h, 1 mM IPTG.

At its N-terminus, (SNAP-)SRSF3 was fused to either of the indicated solubility tags and a SUMO3 cleavage site (Besir 2017). At its C-terminus, it was fused to a 3C protease cleavage site as well as a Strep-tag. The resulting constructs (NusA-SUMO3-(SNAP-)SRSF3-3C-Strep and MBP-SUMO3-(SNAP)-SRSF3-3C-Strep) were used for expression in small volumes according to the indicated conditions, and the solubility of the proteins was tested by ultracentrifugation of the cell lysate after expression.

By comparing the intensity of (SNAP-)SRSF3 bands on SDS-PAGE gels, we were ultimately able to determine the condition that yielded the highest amount of soluble (SNAP-)SRSF3 (Figure 22A, here exemplified for non-SNAP-tagged SRSF3). It included the following parameters: Expression at 18°C for 16 h with an IPTG concentration of 0.1 mM using the Rosetta™ (DE3)pLysS E. coli strain and the NusA solubility tag. The lower temperature and therefore longer expression time represent a “soft” way of expressing proteins, which ultimately facilitates the expression of soluble protein. In contrast, the shorter expression time at 37°C increases the chance of obtaining unfolded or misfolded protein (Francis and Page 2010).

To test for leaky expression of NusA-SUMO3-(SNAP-)SRSF3-3C-Strep prior to the induction of protein expression in the determined condition, we further performed a Western Blot analysis with an anti-Strep antibody (Figure 22B, here exemplified for non-SNAP-tagged SRSF3). As expected, considering the presence of T7 lysozyme in the Rosetta™ (DE3)pLysS E. coli strain, leaky expression of SRSF3 was not detectable. Furthermore, Western blot analysis clearly shows that the majority of SRSF3 expressed under the chosen condition was soluble.

In conclusion, we were thus not only successful in identifying an expression condition resulting in soluble (SNAP-)SRSF3, but also an expression condition in which the majority of expressed (SNAP-)SRSF3 is soluble.

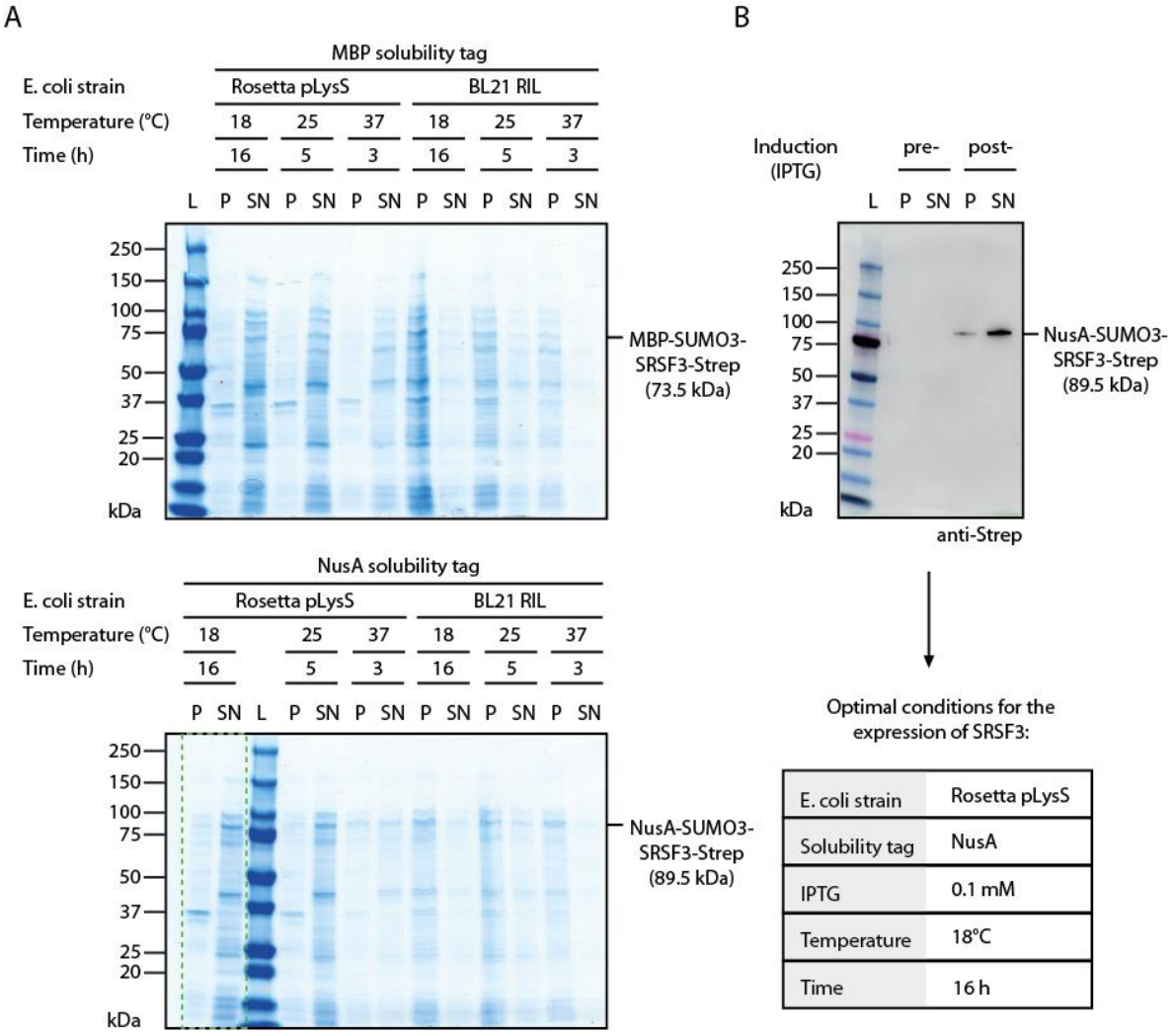

Figure 22: Finding optimal conditions for the expression of (SNAP-)SRSF3. (A) Coomassie-stained SDS-PAGE gels exemplify expression tests for SRSF3 fused to the N-terminal solubility tags MBP (top gel) and NusA (bottom gel). Varying expression conditions were tested: different E. coli strains (Rosetta™ (DE3)pLysS and BL21-CodonPlus(DE3)-RIL), different temperatures (18°C, 25°C, 37°C), different IPTG concentrations (according to temperature; 18°C: 0.1 mM IPTG, 25°C: 0.5 mM IPTG, 37°C: 1 mM IPTG) and different expression times (16 h, 5 h, 3 h). For each condition, the soluble fraction (supernatant, SN) was separated from the insoluble fraction (pellet, P). The condition that yielded the highest amount of soluble SRSF3 (Rosetta™ (DE3)pLysS, NusA, 0.1 mM IPTG, 18°C, 16 h expression) is marked with a green, dashed rectangle. **(B)** The marked condition in (A) was further validated via Western Blot analysis using an anti-Strep antibody for the detection of soluble NusA-SUMO3-SRSF3-3C-Strep prior to and after the induction of protein expression.

5.1.2. Purification of (SNAP-)SRSF3

Following the successful expression of soluble SRSF3 and SNAP-tagged SRSF3, respectively, our aim was to purify both of the latter. We initially focused on the

purification of non-SNAP-tagged SRSF3 to determine optimal purification conditions, and then used the same conditions for the purification of SNAP-SRSF3.

Owing to its described intrinsic insolubility (Hargous et al. 2006), we expected the purification of SRSF3 to be technically challenging following its extraction from E. coli. Initial attempts included purification at 4°C, which is typically used for the purification of recombinant proteins to reduce proteolysis (Remans et al. 2022), as well as size exclusion chromatography to remove any contaminants during purification. However, SRSF3 appeared to be less stable at lower temperatures (data not shown). Furthermore, contaminants could not be efficiently removed and the overall protein yield was severely reduced upon size exclusion chromatography (data not shown), potentially resulting from an interaction of SRSF3 with the column resin.

We were ultimately able to design a room temperature-based purification protocol that yielded pure SRSF3 and SNAP-SRSF3, respectively. The protocol, which is schematically shown in Figure 23, will be briefly discussed here to highlight crucial purification steps. With the aim of degrading contaminating nucleic acids, NusA-SUMO3-(SNAP-)SRSF3-3C-Strep is extracted from E. coli via a prolonged sonication step. Following sonication, it is purified via affinity chromatography and separated from its solubility (NusA-) and purification (Strep-) tags via on-column protease cleavage. SNAP-SRSF3 is subsequently fluorescently labeled with AF647 dye, and non-incorporated dye is subsequently removed via a desalting column. AF647-SRSF3 as well as SRSF3 are finally ultracentrifuged. This step, used to remove potential aggregates, is performed using a lower velocity compared to other purification protocols in this thesis, as SRSF3 is otherwise pelleted.

SDS-PAGE analysis confirms the successful purification of both proteins using the purification protocol developed: SRSF3 and SNAP-SRSF3 migrated as single bands at their expected molecular weights of 19.3 kDa and 41.3 kDa, respectively (Figure 23B). Of note, we initially tried to purify C-terminally instead of N-terminally SNAP-tagged SRSF3. Several purification attempts showed, however, that SRSF3-SNAP was not stable, as the SNAP-tag was typically lost during purification (data not shown), potentially by degradation. Placement of the SNAP-tag at the N-terminus of SRSF3, however, solved this problem.

To further determine the oligomeric state of purified SRSF3 and SNAP-SRSF3, mass photometric analyses were performed (Supplementary Figure 7). Both SRSF3 (19.3 kDa) and SNAP-SRSF3 (41.3 kDa) are either below or at the border of the lower molecular mass detection limit of 40 kDa for this technique (Sonn-Segev et al.

2020; D. Wu and Piszczek 2020, 2021). Their monomer peaks are thus overlayed with the buffer background signal peak (Supplementary Figure 7), and their mass peaks hence cannot be assigned to their molecular mass. Nevertheless, the mass photometric analyses confirm that there are no higher order aggregates of neither of the two purified proteins.

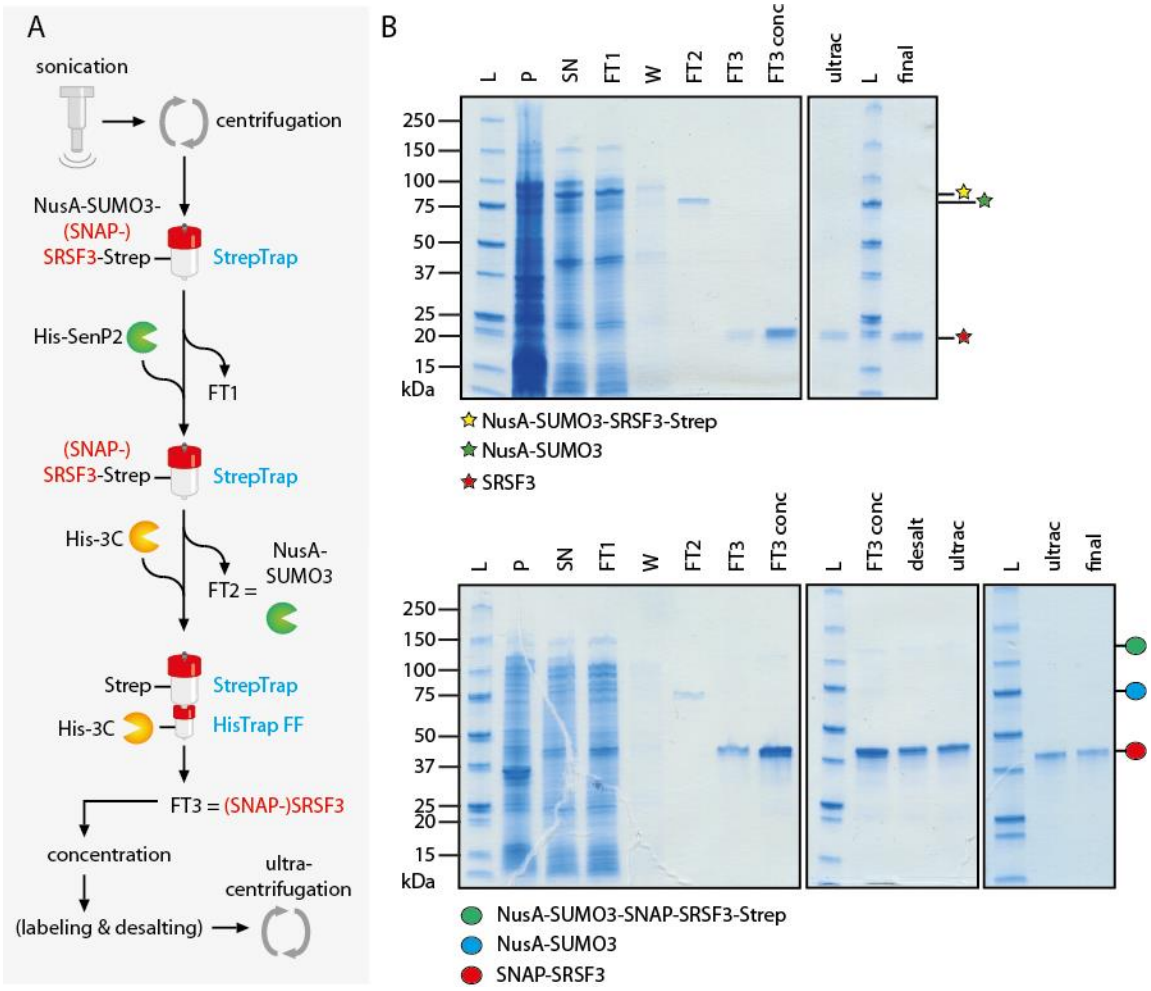

Figure 23: Purification of (SNAP-)SRSF3. SRSF3 and SNAP-SRSF3 were purified according to the protocol shown in **(A)**. **(B)** Coomassie-stained SDS-PAGE gels show the purification steps according to (A) for SRSF3 (top) and SNAP-SRSF3 (bottom). SNAP-SRSF3 was fluorescently labeled with AF647, and non-incorporated dye was removed via to remove non-incorporated fluorescent dye. L: molecular weight protein ladder, P: pellet, SN: supernatant, FT1: flow-through 1, W: wash, FT2: flow-through 2, FT3: flow-through 3, desalt: removal of non-incorporated AF647 dye, conc: concentration, ultrac: ultracentrifugation, final: final sample after flash-freezing and thawing.

5.1.3. SRSF3 occasionally interacts with motor protein-bound NXF1

We next aimed to determine whether SRSF3 and NXF1 can simultaneously interact with microtubule motor proteins. In the case of an interaction, we expected SRSF3 and NXF1 to be co-transported by kinesin-1 or to co-diffuse along microtubules in a complex with dynein. To reduce the complexity of the performed assays, we opted to focus on analyzing exclusively kinesin-1-based transport from now on.

To observe simultaneously fluorescently labeled NXF1 and SRSF3 in kinesin-1-based transport experiments, the unlabeled kinesin-1 heterotetramer (KIF5A/KLC4) was used. Besides individual transport events of NXF1 and SRSF3, we could identify co-transport events of both proteins. This is exemplified in the kymograph in Figure 24, in which out of four NXF1 transport events on a single microtubule, three are accompanied by SRSF3. Even though these initial results suggest that NXF1 and SRSF3 can indeed be co-transported via kinesin-1, the total number of co-transport events of both proteins strongly varied, and were overall low in these initial, exploratory experiments.

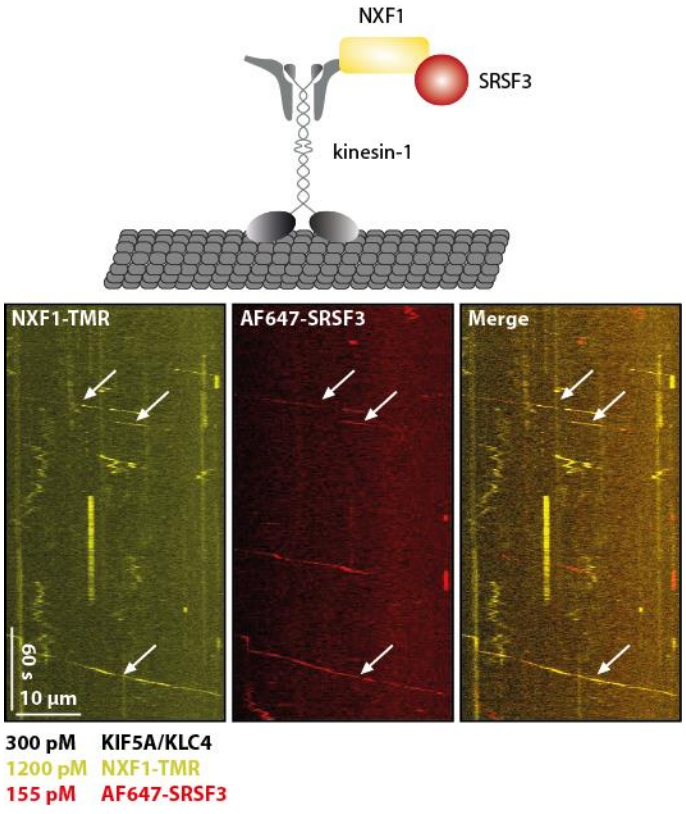

Figure 24: NXF1 and SRSF3 are occasionally co-transported by kinesin-1. Kymographs show that NXF1-TMR and AF647-SRSF3 are co-transported by kinesin-1. Arrows indicate overlaps of the

NXF1-TMR and AF647-SRSF3 signals. The individual and merged channels of NXF1-TMR and AF647-SRSF3 are shown, and the applied concentrations are indicated below the kymographs.

In an attempt to increase the co-transport events of NXF1 and SRSF3 by kinesin-1, we changed two parameters in the in vitro reconstitution experiments, including (1) the addition of ATP to the pre assay mix and (2) the addition of mRNA to the final assay mix. In the pre assay mix (Figure 16, step 1), kinesin-1 (as well as NXF1 and SRSF3) was not incubated with ATP. We expected that addition of ATP to the pre assay mix and not just to the final assay mix (Figure 16, step 6) might stabilize kinesin-1, resulting in a higher quantity of active kinesin-1 molecules and therefore potentially also higher NXF1/SRSF3 co-transport numbers. Addition of ATP to the pre assay mix, however, reduced transport numbers of NXF1/SRSF3, potentially resulting from an interaction of its negatively charged phosphates with the highly positively charged RS domain of SRSF3. Furthermore, although NXF1 and SRSF3 were co-transported in the absence of RNA in these initial experiments, we hypothesized that the number of co-transport events might be increased in the presence of RNA, perhaps by further stabilizing the interaction as described previously (Müller-McNicoll et al. 2016). Initial attempts of adding full-length CamKIIα mRNA (obtained from Artem Komissarov (Maurer group)) to exploratory experiments, however, did not lead to an increase in NXF1/SRSF3 co-transport numbers.

In conclusion, we could for the first time show that kinesin-1 can co-transport two RBPs, NXF1 and its cofactor SRSF3, even though the number of co-transport events was low in these initial, exploratory experiments.

5.2. Discussion

After having established that the main interaction in the proposed rec-YnH network, comprising NXF1 and kinesin-1/dynein, can indeed be reconstituted in a single-molecule in vitro assay, the aim of the work presented in this chapter was to analyze whether kinesin-1 can co-transport NXF1 and SRSF3 in vitro.

In the literature, it is widely accepted that SRSF3 recruits NXF1 to mRNA after the completion of splicing in the nucleus (Y. Huang, Yario, and Steitz 2004; Lai and Tarn 2004). In the past, the interaction between NXF1 and SRSF3 has mostly been described as direct on the basis of pull-down and co-immunoprecipitation approaches in the presence of RNase (Hargous et al. 2006; Yingqun Huang et al. 2003; Lai and Tarn 2004; Tintaru et al. 2007). In contrast, a recent study shows that the NXF1/SRSF3 interaction is lost in co-immunoprecipitation assays upon

prolonged RNase treatment (Müller-McNicoll et al. 2016), suggesting a stabilization of the NXF1/SRSF3 interaction by mRNA in vivo. However, no study has so far been able to conclusively verify whether the interaction is based on a direct protein-protein or protein-RNA-protein interaction using an in vitro assay (see section 1.7), as recombinant, full-length SRSF3 could not be expressed in a soluble form yet (Hargous et al. 2006; Yingqun Huang et al. 2003).

In this thesis, we report, to our knowledge, the first successful purification of bacterially overexpressed, recombinant, full-length SRSF3, enabling us to further analyze the interaction between SRSF3 and NXF1. Strikingly, in our in vitro reconstitution assays, we were able to show that SRSF3 can indeed occasionally interact with kinesin-1/NXF1 complexes in the absence of RNA (Figure 24). Whenever NXF1 and SRSF3 are co-transported, the kinesin-1/NXF1/SRSF3 complex appears to be stable, as neither NXF1 nor SRSF3 dissociates from kinesin-1 during its run (Figure 25). Our results thus suggest that NXF1 and SRSF3 do not require a stabilization via RNA in order to be co-transported by kinesin-1 in vitro. This finding is in agreement with previous studies performed in cell lysate, reporting a direct interaction between NXF1 and SRSF3 in the presence of RNase (Hargous et al. 2006; Yingqun Huang et al. 2003; Lai and Tarn 2004; Tintaru et al. 2007), assuming that NXF1 and SRSF3 interact with each other while being transported by kinesin-1.

Although we were not able to obtain high numbers of NXF1/SRSF3 co-transport events in these initial reconstitution experiments, our results not only represent a novel reconstitution of kinesin-1-mediated transport of an RNA-binding protein, adding to the very small number of previous such reconstitutions, but we also report, to our knowledge, the first reconstitution of a kinesin-1-based transport system comprising *two* RNA-binding proteins in combination.

Our first attempts of increasing the number of NXF1/SRSF3 co-transport events in our in vitro reconstitution experiments consisted of the addition of either ATP or mRNA to the pre incubation mixes (containing kinesin-1, NXF1 and SRSF3; compare with Figure 16). As neither of these attempts resulted in higher numbers of NXF1/SRSF3 co-transport events, and co-transport was not always reproducible, we hypothesized that an additional factor may be required to increase the propensity of NXF1 and SRSF3 to form complexes with kinesin-1.

6. DO ADDITIONAL FACTORS INCREASE THE ASSOCIATION BETWEEN NXF1/SRSF3 AND KINESIN-1?

In the preceding chapters, we established that kinesin-1 can co-transport NXF1 and SRSF3. However, the number of NXF1/SRSF3 co-transport events remained low and transport was not always reproducible, suggesting that additional factors may be required to increase the propensity of NXF1 and SRSF3 to form complexes with kinesin-1. The work presented in this chapter focuses on identifying and analyzing these potential additional factors that might stabilize the kinesin-1/NXF1/SRSF3 complex.

6.1. Results

6.1.1. Extension of the core rec-YnH network

Considering that we identified NXF1 to be a hub for protein interactions, we extended the core NXF1 rec-YnH network (Supplementary Figure 8) to determine proteins that show (if possible) NanoBRET-validated interactions with both kinesin-1 light chain KLC4 and NXF1. Three additional factors fulfill this requirement (Figure 25): fasciculation and elongation zeta protein 2 (FEZ2), RNA transcription, translation and transport factor protein (RTRAF) as well as Nudix hydrolase 21 (NudT21).

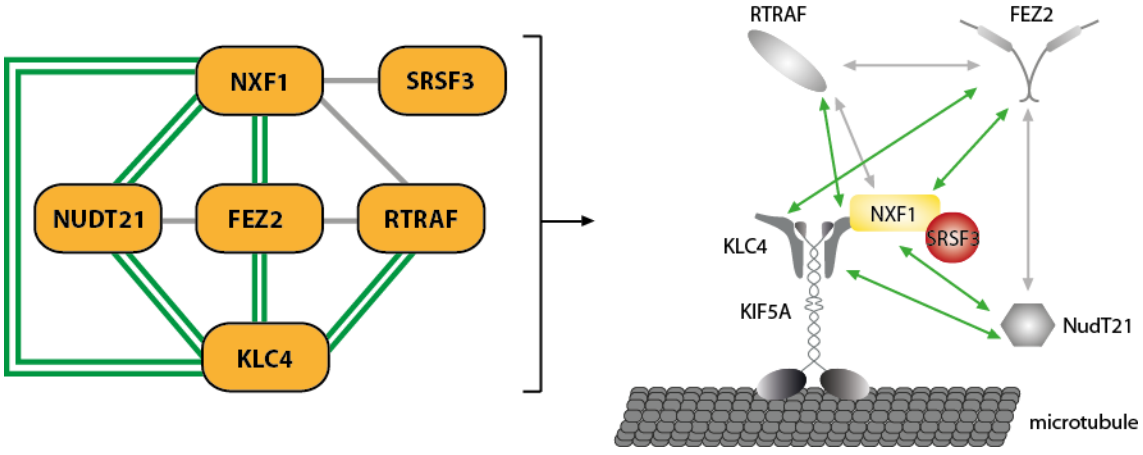

Figure 25: NXF1 and KLC4 are shown interact with additional proteins. NXF1 and KLC4 are predicted to interact with NudT21, FEZ2 and RTRAF in the rec-YnH screen. These interactions have (mostly) been validated by NanoBRET. Green: rec-YnH and NanoBRET positive; gray: rec-YnH positive, NanoBRET negative.

Besides showing interactions with both KLC4 and NXF1 in the rec-YnH and NanoBRET screens, each of these proteins is additionally reported to interact either directly or indirectly with mRNA and/or the microtubule cytoskeleton in the literature. FEZ2, RTRAF and NudT21 are thus interesting factors to study in the context of mRNA transport, and their established roles in this aspect will be outlined in the following.

FEZ1, to which its paralog FEZ2 is closely related, is described to interact with kinesins KIF3 and KIF5 (Fujita et al. 2007; Suzuki et al. 2005). It was proposed to function as a dimeric, bivalent cargo transport adaptor (Teixeira, Alborghetti, and Kobarg 2019), linking a variety of cargoes to microtubule-based transport. Since FEZ1 shares all of its binding partners with FEZ2 (Marcos R. Alborghetti, Furlan, and Kobarg 2011), this adaptor function is likely present in both paralogs, which are further described to play a role in neuronal development as well as neurological disorders (Teixeira, Alborghetti, and Kobarg 2019).

RTRAF, on the other hand, is described to be a component of kinesin-1- and mRNA-containing dendritic granules (Kanai, Dohmae, and Hirokawa 2004) as well as cytosolic, ribosome-containing RNA granules (Elvira et al. 2006).

Finally, NudT21, a component of the cleavage factor Im complex, is reported to be a “master regulator” of alternative polyadenylation (Y. Chu et al. 2019) that promotes the synthesis of longer 3’UTRs similar to SRSF3. Disruption of NudT21-mediated regulation of alternative polyadenylation is consequently reported to result in intellectual disability (Alcott et al. 2020; Gennarino et al. 2015).

In conclusion, each of the above-mentioned proteins has a potential function in neuronal mRNA transport. Consequently, they represent suitable candidates to test in combination with NXF1 and KIF5A/KLC4, potentially leading to the identification of a factor that stabilizes the kinesin-1/NXF1/SRSF3 complex in in vitro reconstitution experiments.

6.1.2. Purification of extended rec-YnH network components

To analyze the transport of NXF1/SRSF3 complexes in the presence of FEZ2, RTRAF and NudT21 in in vitro reconstitution assays, we cloned, expressed and purified each of the latter in unlabeled and labeled versions (Figure 26). FEZ2, RTRAF and NudT21 were each fused to an N-terminal solubility tag (NusA- or ZZ-tag) as well as a C-terminal affinity tag (His- or Strep-tag) which were separated via protease cleavage sites. For the purification of labeled proteins, FEZ2, RTRAF and

NudT21 were fused to an N- or C-terminal SNAP-tag. All proteins were expressed in E. coli and purified via affinity chromatography. After cleavage of solubility and affinity tags, proteins were subjected to size exclusion chromatography, and labeling was performed using AF647 dye.

In SDS-PAGE analyses, all proteins run at their expected molecular weights of 42.6 kDa (unlabeled FEZ2), 27.2 kDa (unlabeled NudT21) and 28.9 kDa (unlabeled RTRAF), respectively. Likewise, the labeled proteins run at their expected molecular weights of 71.1 kDa (labeled FEZ2), 49.2 kDa (labeled NudT21) and 54.0 kDa (labeled RTRAF), respectively. Of note, both unlabeled and labeled RTRAF are characterized by a double band that has previously been observed for the wild type protein (Pazo et al. 2019), potentially resulting from distinct posttranslational modifications.

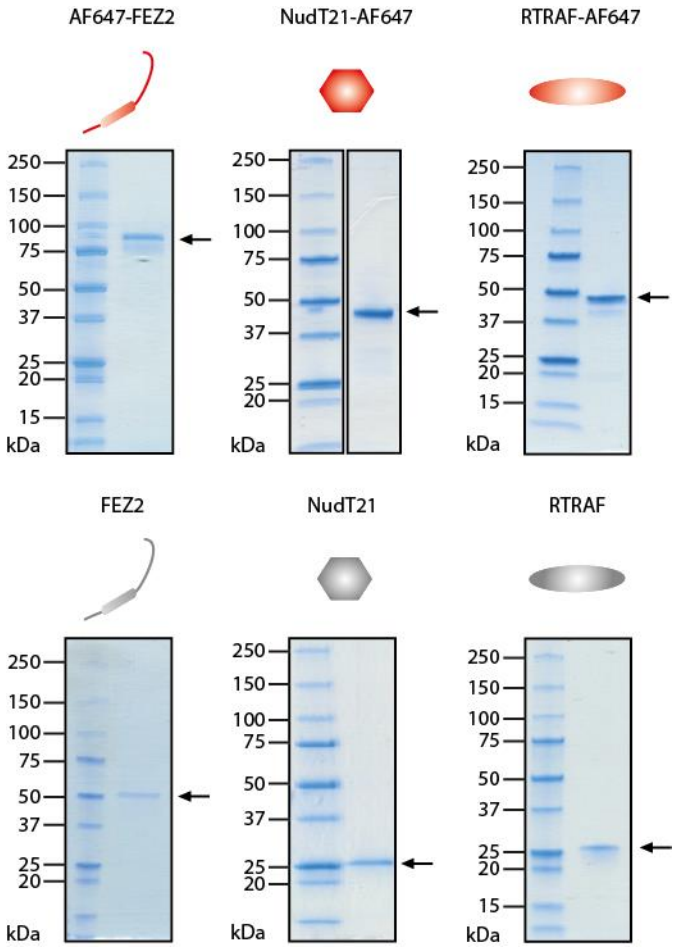

Figure 26: Purification of extended rec-YnH network components. Coomassie-stained SDS-PAGE gels show the purity of labeled and unlabeled FEZ2, RTRAF and NudT21. FEZ2-AF647, FEZ2 and RTRAF-AF647 were purified in this thesis. RTRAF was purified by Carlo Carolis (Protein

Technologies Unit, CRG), whereas NudT21-AF647 and NudT21 were purified by Silvia Speroni (Maurer group). Purification protocols are similar to that of NXF1-TMR and NXF1, respectively, as described in section 3.3.

To analyze the oligomeric states of the purified proteins, they were subjected to mass photometric analyses (Supplementary Figure 9). Considering that the molecular weights of the monomeric proteins are either below or close to the background signal of the TIRF-M assay buffer which they were measured in (corresponding to 40 kDa), the method was only suitable for the detection of oligomer formation. As only minor oligomer peaks were detected for each protein, we assume that they are predominantly present as monomers.

6.1.3. FEZ2 is co-transported with NXF1 and might increase the co-transport numbers of NXF1 and SRSF3

To determine whether the factors of the extended rec-YnH network increase complex formation between kinesin-1 and NXF1, we tested FEZ2, RTRAF and NudT21 in TIRF-M in vitro reconstitution assays (Figure 27 and Figure 28). Based on the rec-YnH and NanoBRET results (Figure 25), we expected each of the proteins to interact with both kinesin-1 and NXF1. Surprisingly, out of all analyzed proteins, we observed that only FEZ2 was transported via kinesin-1 alone as well as in combination with NXF1 (Figure 27A). Furthermore, in exploratory experiments, kinesin-1 frequently co-transported NXF1 and SRSF3 in the presence of FEZ2, as exemplified in Figure 27B.

In disagreement with the extended rec-YnH network (Figure 25), the remaining proteins (NudT21 and RTRAF) did not show an association with kinesin-1 or NXF1 in exploratory experiments (Figure 28A+C). Considering that the rec-YnH network shows an additional link between NudT21, RTRAF and FEZ2, we next assessed whether the further addition of FEZ2 to the experiment including NXF1, kinesin-1 and NudT21/RTRAF could induce complex formation and thus potentially increase NXF1/SRSF3 co-transport (Figure 28B+D).

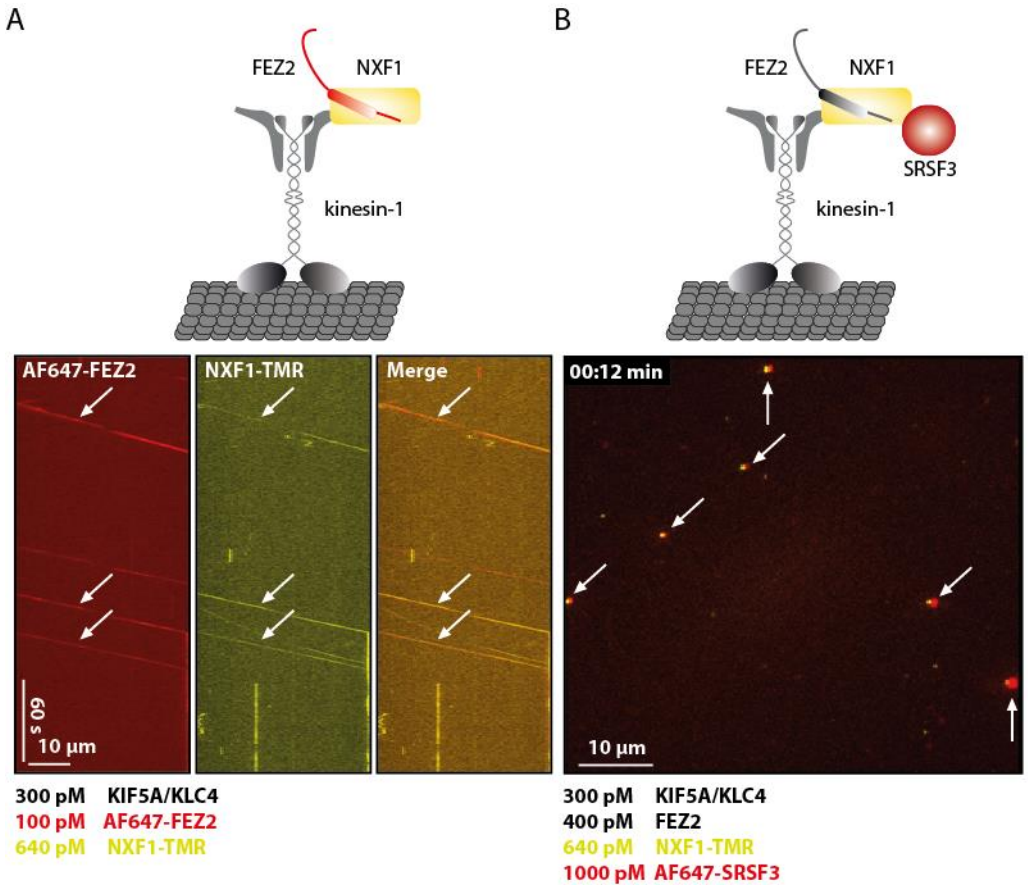

Figure 27: FEZ2 is co-transported with NXF1 and potentially increases NXF1/SRSF3 co-transport numbers. (A) Kymograph showing that NXF1 and FEZ2 are co-transported by kinesin-1 (marked by white arrows). **(B)** Entire field of view of a TIRF-M movie (at 12 s out of 5 min) showing a high association of NXF1 and SRSF3 in the presence of FEZ2.

Interestingly, the addition of FEZ2 to exploratory experiments including kinesin-1, NXF1 and RTRAF (Figure 28B) resulted in the transport of RTRAF by kinesin-1. However, the lack of NXF1 co-transport in this experiment potentially suggests that RTRAF competes with NXF1 for kinesin-1/FEZ2 binding. Alternatively, when FEZ2 was added to exploratory experiments including kinesin-1, NXF1 and NudT21 (Figure 28D), it did not promote an interaction with either kinesin-1 or NXF1, respectively.

In conclusion, out of the tested proteins, FEZ2 is the only factor that can stably associate with kinesin-1/NXF1(/SRSF3) complexes, and was thus included in the in vitro reconstitution experiments presented in the next chapters.

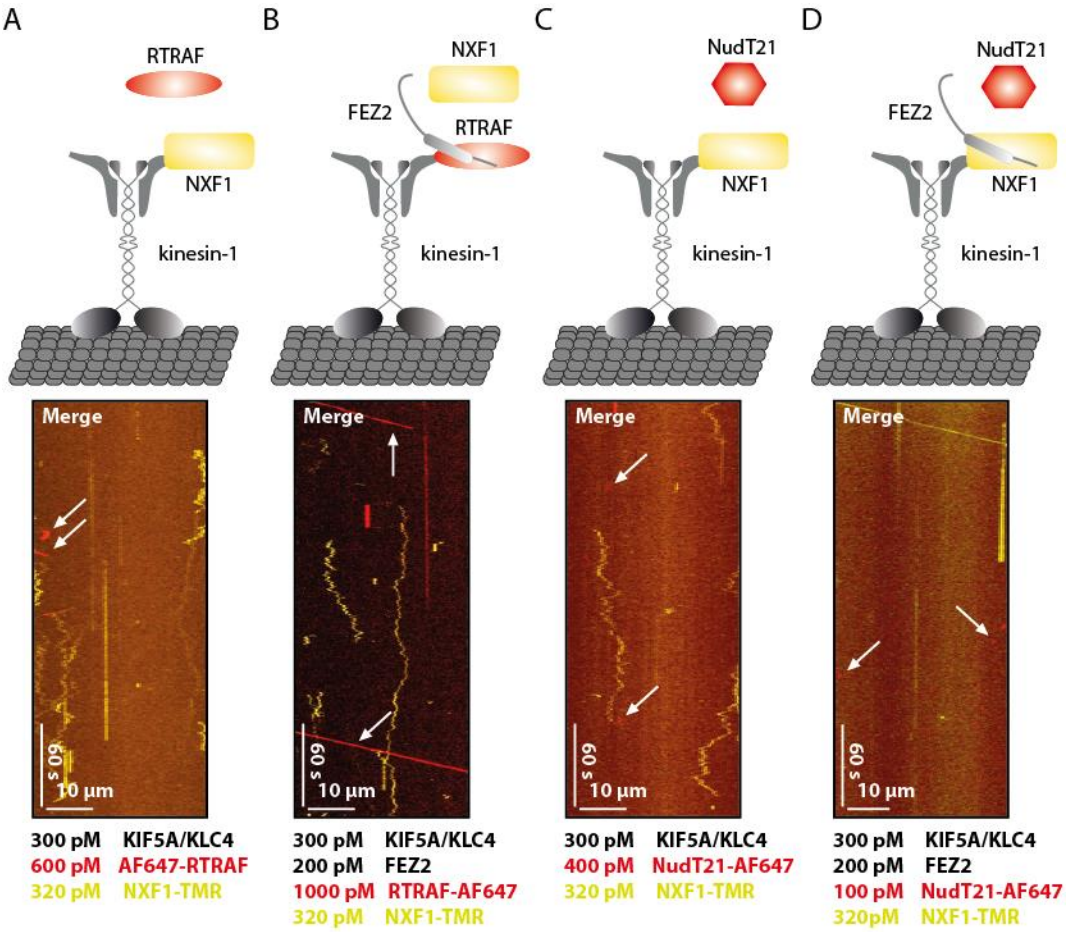

Figure 28: RTRAF and NudT21 do not increase kinesin-1-mediated NXF1 transport. Preliminary data shows that the additional selected proteins from the extended NXF1 rec-YnH network do not increase kinesin-1-mediated NXF1 transport. Different combinations of proteins were tested and exemplary kymographs were chosen. White arrows show the presence of the labeled, additional proteins (red) in the kymographs. **(A)** RTRAF does not interact with kinesin-1 or NXF1. **(B)** In the presence of FEZ2, RTRAF interacts with kinesin-1, however, NXF1 is not co-transported. **(C)** Like RTRAF, NudT21 does not interact with kinesin-1 or NXF1. **(D)** The presence of FEZ2 in the experiment does not lead to an association of NudT21 with NXF1 or kinesin-1.

6.2. Discussion

After having established that NXF1 and SRSF3 are occasionally co-transported by kinesin-1, the aim of the work presented in this chapter was to analyze whether the number of NXF1/SRSF3 co-transport events could be increased.

Starting from the extended rec-YnH-based NXF1 network (Supplementary Figure 8), we tested whether FEZ2, RTRAF and NudT21, which show interactions with both

NXF1 and KLC4 (Figure 25), can increase kinesin-1-based co-transport of NXF1 and SRSF3.

Out of the three proteins analyzed, FEZ2 showed a favorable interaction with both KLC4 and NXF1, visualized by its kinesin-1-based co-transport with NXF1 (Figure 27A). A link between FEZ2 and NXF1 had not been reported previously, and suggests that FEZ2, like its paralog FEZ1, can increase the association of cargoes with kinesin (Fujita et al. 2007; Suzuki et al. 2005; Teixeira, Alborghetti, and Kobarg 2019). Although described to homodimerize in the literature (M. R. Alborghetti et al. 2010), neither AF647-FEZ2, nor unmodified FEZ2 are dimeric in our experiments (Supplementary Figure 9), revealing that homodimerization is not a requirement for FEZ2 to increase the association of NXF1 with kinesin-1.

Exploratory experiments further revealed a frequent co-transport of NXF1 and SRSF3 in the presence of FEZ2 (Figure 27B), but no co-transport of NXF1 with RTRAF or NudT21, respectively (Figure 28B+D), was observed. This suggests a certain selectivity in the rec-YnH network. As the rec-YnH method relies on the homologous recombination of individual bait and prey protein pairs, the method cannot detect whether all of the identified interactions can take place simultaneously or whether some interactions block others via steric hindrances. Additionally, even though mostly validated using the NanoBRET approach, rec-YnH-predicted interactions may nevertheless be false positives or might depend on the cellular environment which they were detected in. Thus, the here presented in vitro reconstitutions with selected components are critical to identify minimal sets of interactors required for efficient microtubule-based transport.

In conclusion, in this chapter we determined that NXF1 and SRSF3 are frequently co-transported by kinesin-1 in the presence of FEZ2. We thus concluded that FEZ2 is an important factor to include in the in vitro reconstitution experiments presented in the next chapters.

7. NXF1 & SRSF3 ARE EFFICIENTLY CO-TRANSPORTED BY KINESIN-1 VIA INTERACTION WITH KLC4

7.1. Results

In the work presented in the previous chapter, we established in exploratory TIRF-M-coupled in vitro reconstitution experiments that the low number of kinesin-1-based NXF1/SRSF3 co-transport events is potentially increased in the presence of FEZ2 (Figure 27).

7.1.1. KLC4 is required for the transport of NXF1

Direct binding to the KIF5A HC has been reported in previous studies for other kinesin-1 cargoes (Sun et al. 2011; Williams et al. 2014; Woźniak and Allan 2006). Since minor KIF5A HC dimer/oligomer populations are also present in our heterotetramer preparations (Figure 18 and Supplementary Figure 5), we wanted to test if transport of FEZ2/NXF1/SRSF3 complexes is really dependent on the kinesin-1 light chain KLC4 (Figure 18 and Supplementary Figure 5), as predicted by the rec-YnH and NanoBRET screens (Figure 25).

To do so, we designed an in vitro reconstitution experiment in which we focused exclusively on the transport of NXF1 by each of the KIF5A/KLC4 heterotetramer preparations (KIF5A/KLC4-AF647, AF647-KIF5A/KLC4, unlabeled KIF5A/KLC4) in comparison to a dimeric AF647-KIF5A HC which was kindly provided by Sebastian Baumann (Maurer group).

In these in vitro experiments, each of the KLC4-containing heterotetramers transported NXF1. In contrast, NXF1 was not transported by AF647-KIF5A HC dimers, suggesting that KLC4 is indeed required for the transport of NXF1 (Figure 29).

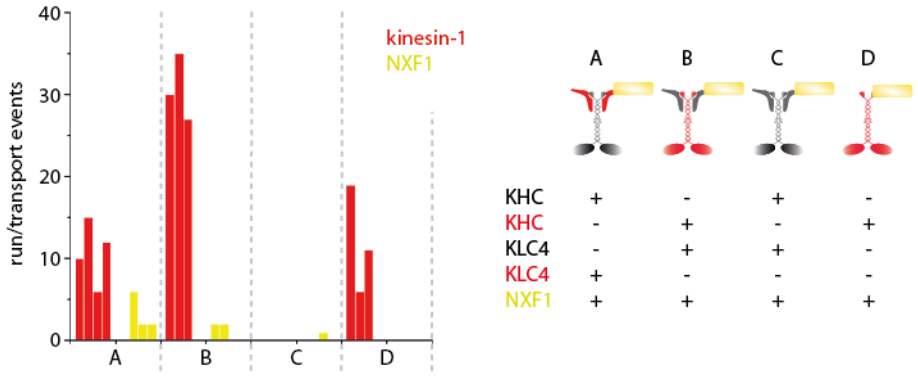

Figure 29: KLC4 is crucial for NXF1 transport. Using kinesin-1 concentrations normalized relative to a bovine serum albumin standard, we compared transport efficiencies of NXF1 by the different KLC4-containing kinesin-1 heterotetramers in comparison to dimeric KIF5A HC. Concentrations of kinesin-1 heterotetramers were diluted 10-fold in comparison to previous in vitro reconstitution experiments. KLC4-containing kinesin-1 heterotetramers transported NXF1, whereas the KLC4-lacking AF647-KIF5A HC dimer did not transport NXF1. All experiments were performed at least in triplicates. The AF647-labeled component of each kinesin-1 variant is marked in red. NXF1-TMR is marked in yellow.

7.1.2. FEZ2 increases the co-transport of NXF1/SRSF3 via kinesin-1

After having determined that KLC4 is necessary for NXF1 transport, we set out to precisely determine the ratios of kinesin-1 run events vs. transported cargo. To do so, we performed experiments using light chain-labeled KIF5A/KLC4 heterotetramers.

Purified KLC4-SNAP has a high labeling ratio of 80%, we thus expect a majority of the KIF5A/KLC4-SNAP heterotetramers to carry at least one fluorescent AF647 dye, allowing us to count only those run events that include KLC4. Using this experimental setup, we were thus able to determine how additional cargo influences kinesin-1-based transport of NXF1.

In an exploratory reconstitution experiment, we first compared KIF5A/KLC4-AF647-mediated transport of NXF1 alone with that of NXF1 transport in the presence of FEZ2 and SRSF3 (Figure 30). Confirming our observations with unlabeled KIF5A/KLC4 (Figure 27), the presence of FEZ2 lead to an increase in KIF5A/KLC4-AF647-mediated transport of NXF1(/SRSF3). Importantly, transport of NXF1 was still dependent on KLC4 in the presence of FEZ2 and SRSF3 in these experiments, as seen by the overlap of the NXF1 and KLC4 signals in Figure 30B.

To understand which fraction of heterotetramers transports cargo, we next quantified NXF1 transport events relative to KIF5A/KLC4-AF647 run events in the presence of FEZ2 or SRSF3, respectively, as well as a combination of both (Figure 31).

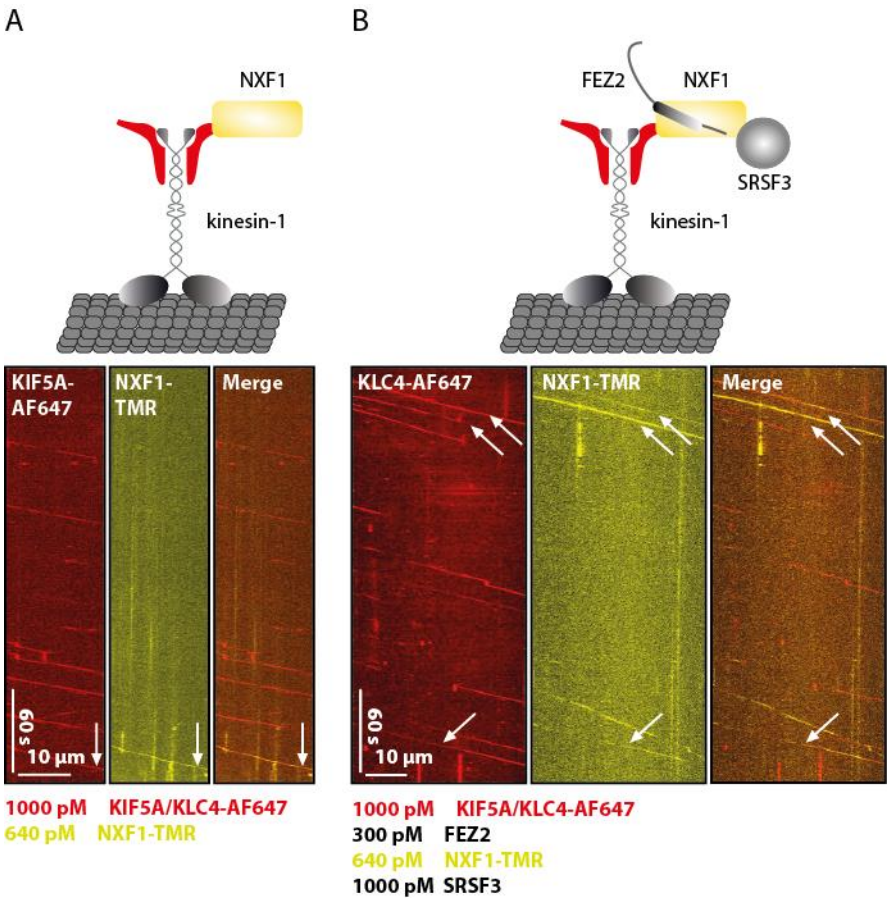

Figure 30: NXF1 transport depends on KLC4 and is increased in the presence of further cargo. Kymographs showing the dependency of NXF1 transport on KLC4 via an overlap of NXF1 and KLC4 signals (white arrows). **(A)** NXF1 transport by KIF5A/KLC4 heterotetramers. Overlaps of NXF1-TMR and KIF5A/KLC4-AF647 signals are marked with white arrows. **(B)** NXF1 transport by KIF5A/KLC4 heterotetramers in the presence of FEZ2 and SRSF3. Overlaps of NXF1-TMR and KIF5A/KLC4-AF647 signals are marked with white arrows.

In agreement with our previous observations (Figure 27 and Figure 30), the transport of NXF1 was significantly increased in the presence of a combination of FEZ2 and SRSF3 (Figure 31). In the presence of both, approximately 16% of KLC4-carrying kinesin-1 motors transported NXF1. In contrast, the presence of either SRSF3 or FEZ2 alone did not increase NXF1 transport efficiencies: While approximately 7% of KIF5A/KLC4 heterotetramers transported NXF1, approximately 8% of kinesin-1 heterotetramers transported combinations of NXF1 with either SRSF3 or FEZ2, respectively.

To finally determine whether kinesin-1 motility is affected by its type of cargo, we further measured the run length and velocity of kinesin-1 in the presence of different combinations of NXF1, FEZ2 and SRSF3 (Figure 31). We observed that neither kinesin-1 run length, nor velocity was affected by these combinations of cargo.

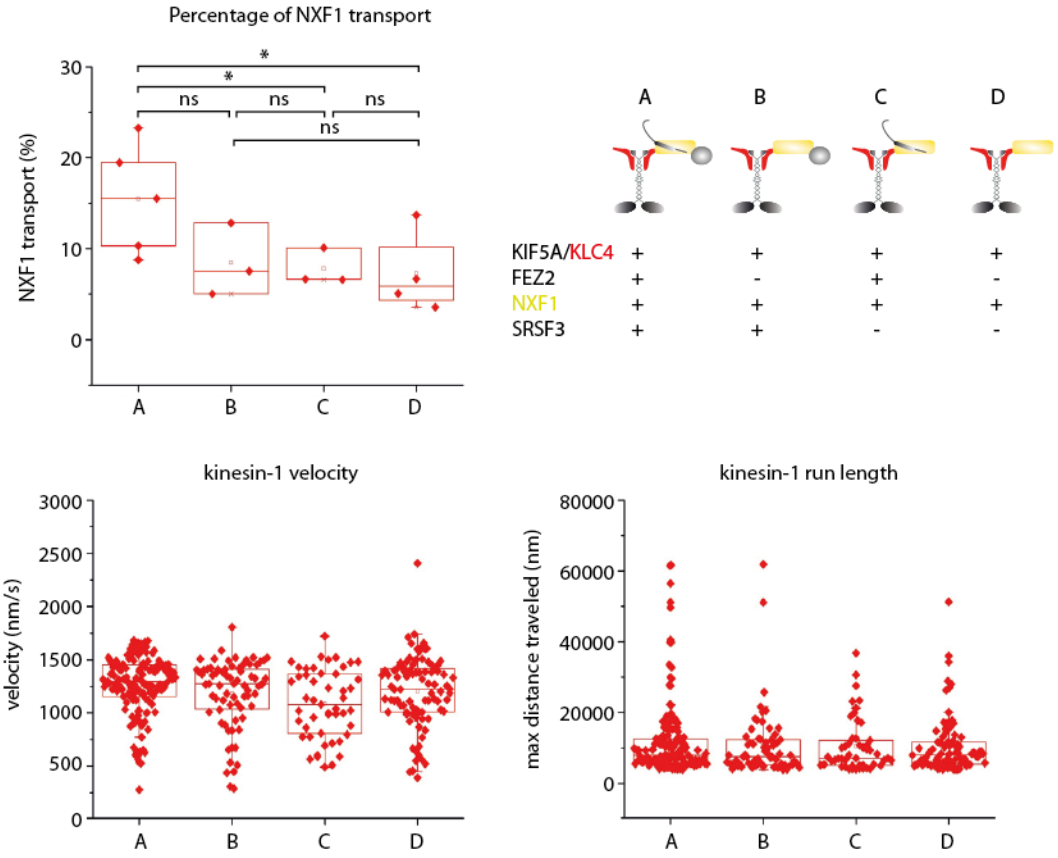

Figure 31: NXF1 transport is increased in the presence of FEZ2 and SRSF3. Comparison of kinesin-1-based NXF1 transport efficiencies in the presence/absence of additional factors. The included factors of each experiment as well as their fluorescent label (yellow: TMR; red: AF647) are displayed on the right. The velocity and run length of kinesin-1 are comparable in the presence different cargo. Each experiment was performed at least in triplicates.

7.1.3. An optimized TIRF-M assay buffer increases run/transport events

In comparison to other TIRF-M-based in vitro reconstitution experiments performed in the Maurer group (S. Baumann et al. 2020; S. J. Baumann et al. 2022), the TIRF-M assay buffer used for the here presented in vitro reconstitution experiments up to this point contained a 2-fold higher concentration of $MgCl_2$. To test whether the Mg^{2+} concentration influences kinesin-1 run length, velocity and cargo transport, we compared kinesin-1 motility in the two TIRF-M assay buffers, containing either 5.0

mM or 2.5 mM $MgCl_2$, respectively (Figure 32). Strikingly, in the presence of a lower Mg^{2+} concentration, the number of processive kinesin-1 events per 5 min movie was approximately 4x higher than in the TIRF-M assay buffer with a higher Mg^{2+} concentration. For all following TIRF-M in vitro reconstitution experiments, the $MgCl_2$ concentration was thus adjusted to 2.5 mM.

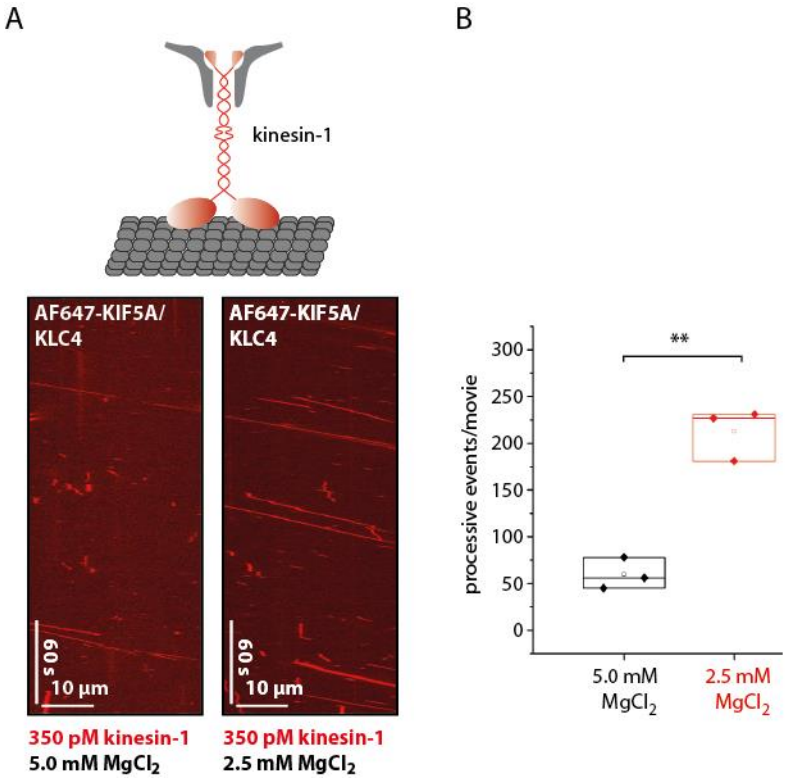

Figure 32: Effect of Mg^{2+} concentration on kinesin-1 processivity. (A) Kymographs comparing the processivity of kinesin-1 in TIRF-M assay buffer containing 5.0 mM and 2.5 mM $MgCl_2$, respectively. **(B)** Quantification of kinesin-1 run events per 5 min movie in TIRF-M assay buffer containing 5.0 mM and 2.5 mM $MgCl_2$, respectively.

Using the optimized TIRF-M assay buffer, we next analyzed whether the reduced Mg^{2+} concentration had an effect on kinesin-1-based cargo transport. TIRF-M in vitro reconstitution experiments under these conditions revealed that the increase in the number of processive kinesin-1 events (Figure 32) also led to an increase in the number of transport events of NXF1 alone (Figure 33A) and in combination with SRSF3 (Figure 33B), respectively.

In conclusion, we could show that NXF1 transport by kinesin-1 is dependent on its light chain KLC4. Although the percentage of NXF1 transport is increased in the presence of both SRSF3 and FEZ2, an optimized TIRF-M assay buffer led to an

increase in the number of processive kinesin-1 events and also to higher co-transport numbers of NXF1 and SRSF3 even in the absence of FEZ2.

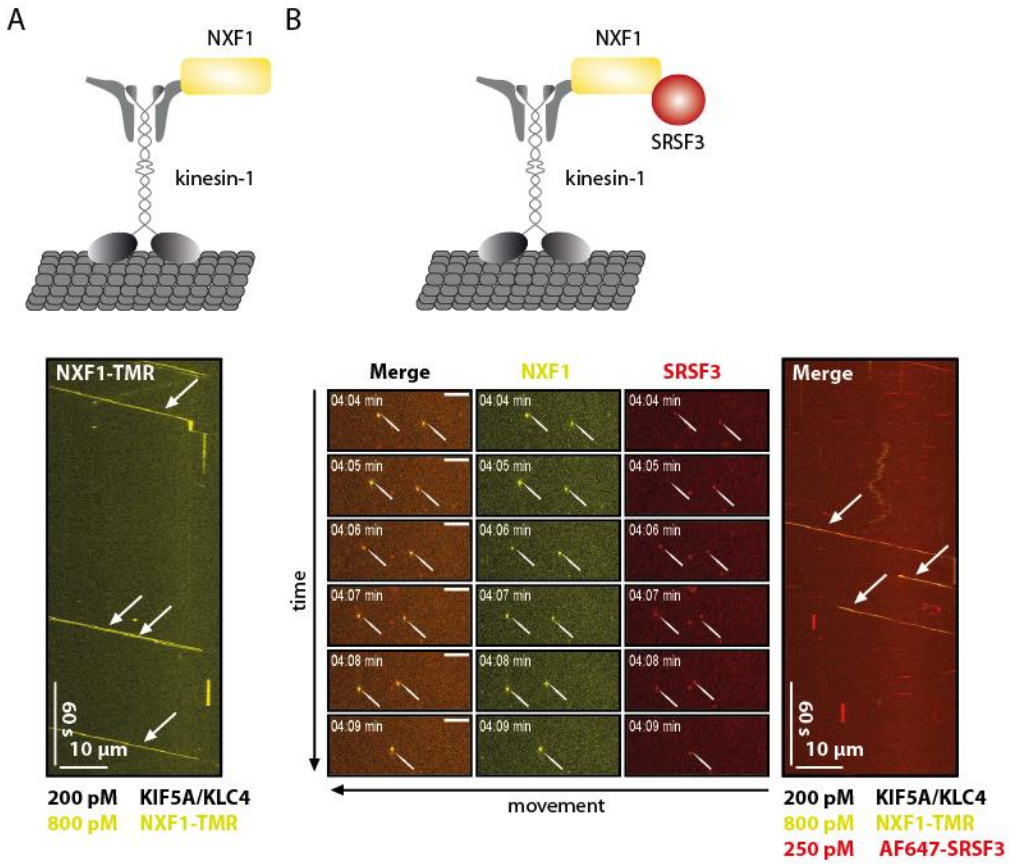

Figure 33: Lower Mg^{2+} concentration increases co-transport numbers of NXF1 and SRSF3. (A) Kymograph showing increased numbers of NXF1 transport events. **(B)** Left: Screenshots of a 5 min TIRF-M movie (at 04:04 min - 04:09 min) showing two co-transport events of NXF1 and SRSF3. Transport proceeds in the right-to-left direction. Scalebar: 5 µm. Right: Kymograph showing increased numbers of NXF1/SRSF3 co-transport events in the optimized TIRF-M assay buffer.

7.2. Discussion

After having observed that FEZ2 is transported by kinesin-1 and potentially increases the amount of NXF1/SRSF3 co-transport events in exploratory reconstitution experiments, the aim of this chapter was to determine specificities and motility parameters of the analyzed kinesin-1-based transport system.

In the previous chapters, the rec-YnH- and NanoBRET-based link between KLC4 and NXF1 (Figure 11) was exclusively analyzed using either KIF5A HC-labeled or unlabeled KIF5A/KLC4 heterotetramers. However, as purified KIF5A/KLC4

heterotetramer samples are accompanied by KIF5A HC dimer/oligomer populations (Figure 18 and Supplementary Figure 5), and direct binding to KIF5A HC had been reported for a few other kinesin-1 cargoes (Sun et al. 2011; Williams et al. 2014; Woźniak and Allan 2006), it was important to verify whether NXF1 transport is indeed dependent on KLC4. The here presented in vitro reconstitution experiments using purified, KIF5A/KLC4-AF647 heterotetramers thus enabled a precise analysis of the link between KLC4 and NXF1.

Using KIF5A/KLC4-AF647, we were able to determine that KLC4 is required for kinesin-1-based NXF1 transport (Figure 30). In agreement with this finding, NXF1 is not transported in the absence of KLC4 (Figure 29), validating the NXF1-KLC4 link reported via rec-YnH and NanoBRET approaches (Figure 11) and being in agreement with the identification of potential KLC4 interaction motifs found in NXF1 (see section 4.1.1). These results suggest a potentially different binding mode of NXF1 compared to other kinesin-1 cargoes that bind to the kinesin-1 heavy chain (Sun et al. 2011; Williams et al. 2014; Woźniak and Allan 2006), confirming the role of kinesin-1 light chains in cargo recognition and binding (Pernigo et al. 2013, 2018; Woźniak and Allan 2006; Zhu et al. 2012). These studies highlight the kinesin-1 light chain tetratricopeptide repeat domain for cargo recognition, usually recognizing tryptophan-acidic motifs in cargoes. Whether the tryptophan-acidic motif is important for the interaction between KLC4 and NXF1, which harbors two of these motifs (see section 4.1.1), is yet to be analyzed.

The quantitative analysis of transport events showed that NXF1 is most efficiently transported in the presence of both FEZ2 and SRSF3 (Figure 31), which confirms previous more qualitative observations (Figure 27). Interestingly, we could not observe a significant increase of kinesin-1-based NXF1 transport events in the presence of only FEZ2, although the rec-YnH and NanoBRET screens as well as previous more qualitative experiments (Figure 25 and Figure 27) showed that FEZ2 can interact with both NXF1 and KLC4.

Different explanations for the dependency of efficient NXF1 transport on the presence of both FEZ2 and SRSF3 are possible. The simultaneous binding of SRSF3 and FEZ2 to NXF1 could lead to a refolding of NXF1, potentially relieving its described autoinhibition (Müller-McNicoll et al. 2016; Viphakone et al. 2012) more efficiently than via SRSF3 alone. Alternatively, the simultaneous binding of FEZ2 and SRSF3 could lead to a change in charge that favors NXF1 binding to kinesin-1 heterotetramers. Finally, the presence of two additional proteins, increasing the overall concentration of proteins in the in vitro reconstitution experiment, might lead to unspecific oligomerization or phase separation, a phenomenon that has been observed previously in the Maurer group for a wide range of proteins at higher

concentrations, promoting transport in an artificial way. However, for unspecific oligomerization, likely resulting in more kinesin-1 heterotetramers attached to a higher molecular weight NXF1/SRSF3/FEZ2 complex, we would expect an increased kinesin-1 run length due to a lower probability of dissociation from microtubules. By comparing the kinesin-1 run length in the presence of NXF1 alone or in combination with FEZ2 and SRSF3 (Figure 31), we do not observe any differences, making unspecific oligomerization improbable.

However, the median run lengths of 7100 – 8000 nm we obtained for KIF5A/KLC4 complexes (in the presence or absence of cargo) are significantly higher than that reported for KIF5A/KLC1 complexes, where the median run length is described to be 1490 nm (interquartile range: 780 – 2840 nm) (Chiba et al. 2022). In the Maurer group, a higher run length has also been observed previously for TIRF-M-based in vitro reconstitution experiments using dimeric KIF3 or KIF5A HC (S. Baumann et al. 2020; S. J. Baumann et al. 2022), and might depend on specific experimental conditions. Considering that our observed cargo transport does not result from unspecific oligomerization, and that our system shows a certain selectivity (Figure 28), the higher run length of KIF5A/KLC4 heterotetramers still allows us to draw meaningful conclusions from transport experiments.

We further observed that a lower Mg^{2+} concentration in the TIRF-M assay buffer significantly increases the number of processive kinesin-1 events per 5 min movie. The inhibitory effect of an excess of free Mg^{2+} has been observed previously for kinesin as well as myosin motors, and is related to the inhibition of ADP release from the active site as well as the lowering of the affinity of motor proteins for microtubules or actin, respectively (Nitta, Okada, and Hirokawa 2008; Rosenfeld, Houdusse, and Sweeney 2005; Swenson et al. 2014).

Using a lower Mg^{2+} concentration, we were not only able to increase the number of processive kinesin-1 events, but also that of NXF1 transport events (Figure 33). Strikingly, under these optimized conditions, efficient NXF1/SRSF3 co-transport was obtained in the absence of FEZ2. This confirmed our initial hypothesis that kinesin-1 light chain KLC4 as well as the two RBPs NXF1 and SRSF3 represent the core protein components of the proposed RNA transport system (Figure 11). The extended network factor FEZ2 (Figure 25) might nevertheless be able to further increase kinesin-1-based co-transport of the core network proteins NXF1 and SRSF3 by facilitating their interaction with kinesin-1. This would align with the increase in NXF1/SRSF3 co-transport events we observed in the presence of FEZ2 using a higher Mg^{2+} concentration (Figure 31), and be in agreement with the kinesin-1 adaptor function described for the FEZ2 paralog FEZ1 (Teixeira, Alborghetti, and Kobarg 2019).

In conclusion, we identified optimal conditions for the reconstitution of an RBP transport system incorporating kinesin-1 (KIF5A/KLC4 heterotetramers), NXF1 and SRSF3. In the next chapter, we will analyze whether this RBP transport system is both capable of and sufficient for the transport of RNA. Although we could determine that FEZ2 is not required for the efficient co-transport of NXF1 and SRSF3, it may further increase co-transport numbers. In order to maximize the potential transport of RNA, we thus included it in further in vitro reconstitution experiments.

8. THE RECONSTITUTED RBP SYSTEM TRANSPORTS RNA

8.1. Results

After having reconstituted a functional and stable RBP transport system consisting of the core rec-YnH network components kinesin-1, NXF1 and SRSF3, as well as the optional extended network component FEZ2, we next set out to analyze whether this system can also transport RNA.

8.1.1. Selection of a suitable mRNA candidate

As described above (see section 1.6.2), 3'UTR length has recently been proposed to be an indicator for neuronal mRNA localization. mRNA transcripts enriched in the neuropil were reported to have significantly longer 3'UTRs than mRNA transcripts in the soma (Middleton, Eberwine, and Kim 2019; Tushev, Glock, Heumüller, et al. 2018) (see section 1.6.2, Figure 6A). One such example is CamKIIα mRNA (Figure 7), a highly abundant mRNA in neurons which harbors three tandem 3'UTR isoforms of differing lengths. The mRNA's peripheral destination is related to the associated 3'UTR isoform: the longer the isoform, the more distal the transcript localizes within dendrites (Tushev, Glock, Heumüller, et al. 2018) (Figure 7).

In the previous chapters, we could show that the two main RBP components of the rec-YnH network, the nuclear export factor NXF1 and the 3'UTR length-regulator SRSF3, can be efficiently co-transported by the microtubule motor protein kinesin-1 in vitro. In cells, SRSF3 is known to promote the generation of long 3'UTRs (see section 1.10.2), remains bound to these, and promotes their export from the nucleus to the cytoplasm by association with NXF1 (see section 1.9.1). We hence chose the middle and long CamKIIα 3'UTR isoforms, driving their mRNA transcript's localization to distal parts of dendrites, as suitable candidates to study in the context of mRNA transport via the reconstituted RBP system.

8.1.2. Analysis of SRSF3 motifs in CamKIIα 3'UTR

We were first interested in analyzing whether the middle and long 3'UTR isoforms of CamKIIα mRNA harbor SRSF3 motifs. We therefore searched for known SRSF3 motifs in the literature and additionally used information from unpublished data (personal communication with Michaela Müller-McNicoll) (Figure 34A). Many of the identified motifs are not unique, and allow for nucleotide (nt) variation at some positions in the sequence (Figure 34A, motifs 1, 2, 3, 9 and 10) (Änkö 2014b;

Hargous et al. 2006) (see section 1.11.2). We next determined the abundance of the identified motifs in the three different CamKIIα 3'UTRs, including the short (850 nt), middle (1629 nt) and long (3116 nt) isoforms. As tandem 3'UTRs, the sequences of the three 3'UTRs overlap (Figure 34B), therefore the entire sequences of the short and the middle 3'UTR isoforms are incorporated in the long 3'UTR isoform.

We found a comparatively large number of partially overlapping SRSF3 motifs in the three CamKIIα 3'UTR isoforms: 192 motifs in the long 3'UTR, 124 motifs in the middle 3'UTR and 56 motifs in the short 3'UTR isoform (Figure 34 and Supplementary Figure 11). The SRSF3 motifs can be categorized into two distinct sets: unique and repetitive motifs. While motif 9 is a unique motif exclusively present in the long 3'UTR, the abundance of motifs 1, 2 and 10 increases from the short to the long 3'UTR isoform (Figure 34B).

A

Name	Motif	Source
SRSF3 motif 1	[AT]C[AT][AT]C	10.1016/j.semcdb.2014.03.011 1084-9521
SRSF3 motif 2	CTC[TG]TC[CT]	10.1016/j.semcdb.2014.03.011 1084-9521
SRSF3 motif 3	ATCA[AT]CG	10.1016/j.semcdb.2014.03.011 1084-9521
SRSF3 motif 4	TTCTTCATCC	10.1186/s12915-019-0630-z
SRSF3 motif 5	CACCACCACC	10.1016/j.bbagrm.2013.11.006
SRSF3 motif 6	CCTCTTCC	10.1038/sj.emboj.7601385
SRSF3 motif 7	CCTCGTCC	10.1038/sj.emboj.7601385
SRSF3 motif 8	TCATCATCTTCATCG	M. Müller-McNicoll, personal communication
SRSF3 motif 9	[CT][AT]CTTCAT	10.1016/s1097-2765(01)00233-7
SRSF3 motif 10	C[ACTG][CT]C	10.1042/BST20210325

B

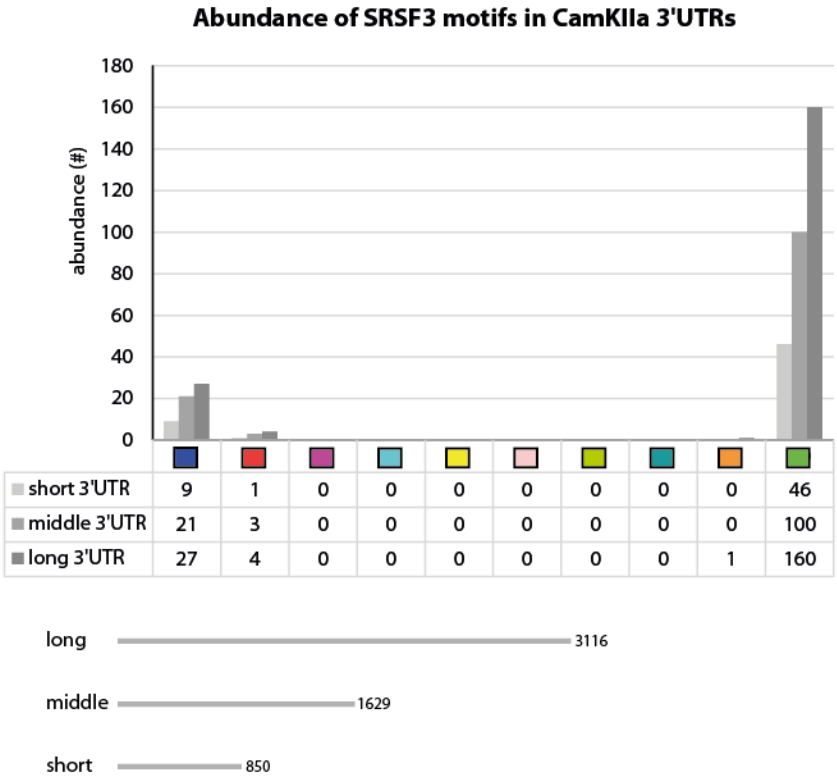

Figure 34: Abundance of SRSF3 motifs in rat CamKIIα 3'UTR isoforms. SRSF3 motifs were obtained from the literature and using information from unpublished data (personal communication with Michaela Müller-McNicoll) (Änkö 2014b; Hargous et al. 2006; Yingqun Huang and Steitz 2001; Jang et al. 2014; Jia and Zheng 2009; Middleton, Eberwine, and Kim 2019; Slišković, Eich, and Müller-McNicoll 2022). Nucleotides enclosed in brackets indicate the possibility of distinct nucleotides at the specified position, e.g. [AT] allows for adenine or thymine (uracil in RNA) at the given position. **(B)** Abundance of SRSF3 motifs in the short (850 nt), middle (1629 nt) and long (3116 nt) 3'UTR isoforms of rat CamKIIα mRNA. The long 3'UTR isoform harbors 192 motifs, the middle 3'UTR harbors 124 motifs and the short 3'UTR harbors 56 motifs.

8.1.3. In vitro reconstitution of an RNA transport system

We next set out to determine whether the reconstituted RBP transport system can transport RNA in our TIRF-M-based in vitro reconstitution experiments. As an RNA to test in these experiments, we used a 60 nucleotide sequence from the long and middle CamKIIα 3'UTR isoforms (SRSF3 RNA #1) which harbors three distinct SRSF3 motifs: motifs 1, 2 and 10. Whereas motifs 1 and 2 are present in one copy each in the RNA, motif 10 is present in multiple copies (Figure 35A-B).

In a first step, we analyzed the interaction of SRSF3 RNA #1 with different subcomplexes of the reconstituted RBP transport system in TIRF-M-coupled in vitro reconstitution experiments. We initially tested a combination of SRSF3 RNA #1 with KIF5A/KLC4 alone, showing that the motor itself was interestingly able to transport RNA in low numbers.

To test whether the presence of NXF1 affected RNA transport by KIF5A/KLC4, we then analyzed a combination of KIF5A/KLC4, NXF1 and SRSF3 RNA #1 in the vitro reconstitution experiments. Strikingly, we observed that the kinesin-1 heterotetramer can co-transport NXF1 and RNA (Figure 35C), and that the presence of NXF1 led to an increase in the number of RNA transport events (Figure 35E). Importantly, by simultaneously tracking NXF1 and RNA, we could determine that NXF1 and RNA did not dissociate from one another during their run, suggesting that the transported complex is stable over time.

To exclude the possibility that the observed increase in RNA transport events resulted from a non-specific interaction of the TMR dye bound to SNAP-tagged NXF1, we exchanged fluorescently labeled NXF1 with unlabeled, non-SNAP-tagged NXF1, and tested it in combination with KIF5A/KLC4 and SRSF3 RNA #1 (Figure 35D). The number of RNA transport events was comparable in the presence of fluorescently labeled and unlabeled NXF1, respectively, showing that the SNAP-tag and fluorescent TMR dye do not influence RNA transport (Figure 35Figure 35E).

In conclusion, we determined that although the KIF5A/KLC4 heterotetramer can occasionally transport RNA alone, it also co-transports NXF1 and RNA, which results in an overall increase in RNA transport efficiency.

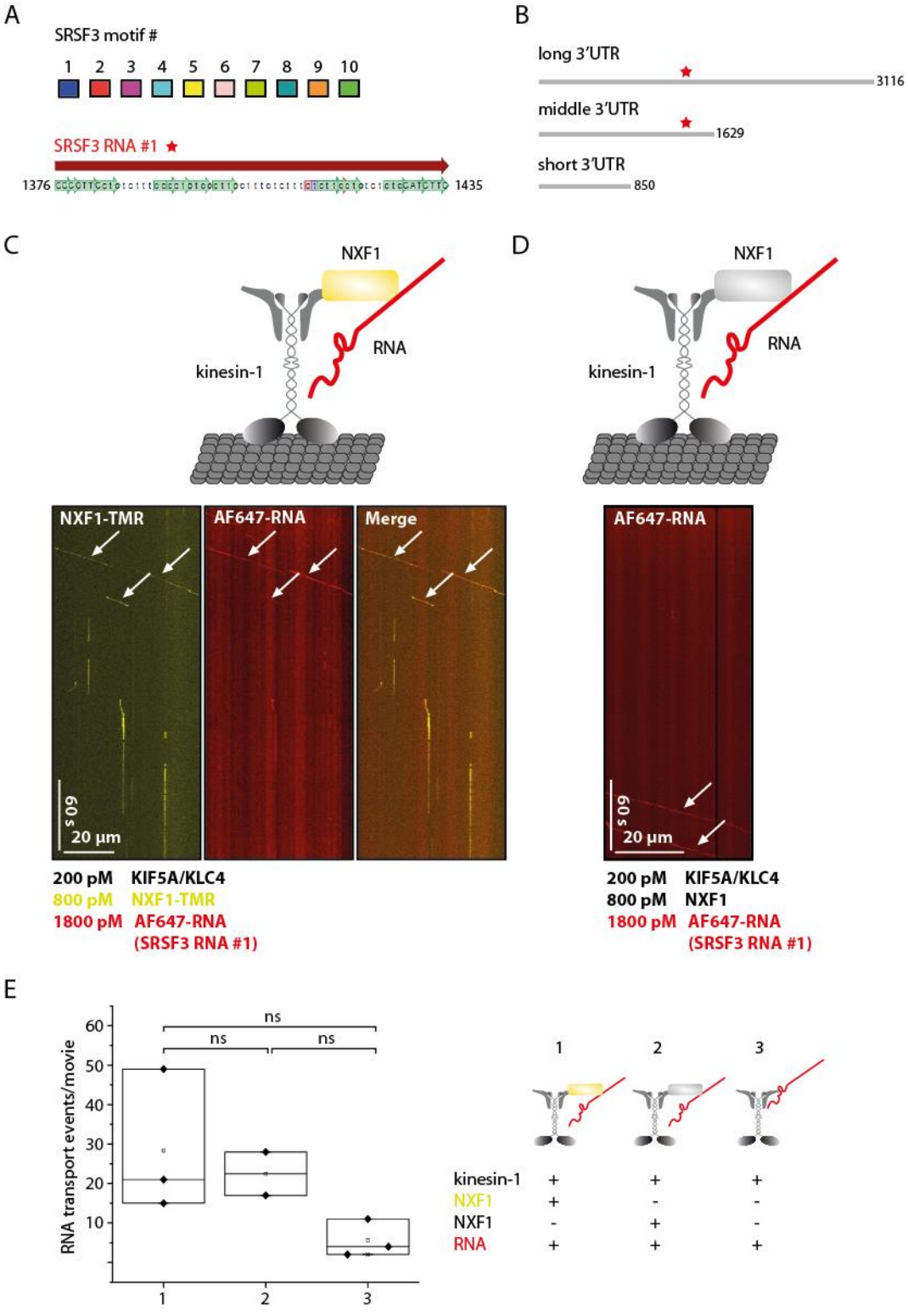
A
SRSF3 motif #
1 2 3 4 5 6 7 8 9 10
SRSF3 RNA #1
1376
1435
B
long 3'UTR
3116
middle 3'UTR
1629
short 3'UTR
850
C
NXF1
RNA
kinesin-1
NXF1-TMR
AF647-RNA
Merge
60 s
20 µm
200 pM KIF5A/KLC4
800 pM NXF1-TMR
1800 pM AF647-RNA
(SRSF3 RNA #1)
D
NXF1
RNA
kinesin-1
AF647-RNA
60 s
20 µm
200 pM KIF5A/KLC4
800 pM NXF1
1800 pM AF647-RNA
(SRSF3 RNA #1)
E
RNA transport events/movie
ns
ns
ns
1
2
3
kinesin-1 + + +
NXF1 + - -
NXF1 - + -
RNA + + +

Figure 35: RNA is transported by individual components of the RBP transport system. (A) SRSF3 RNA #1 was chosen based on a 60 nucleotide sequence in the middle and long 3'UTR isoforms of CamKIIα mRNA according to the presence of different SRSF3 motifs in varying quantities. SRSF3 motifs 1-10 are marked in different colors represented by the individual boxes. **(B)** The stars mark where the SRSF3 RNA #1 sequence is located within the long and middle CamKIIα 3'UTRs, respectively. **(C)** Kinesin-1/NXF1 complexes transport SRSF3 RNA #1 in the absence of FEZ2 and SRSF3 (white arrows). **(D)** Transport of SRSF3 RNA #1 is not dependent on the SNAP-tag/AF647 dye on NXF1. **(E)** The number of SRSF3 RNA #1 transport events differs in the presence of either kinesin-1 alone or kinesin-1/NXF1 complexes, respectively.

8.1.4. Analysis of the specificity of the RNA transport system

While NXF1 alone is reported to bind RNA without sequence specificity in its active state (Viphakone et al. 2012; Walsh, Hautbergue, and Wilson 2010) (see section 1.9.1), SRSF3 is known to recruit NXF1 to specific motifs within 3'UTRs of mRNAs (Müller-McNicoll et al. 2016) (see section 1.11.2). We thus expected the presence of SRSF3 to convey RNA-binding specificity to the reconstituted system.

To analyze whether SRSF3 affects the specificity of RNA transport by the reconstituted system, we used two more 60 nucleotide sequences from the long CamKIIα 3'UTR isoform (SRSF3 RNA #2 as well as a negative control RNA (- control RNA)) as RNAs to test in comparison to SRSF3 RNA #1 (Figure 36A-B). In contrast to SRSF3 RNA #1, SRSF3 RNA #2 harbors fewer copies of the repetitive motif 10, and additionally harbors the unique motif 9 (Figure 34 and Figure 36A). The negative control RNA, on the other hand, does not harbor any SRSF3 motifs (Figure 36A). Using a combination of these RNAs, we aimed to study whether RNA transport relies on unique motifs within the RNA sequences or on an additive effect resulting from the presence of multiple copies of repetitive motifs.

To try to maximize the transport of RNA in the specificity-related TIRF-M-coupled in vitro reconstitution assays, we further added FEZ2 to the RNA transport system. As expected, SRSF3 RNA #1 was transported by the in vitro RBP system comprising kinesin-1, FEZ2, NXF1 and SRSF3 (Figure 36C). When comparing the transport of SRSF3 RNA #1 to that of SRSF3 RNA #2 and the negative control RNA (- control RNA), the transport system showed different selectivities (Figure 36D). Strikingly, there is a significant difference in the transport of SRSF3 RNA #1 vs. SRSF3 RNA #2, suggesting that the transport system can bind RNA with some sequence specificity. Nevertheless, the negative control RNA, which we expected not to be transported due to its lack of SRSF3 motifs, is surprisingly transported more efficiently than SRSF3 RNA #2. Thus, although the system can differentiate between different RNA sequences for transport, it currently remains unclear how the putative binding motifs affect RNA binding to the reconstituted transport system.

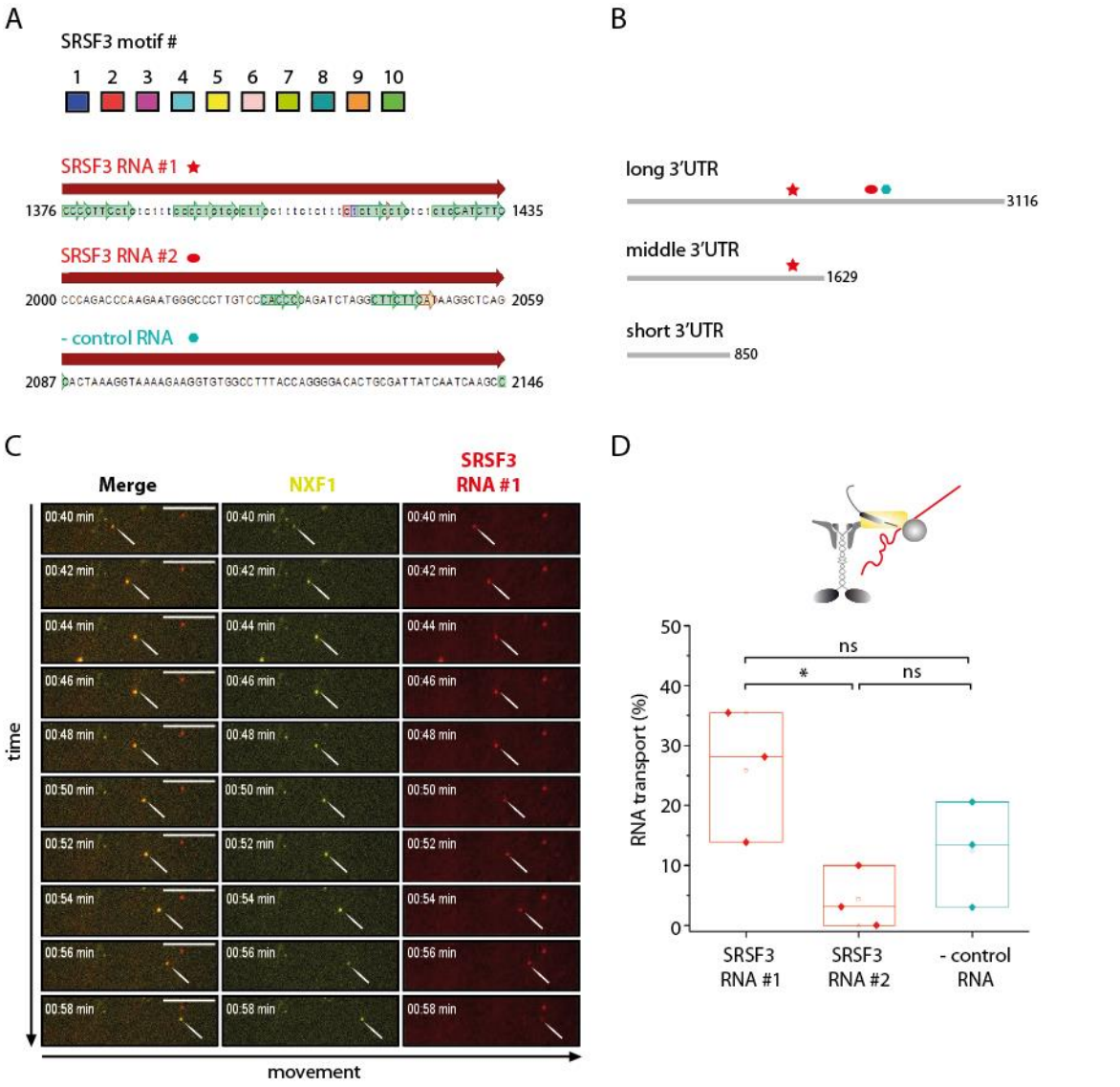

Figure 36. Selectivity of RNA transport. (A) Three RNA sequences (SRSF3 RNA #1, SRSF3 RNA #2, - control RNA) from the CamKIIα 3'UTR isoforms were chosen based on the presence or absence of SRSF3 motifs. SRSF3 motifs 1-10 are marked in different colors represented by the colored boxes. **(B)** Visualization of where the 60 nucleotide RNA sequences are located within the middle and long 3'UTR isoforms of rat CamKIIα mRNA. Red star: SRSF3 RNA #1, red oval: SRSF3 RNA #2, blue shape: - control RNA. **(C)** Screenshots of a TIRF-M movie (at 00:40-00:58 min out of 05:00 min) showing co-transport of NXF1 and SRSF3 RNA #1 in the presence of kinesin-1, FEZ2 and SRSF3. Transport proceeds in the left-to-right direction. Scalebar: 10 µm. **(D)** Comparison of the percentage of AF647-labeled RNA (SRSF3 RNA #1, SRSF3 RNA #2, - control RNA) transport in the presence of kinesin-1, FEZ2, NXF1-TMR and SRSF3.

8.2. Discussion

The aim of the work reported in this chapter was to analyze whether the reconstituted RBP transport system comprising either (1) kinesin-1 and NXF1 or (2) kinesin-1, FEZ2, NXF1 and SRSF3, respectively, can transport RNA.

We chose a sequence from the middle and long CamKIIα 3'UTR isoforms as a candidate RNA (SRSF3 RNA #1), as it harbors several SRSF3 motifs that comprise the core motif CNYC and thus potential NXF1 binding sites, facilitating NXF1-based export of SRSF3/mRNA complexes (Müller-McNicoll et al. 2016). Additionally, the middle and long 3'UTR isoforms are known to localize to more distal regions of dendrites compared to the short 3'UTR isoform (Tushev, Glock, Heumüller, et al. 2018) (Figure 7).

Our in vitro experiments show that heterotetrametric KIF5A/KLC4 itself transported SRSF3 RNA #1 to a certain extent. A similar observation was made recently by Dimitrova-Paternoga and colleagues, showing a direct interaction between RNA and a purified, recombinant Drosophila melanogaster kinesin heavy chain truncation (Dimitrova-Paternoga et al. 2021).

Strikingly, when NXF1 was added to the in vitro reconstitution experiments, kinesin-1 efficiently co-transported RNA and NXF1. Although we observe a clear trend for NXF1 alone increasing the number of RNA transport events independent of its fluorescent tag, we did not obtain sufficiently high numbers of RNA transport events in either the presence or absence of NXF1 yet. Further experiments are needed to validate the observed trend.

As NXF1 is described to be autoinhibited in the nucleus (Viphakone et al. 2012), a state in which it cannot bind mRNA, we initially expected kinesin-1/NXF1-based RNA transport to be possible only in the presence of SRSF3. In cells, mRNA-bound SRSF3 interacts with NXF1 to relieve its autoinhibition (Müller-McNicoll et al. 2016; Viphakone et al. 2012), leading to the export of NXF1/SRSF3/mRNA complexes from the nucleus to the cytoplasm. While autoinhibited NXF1 cannot bind mRNA, activated NXF1 can bind mRNA without sequence specificity (Viphakone et al. 2012; Walsh, Hautbergue, and Wilson 2010). Due to the increase in RNA transport events observed in the presence of kinesin-1/NXF1 complexes compared to kinesin-1 alone in our in vitro experiments, we thus consider it likely that at least a fraction of NXF1 is activated in our in vitro experiments even in the absence of SRSF3.

As SRSF3 recruits NXF1 to specific motifs in the 3'UTRs of neuronal mRNAs (Müller-McNicoll et al. 2016), we assumed that the presence of SRSF3 in the reconstituted system might not only increase the number of RNA transport events, but also the specificity of RNA transport. To analyze this, we further tested two additional 60 nucleotide sequences from the middle and long CamKIIα 3'UTR isoforms: SRSF3 RNA #2 and a negative control RNA.

In comparison to SRSF3 RNA #1, SRSF3 #2 RNA contains fewer repetitions of SRSF3 motif 10 as well as the unique motif 9 which is exclusively present in the long 3'UTR isoform. In the presence of kinesin-1, FEZ2, NXF1 and SRSF3, we observed a significantly lower number of SRSF3 RNA #2 vs. SRSF3 RNA #1 transport events. This suggests that unique motif 9 is not crucial for RNA transport by the reconstituted system. Instead, these results imply that it indeed might rather be the quantity of repetitive motifs, in this case motif 10, that is of relevance for RNA transport.

Alternatively, the folding of SRSF3 RNA #2 might render SRSF3 motifs, potentially also motif 9, inaccessible, resulting in lower numbers of SRSF3 RNA #2 transport. Surprisingly, SRSF3 RNA #2 is also transported less frequently than a negative control RNA lacking SRSF3 motifs, suggesting that we either missed a further SRSF3 motif in our analysis or an additional factor that may be important for the binding of SRSF3 and thus RNA to kinesin-1/NXF1 complexes in vitro experiments. Hence, although a difference in RNA transport numbers can be observed for SRSF3 motif #2 and the negative control RNA, this difference is not significant, possibly given the small number of data points. More experiments have to be performed in order to further analyze the potential specificity of the reconstituted system.

In conclusion, we were able to reconstitute an RNA transport complex using purified, recombinant proteins and RNA. While kinesin-1 transports RNA to a low extent by itself, a complex of kinesin-1 and NXF1 can more efficiently transport RNA in vitro (Figure 33). Although it has not been formally shown, we further conclude that SRSF3 is a member of the RNA transport complex, considering that (1) we obtained efficient co-transport of NXF1 and SRSF3 by kinesin-1 (Figure 33), (2) our reconstituted system shows to a certain degree different selectivities depending on the presence or absence of SRSF3 motifs (Figure 36); and (3) SRSF3 is known to activate NXF1 and to recruit it to 3'UTRs in cells (Müller-McNicoll et al. 2016). In the future, it will be important to perform additional experiments in which NXF1, SRSF3 and RNA are independently fluorescently labeled to unequivocally test if indeed they form an RNA transport complex together with kinesin-1 in vitro.

9. CONCLUSION

While mRNA transport has been studied for decades, we still lack a comprehensive understanding of how distinct distributions of thousands of mRNAs are generated in neurons, a process which is crucial for synaptic plasticity as well as long-term memory formation (Cajigas et al. 2012; Glock, Heumüller, and Schuman 2017; Taliaferro et al. 2016; Tushev, Glock, Heumüller, et al. 2018). To date, only a handful of adaptor proteins, such as adenomatous polyposis coli (S. Baumann et al. 2020; S. J. Baumann et al. 2022), have been identified to link specific zip code-containing neuronal mRNAs to the microtubule motor proteins dynein and kinesin for the transport of mRNAs along microtubules.

The Maurer lab has therefore developed a yeast-2-hybrid-based many-by-many protein screening approach, namely rec-YnH (Yang et al. 2018), to identify novel interactions between RNA-binding and microtubule-associated proteins.

The rec-YnH screening approach revealed a network of interactors (Figure 11) that proposes a connection between mRNA export, microtubule-based mRNA transport and 3'UTR length-dependent mRNA localization.

The aim of this thesis was thus to analyze this identified network of interactors (Figure 11), including the light chains of the microtubule motor proteins kinesin-1 and dynein, the nuclear export factor NXF1 as well as the 3'UTR length regulator SRSF3, in order to determine whether these components are necessary and sufficient to reconstitute RNA transport in vitro, and whether this potential RNA transport system can provide insight into how the delivery of mRNAs to distal destinations within neurons is achieved.

We determined that the central factor of the network, the nuclear export factor NXF1, harbors interaction motifs for both dynein and kinesin-1 light chains. Strikingly, using our TIRF-M-coupled in vitro reconstitution approach (Grawenhoff, Baumann, and Maurer 2022), we could show that NXF1 can indeed co-diffuse or be transported along microtubules by dynein and kinesin-1, respectively, validating the obtained rec-YnH screening data.

Although NXF1 has already been proposed to be involved in the microtubule-based transport of viral RNA in the past (Pocock et al. 2016), and further NXF1 family proteins were observed in neuronal RNA granules (see section 1.9.2), we here report the first indication of a direct interaction between NXF1 and microtubule motor proteins.

Furthermore, we were able to show that NXF1 and SRSF3 are co-transported by kinesin-1 via its light chain KLC4. NXF1 and SRSF3 have previously been described to interact directly with one another in pull-down and co-IP approaches (Hargous et al. 2006; Yingqun Huang et al. 2003). To date, it is however not clear whether the interaction is further stabilized by mRNA (Müller-McNicoll et al. 2016). Although we exclusively looked at the assembly of NXF1 and SRSF3 on kinesin-1, we could determine that RNA is not required in order for them to be co-transported.

Analyzing potential effects of additional extended rec-YnH network components (Figure 25) revealed that FEZ2, a paralog of the kinesin cargo adaptor FEZ1 (Teixeira, Alborghetti, and Kobarg 2019), can increase co-transport events of NXF1 and SRSF3. In agreement with the adaptor function of FEZ1, we thus determine that FEZ2 helps the assembly of kinesin-1/NXF1/SRSF3 complexes (see chapter 6). Various optimizations finally showed that FEZ2 is, however, not necessary for efficient kinesin-1-based co-transport of NXF1 and SRSF3.

We further identified that kinesin-1 itself is capable of inefficiently transporting RNA, a characteristic which has only recently been reported for the kinesin-1 heavy chain (Dimitrova-Paternoga et al. 2021). Strikingly, we show that NXF1 and RNA are co-transported via kinesin-1, and that NXF1 increases the amount of RNA transported by kinesin-1. This finding aligns with previous reports in the literature, stating that NXF1 harbors an N-terminal RNA-binding domain that can bind mRNA in a non-specific manner (Viphakone et al. 2012; Walsh, Hautbergue, and Wilson 2010), which would explain why the presence of NXF1 results in an increase in RNA transport numbers.

Furthermore, while NXF1 has been described to be involved in the trafficking of viral RNA via a constitutive transport element motif encoded in it (Pocock et al. 2016), NXF1 has different modes for binding to viral and messenger RNA, respectively. While it uses its N-terminal RNA-binding domain to bind to mRNA, it uses an alternative RNA-binding domain, consisting of its ΨRRM-LRR domains (see section 1.9.1), to bind to viral RNA. In contrast to the previous study on viral RNA (Pocock et al. 2016), we thus report the first instance of kinesin-1/NXF1-based RNA transport independent of the viral constitutive transport element, revealing that this transport mechanism is potentially of importance to the neuron itself.

Although our assays show that SRSF3 is not necessary for the in vitro transport of RNA via kinesin-1 and NXF1 per se, SRSF3 might be important for the in vivo transport of mRNA in combination with kinesin-1 and NXF1. In cells, SRSF3 is reported to promote 3’UTR lengthening and to recruit NXF1 to specific motifs within

the 3’UTR of mRNAs (Müller-McNicoll et al. 2016), resulting in the activation of NXF1 and the export of NXF1/SRSF3/mRNA complexes. In its free state, however, NXF1 is autoinhibited, a state in which it cannot bind mRNA, and instead requires adaptor proteins like SRSF3 to gain the ability to bind mRNA.

There is currently no reason to assume that SRSF3 is absent from the reconstituted RNA transport system, as (1) SRSF3 and NXF1 are efficiently co-transported by kinesin-1 in our in vitro reconstitution assay (Figure 33); (2) the reconstituted system likely shows different RNA-binding selectivities dependent on SRSF3 motifs; and (3) SRSF3 activates the mRNA-binding activity of NXF1 in cells, priming it for the nuclear export of NXF1/SRSF3/mRNA complexes (Müller-McNicoll et al. 2016). To unequivocally prove that SRSF3 is co-transported with kinesin-1/NXF1/RNA complexes, we nevertheless require additional experiments in which one can simultaneously track NXF1, SRSF3 and RNA via individual fluorescent tags on each component.

Considering that SRSF3 and NXF1 preferentially export mRNAs with long 3’UTRs from the nucleus to the cytoplasm in cells, the here described in vitro RNA transport system could potentially function as a 3’UTR length-dependent mRNA sorting system in cells. This system would then be responsible for exclusively sorting mRNAs with long 3’UTR isoforms to distal regions of dendrites or axons.

In conclusion, we report the first reconstitution of a minimal kinesin-1-based RNA transport system that can potentially simultaneously (1) connect mRNA export from the nucleus with microtubule-based mRNA transport in the cytoplasm, and (2) connect 3’UTR length regulation with mRNA localization within neurons.

10. OUTLOOK

An exciting new discovery in the mRNA localization field is that not only specific localization motifs (zip codes) within 3'UTRs, but also 3'UTR length in general, are important determinants for the localization of specific mRNAs in neurons. In particular, longer 3'UTR isoforms were identified to reach more distal locations within axons and dendrites compared to shorter 3'UTR isoforms. However, the required factors and mechanisms with which neurons accomplish 3'UTR length-dependent mRNA sorting are yet to be identified, representing a crucial step in understanding how neurons regulate processes such as synaptic plasticity and the formation of long-term memories.

Despite decades of research, a limitation in determining how specific mRNAs are localized to distal neuronal locations has been the missing knowledge on key components of mRNP transport complexes. In this thesis, we were able to reconstitute a novel RNP transport complex that suggests a connection between 3'UTR length regulation, mRNA export as well as mRNA transport, and hence builds the basis for the identification of an mRNA sorting system in neurons.

There are indications in the literature that point towards a potential function of the reconstituted NXF1/SRSF3/RNA transport system in 3'UTR length-dependent mRNA sorting. In particular, there are recent studies that determined that 3'UTRs enriched in dendrites and axons harbor SRSF3 motifs, deletion of which abolishes their localization (Middleton, Eberwine, and Kim 2019; Mikl et al. 2022). Furthermore, long 3'UTR isoforms were described to comprise a high number of unique motifs besides repetitive motifs already present in shorter isoforms (Tushev, Glock, Biever, et al. 2018). As such, the localization of specific mRNAs was proposed to either result from (1) unique localization motifs within the 3'UTR or (2) a broader localization potential resulting from the combination of several motifs within the 3'UTR (Mikl et al. 2022) (see section 1.10.3). Alternatively, mRNA localization has been proposed to result from liquid-liquid phase separation of the mRNA itself (reviewed in (Langdon and Gladfelter 2018)) or of (specific domains of) the adaptors linking mRNAs to motor proteins (Liao et al. 2019).

Provided that SRSF3 is indeed a component of the reconstituted RNP system, we can integrate these ideas to propose a model that introduces three different mechanisms with which neurons could regulate 3'UTR length-dependent mRNA sorting:

(a) Motor proteins are exclusively coupled to long 3'UTR isoforms via a unique SRSF3 motif encoded in them, leading to the transport of only long 3'UTR isoforms;

(b) Motor proteins transport long 3'UTR isoforms more efficiently due to the increase in SRSF3 motifs in longer vs. shorter 3'UTR isoforms;

(c) Motor proteins are preferentially coupled to long 3'UTR isoforms due to their higher probability to phase separate either alone or in combination with SRSF3.

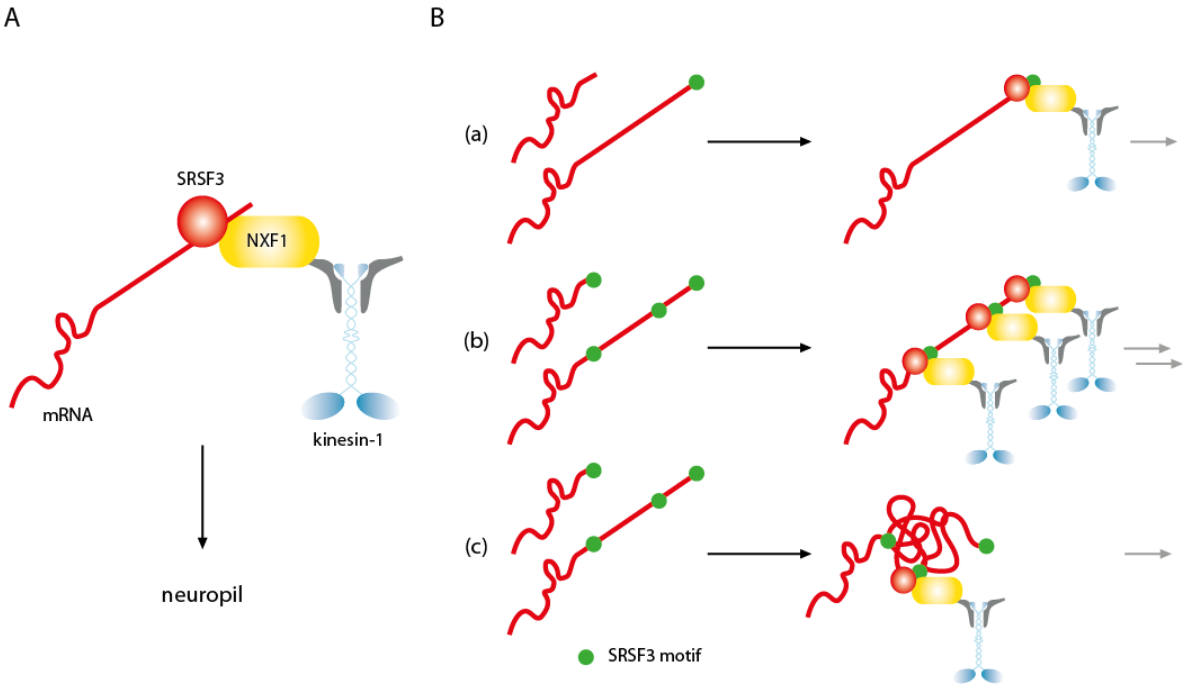

Figure 37: Different mechanisms could account for 3'UTR length-dependent mRNA sorting. **(A)** The proposed 3'UTR length-dependent mRNA sorting system comprises mRNA, SRSF3, NXF1 and a microtubule motor protein (exemplified for kinesin-1). **(B)** Three different mechanisms could account for 3'UTR length-dependent mRNA sorting: (a) Motor proteins are only coupled to long 3'UTR isoforms via a unique SRSF3 motif in them, meaning that only those transcripts with long 3'UTR isoforms get transported; (b) Motor proteins transport mRNAs harboring long 3'UTR isoforms more efficiently due to the increase in SRSF3 motifs in longer vs. shorter 3'UTR isoforms; and (c) Motor proteins are preferentially coupled to long 3'UTR isoforms via their higher probability to phase separate either alone or in combination with SRSF3.

Our reconstituted RNP transport system is uniquely positioned to determine the precise mechanism that 3'UTR length-dependent mRNA sorting underlies. Using the system to have a closer look at the different possibilities provided by the model, first results hint towards possibility (b), a more efficient transport of longer 3'UTR

isoforms due to an increase in (repetitive) SRSF3 motifs within them. Although it is premature to draw any definite conclusions from these exploratory experiments, the data we obtained shows that our in vitro reconstitution system, enabling the precise control over the presence/absence as well as quantity of SRSF3 motifs in a given RNA, is highly effective in further investigating the different mechanisms described by the proposed model.

We expect that future research on the reconstituted RNP transport system, which we propose to function as a potential neuronal 3'UTR length-dependent mRNA sorting system, will help to elucidate the mechanism neurons employ to ensure the localization of mRNAs to their precise destinations. We anticipate that this will ultimately contribute to the understanding of not only processes like synaptic plasticity-underlying long-term memory formation, but also neurological disorders associated with their dysregulation, as for example epilepsy.

11. SUPPLEMENT

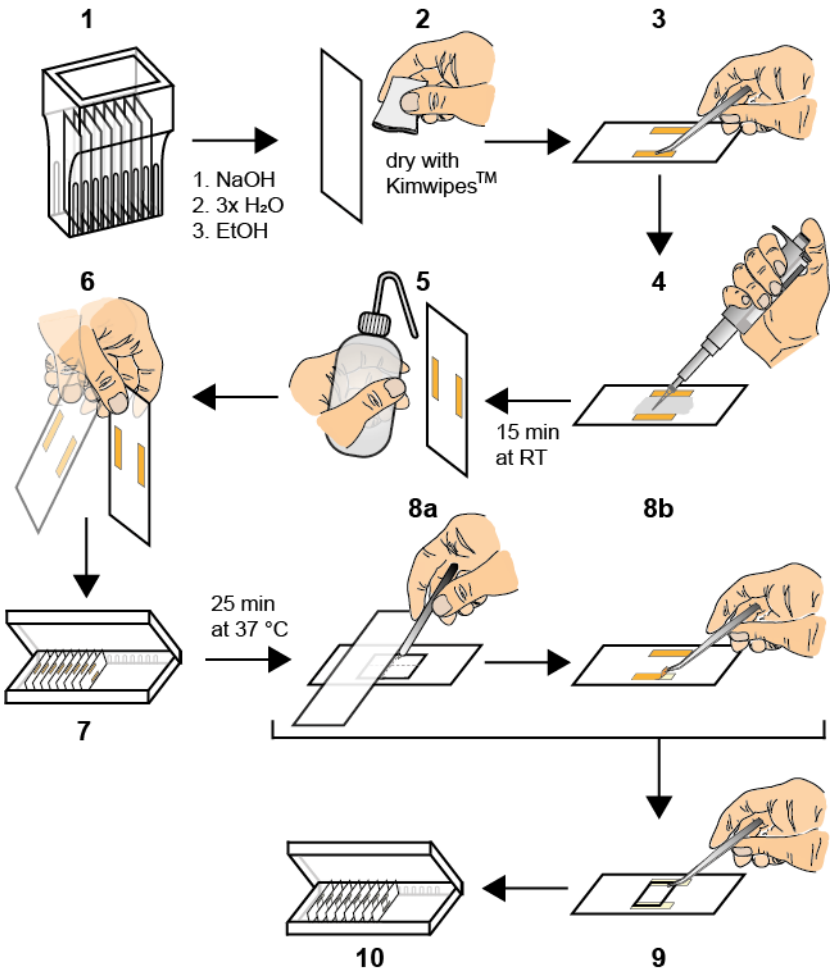

Supplementary Figure 1: TIRF-M assay chamber preparation. Glass slides are cleaned via subsequent wash steps with NaOH, H_2O and EtOH (1). They are then dried (2), supplied with two strips of double-sided tape (3) and passivated with PLL-PEG (4). Residual PLL-PEG is removed via a wash step with H_2O (5), and glass slides are dried via a swift movement of the wrists (6) as well as incubation at 37°C (7). Biotinylated coverslips are then cut into four equal pieces and attached to the double-sided tape strips on the passivated glass slides (8a-9). The resulting TIRF-M chambers are placed in a box and stored at 4°C until further use (10). Figure taken from (Grawenhoff, Baumann, and Maurer 2022).

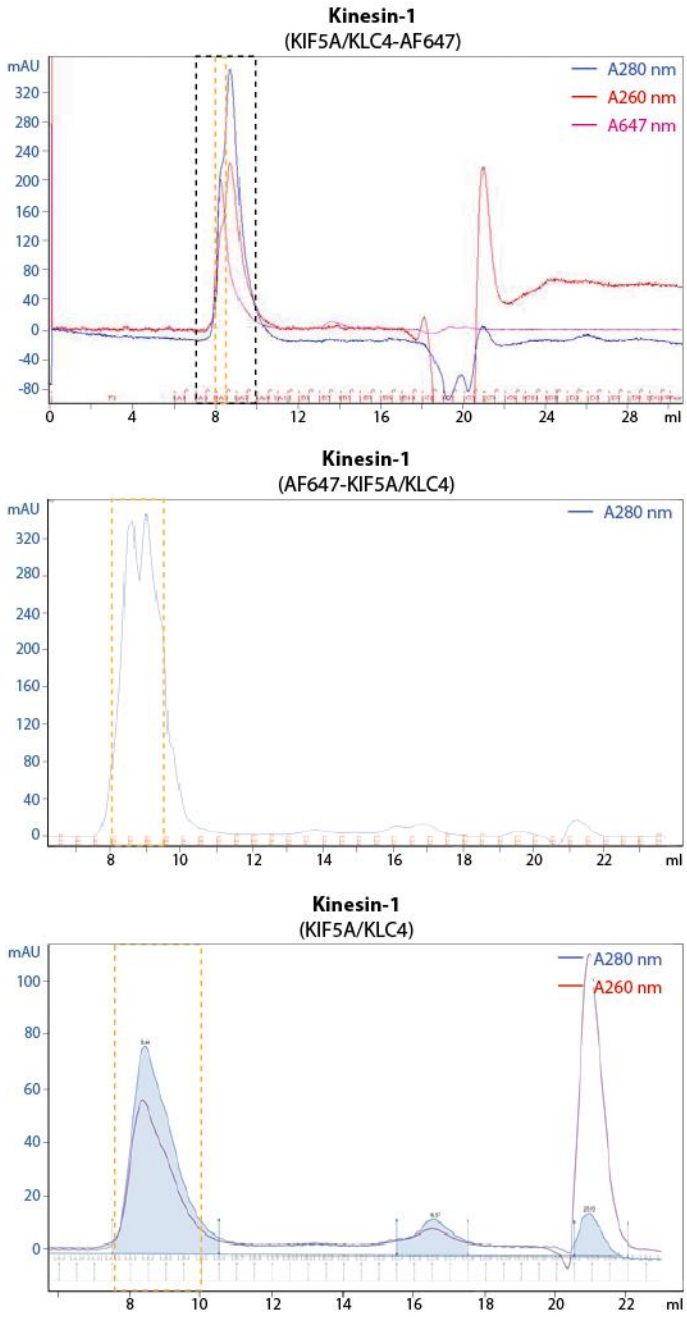

Supplementary Figure 2: Size exclusion chromatograms of kinesin-1 purifications. Top: Chromatogram of the KIF5A/KLC4-AF647 heterotetramer purification. Middle: Chromatogram of the AF647-KIF5A/KLC4 heterotetramer purification. Bottom: Chromatogram of the KIF5A/KLC4 heterotetramer purification. Dotted gray rectangles: KIF5A/KLC4-SNAP heterotetramer size exclusion chromatography fractions analyzed via SDS-PAGE in Figure 18, dotted yellow rectangles: selection of fractions for further purification.

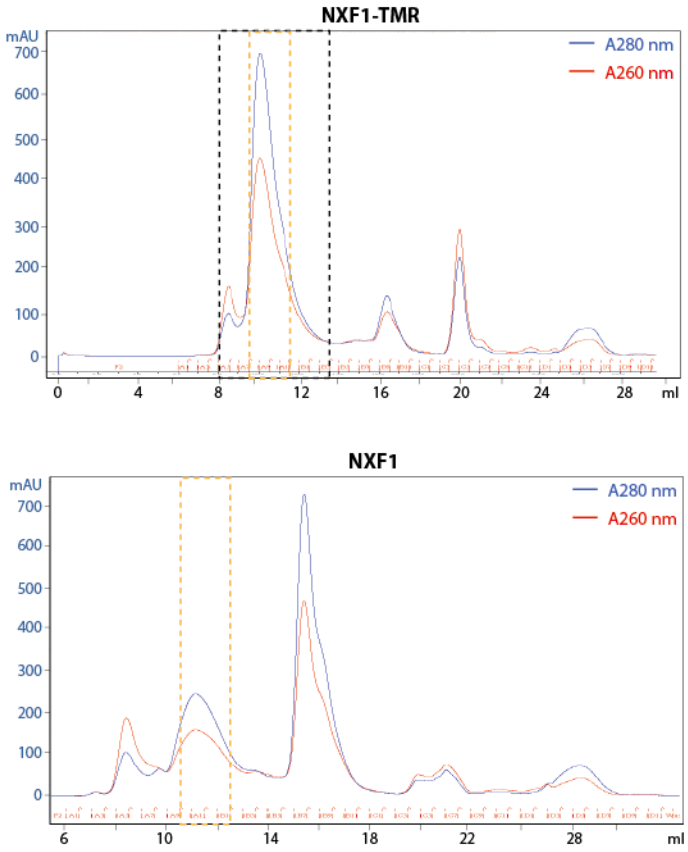

Supplementary Figure 3: Size exclusion chromatograms of NXF1 purifications. Top: Chromatogram of the NXF1-TMR purification, bottom: Chromatogram of the NXF1 purification. Dotted gray rectangles: NXF1-SNAP size exclusion chromatography fractions analyzed via SDS-PAGE in Figure 20, dotted yellow rectangles: selection of fractions for further purification.

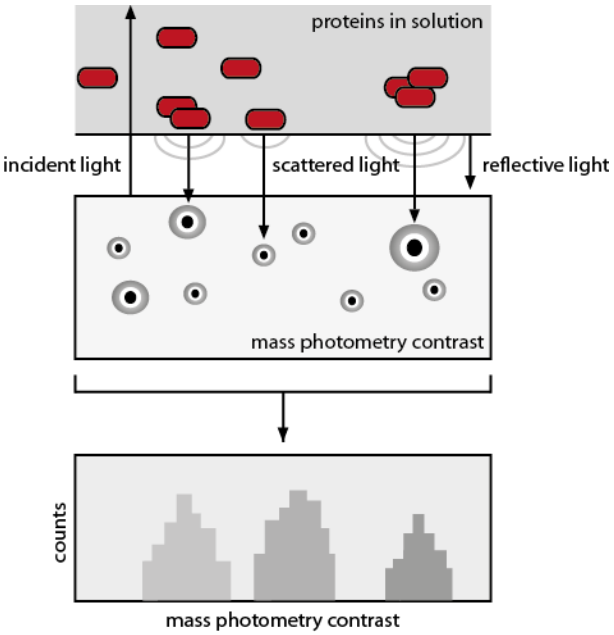

Supplementary Figure 4: Mass photometry principle. Proteins in solution scatter light according to their molecular mass. The resulting contrast can be translated into the molecular weight of the analyzed protein(s). Figure was designed based on: https://www.refeyn.com/about-mass-photometry.

Obtained values (kDa)		Matched values (kDa)	
	Control		
Peak 1:	-41 kDa	41 kDa	Background
Peak 2:	41 kDa		

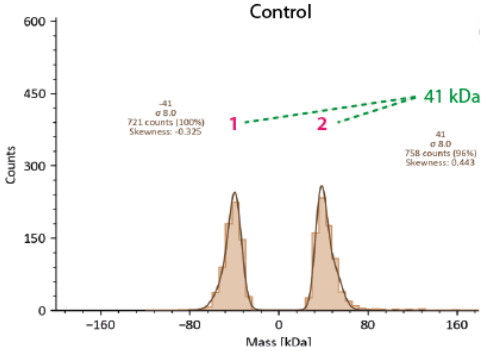

	KIF5A/KLC4		
Peak 1:	38 kDa	41 kDa	Background
Peak 2:	134 kDa	234 kDa	KHC dimer
Peak 3:	238 kDa	69 kDa	KLC4 monomer
Peak 4:	378 kDa	138 kDa	KLC4 dimer
Peak 5:	480 kDa	372 kDa	KHC/KLC4 heterotetramer
		303 kDa	KHC dimer/KLC4 monomer
		468 kDa	KHC tetramer

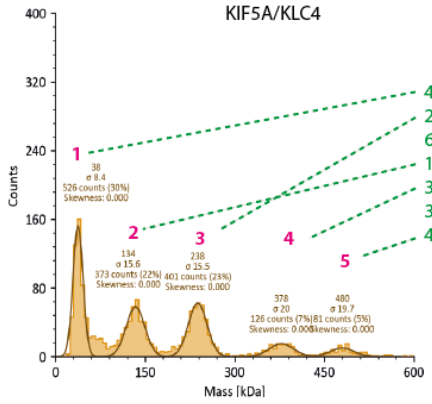

	KIF5A/KLC4-AF647		
Peak 1:	45 kDa	41 kDa	Background
Peak 2:	94 kDa	234 kDa	KHC dimer
Peak 3:	181 kDa	91 kDa	KLC4-SNAP monomer
Peak 4:	240 kDa	182 kDa	KLC4-SNAP dimer
Peak 5:	413 kDa	372 kDa	KHC/KLC4-SNAP heterotetramer
Peak 6:	490 kDa	303 kDa	KHC dimer/KLC4-SNAP monomer
Peak 7:	696 kDa	468 kDa	KHC tetramer

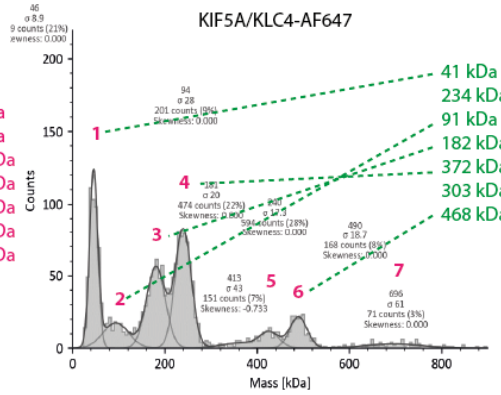

	AF647-KIF5A/KLC4		
Peak 1:	44 kDa	41 kDa	Background
Peak 2:	133 kDa	278 kDa	SNAP-KHC dimer
Peak 3:	280 kDa	69 kDa	KLC4 monomer
Peak 4:	417 kDa	138 kDa	KLC4 dimer
Peak 5:	566 kDa	416 kDa	SNAP-KHC/KLC4 heterotetramer
Peak 6:	691 kDa	347 kDa	SNAP-KHC dimer/KLC4 monomer
		557 kDa	SNAP-KHC tetramer

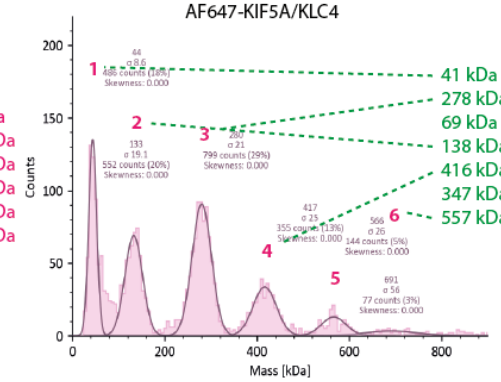

Supplementary Figure 5: Analysis of the oligomeric states of kinesin-1. Mass photometry was used to determine the oligomeric states of the different kinesin-1 heterotetramers: KIF5A/KLC4, AF647-KIF5A/KLC4 and KIF5A/KLC4-AF647. Individual samples were measured in TIRF-M assay buffer (90 mM HEPES, 10 mM PIPES, 2.5 mM $MgCl_2$, 1.5 mM EGTA, 15 mM BME, pH 6.95) supplemented with 2.5 mM ATP. The background (buffer) signal was subtracted from the measured peaks. On the left, the measured molecular weight of individual peaks is noted (pink). On the right, the peaks are assigned (via dashed green lines) to the expected components in each sample (green) based on calculated molecular weights.

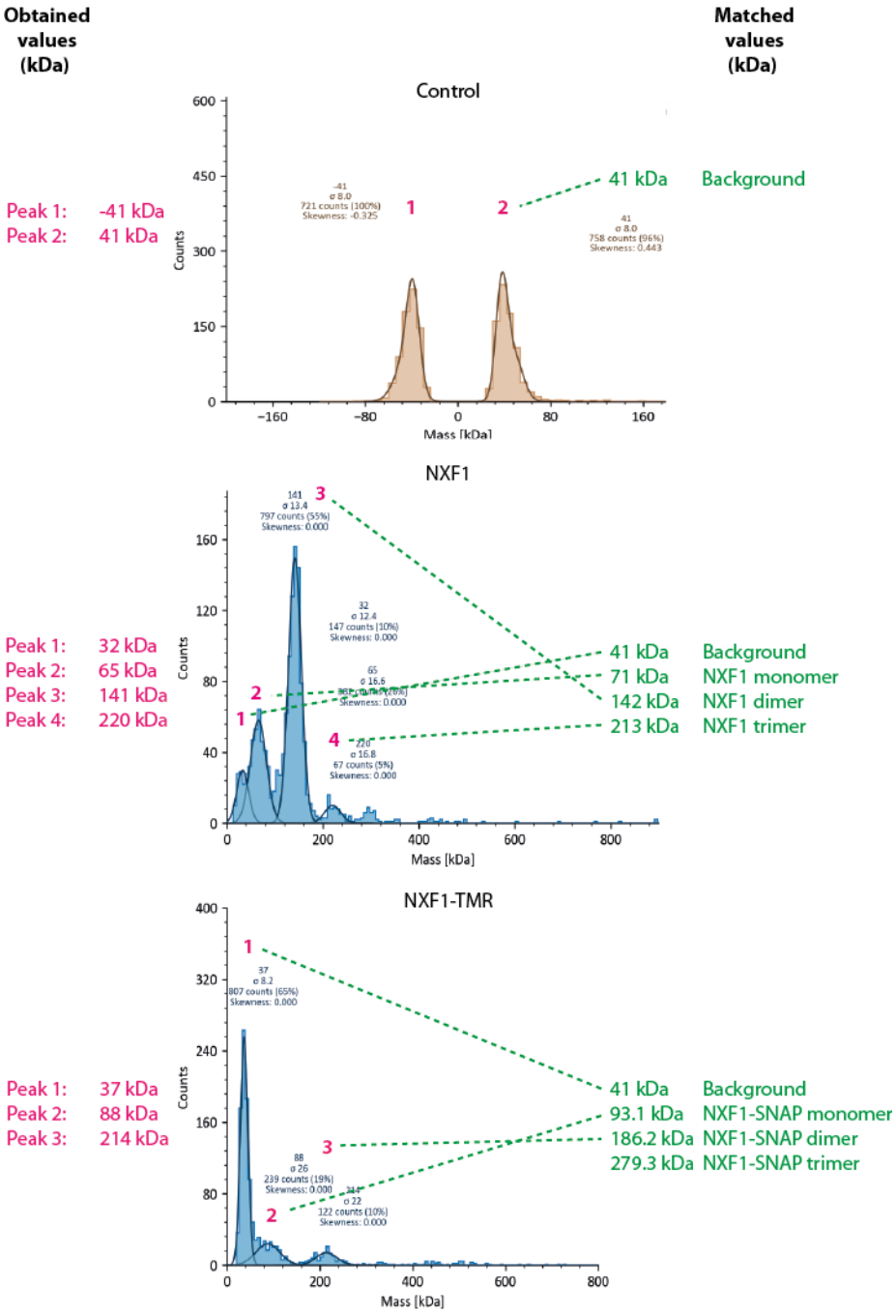

Supplementary Figure 6: Analysis of the oligomeric states of NXF1 and NXF1-TMR. Mass photometry was used to determine the oligomeric states of NXF1 and NXF1-TMR. Individual samples were measured in TIRF-M assay buffer (90 mM HEPES, 10 mM PIPES, 2.5 mM $MgCl_2$, 1.5 mM EGTA, 15 mM BME, pH 6.95) supplemented with 2.5 mM ATP. The background (buffer) signal was subtracted from the measured peaks. On the left, the measured molecular weight of individual peaks is noted (pink). On the right, the peaks are assigned (via dashed green lines) to the expected components in each sample (green) based on calculated molecular weights.

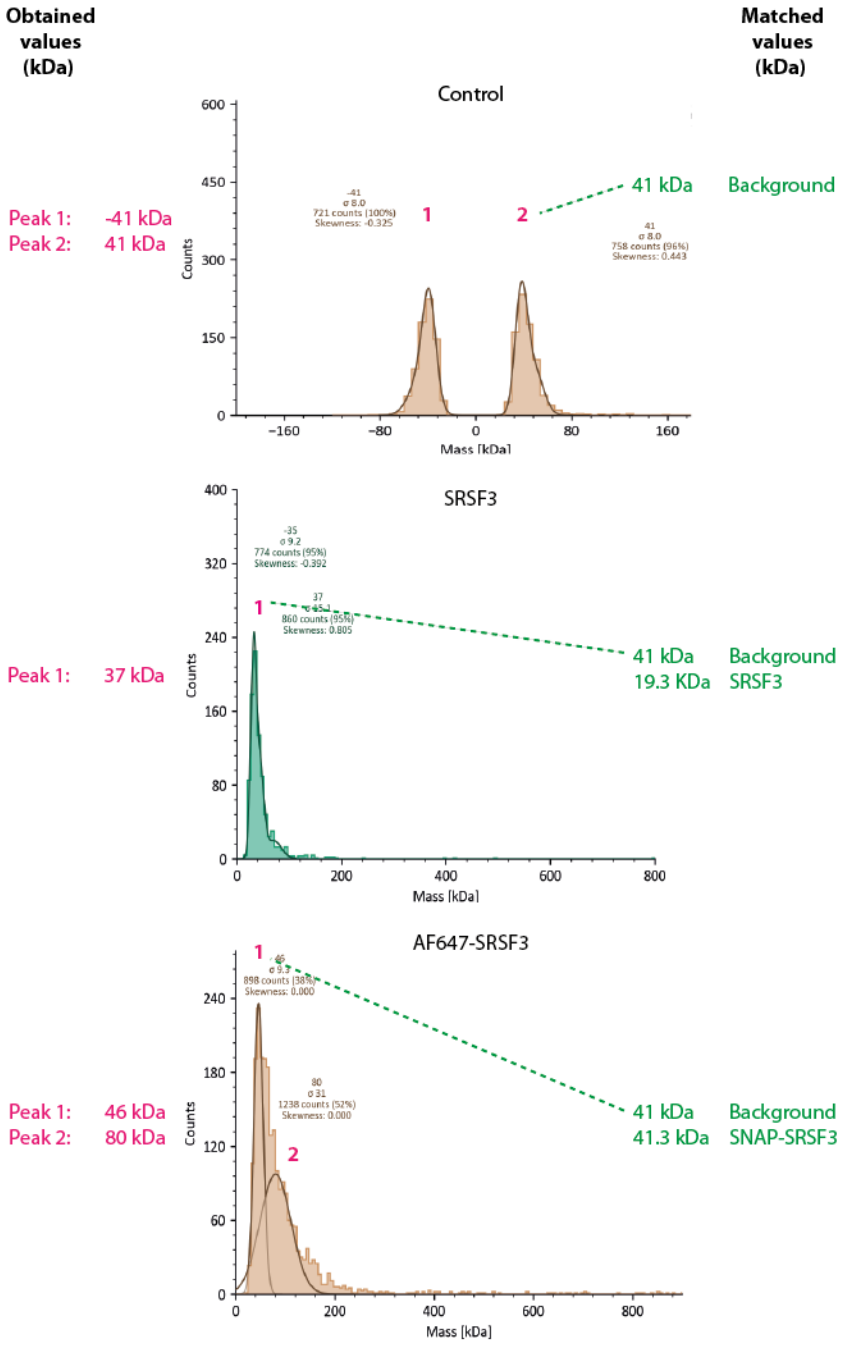

Supplementary Figure 7: Analysis of the oligomeric states of SRSF3 and AF647-SRSF3. Mass photometry was used to determine the oligomeric states of SRSF3 and AF647-SRSF3. Individual samples were measured in TIRF-M assay buffer (90 mM HEPES, 10 mM PIPES, 2.5 mM $MgCl_2$, 1.5 mM EGTA, 15 mM BME, pH 6.95) supplemented with 2.5 mM ATP. The background (buffer) signal was subtracted from the measured peaks. On the left, the measured molecular weight of individual peaks is noted (pink). On the right, the peaks are assigned (via dashed green lines) to the expected components in each sample (green) based on calculated molecular weights.

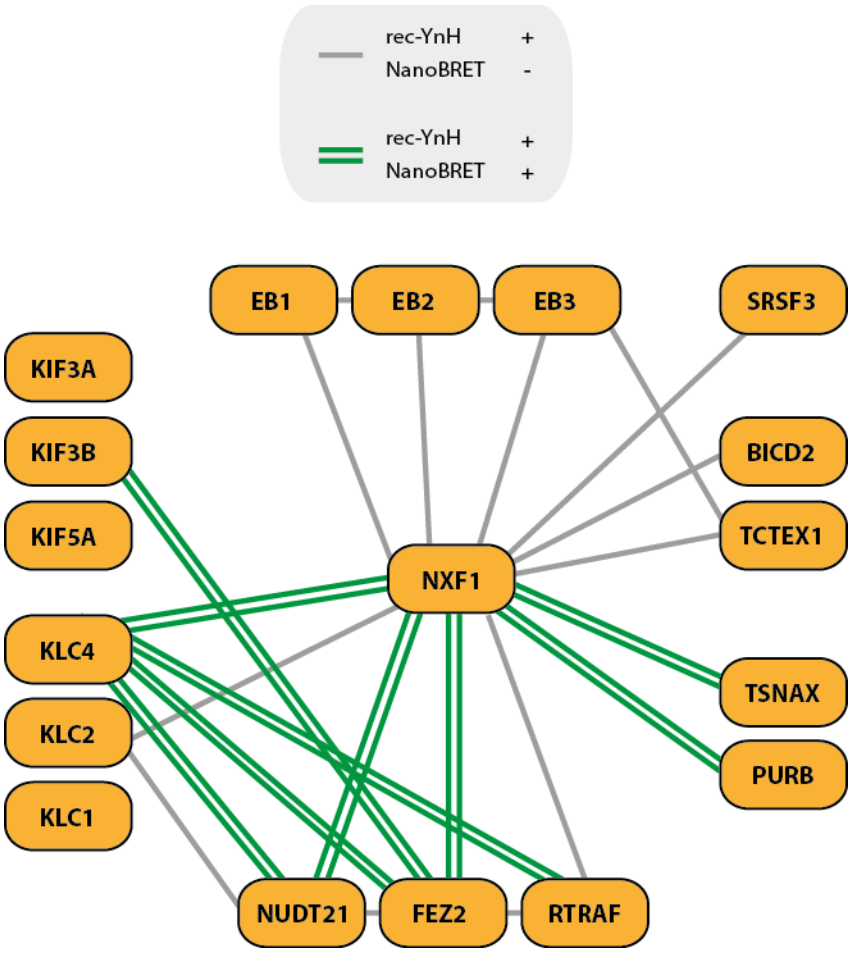

Supplementary Figure 8: Extended rec-YnH network shows that NXF1 is a hub for protein interactions. Interactions between NXF1 and a multitude of proteins such as microtubule motor protein light chains (KLC1, KLC2, KLC4), microtubule end-binding proteins (EB1, EB2, EB3), a dynein light chain (Tctex1) and adaptor (BICD2) as well as others were identified via rec-YnH screening and verified via the NanoBRET approach. Green: rec-YnH and NanoBRET positive; gray: rec-YnH positive, NanoBRET negative.

Obtained values (kDa)

Matched values (kDa)

Control

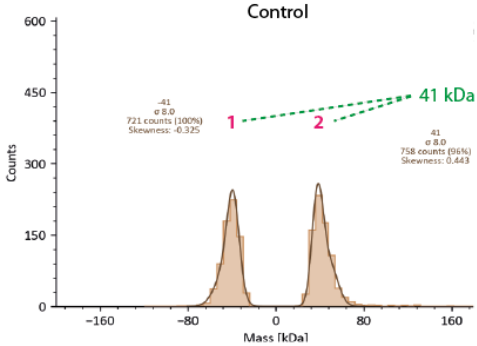

Peak 1: -41 kDa
Peak 2: 41 kDa

41 kDa Background

RTRAF vs. RTRAF-AF647

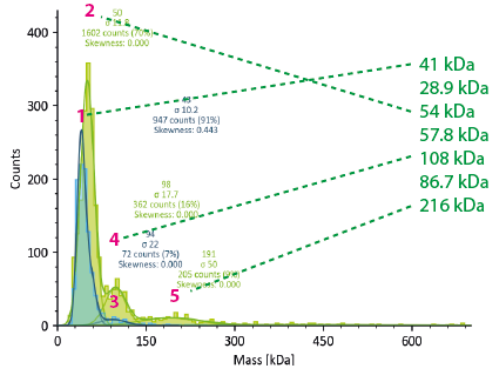

Peak 1: 43 kDa
Peak 2: 50 kDa
Peak 3: 94 kDa
Peak 4: 98 kDa
Peak 5: 191 kDa

41 kDa Background
28.9 kDa RTRAF monomer
54 kDa RTRAF-AF647 monomer
57.8 kDa RTRAF dimer
108 kDa RTRAF-AF647 dimer
86.7 kDa RTRAF trimer
216 kDa RTRAF-AF647 trimer

NudT21 vs. NudT21-AF647

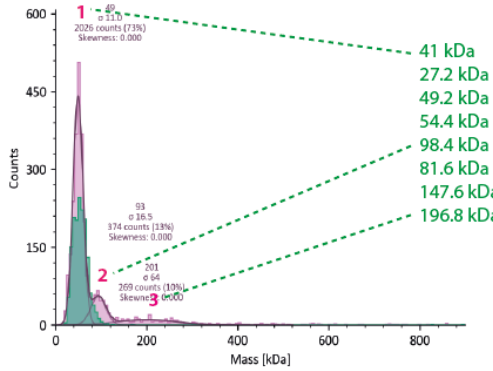

Peak 1: 49 kDa
Peak 2: 93 kDa
Peak 3: 201 kDa

41 kDa Background
27.2 kDa NudT21 monomer
49.2 kDa NudT21-AF647 monomer
54.4 kDa NudT21 dimer
98.4 kDa NudT21-AF647 dimer
81.6 kDa NudT21 trimer
147.6 kDa NudT21-AF647 trimer
196.8 kDa NudT21-AF647 tetramer

FEZ2 vs. AF647-FEZ2

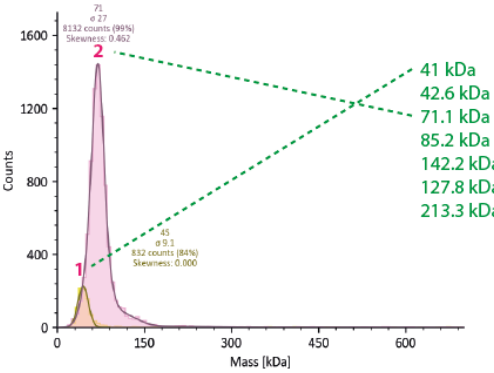

Peak 1: 45 kDa
Peak 2: 71 kDa

41 kDa Background
42.6 kDa FEZ2 monomer
71.1 kDa AF647-FEZ2 monomer
85.2 kDa FEZ2 dimer
142.2 kDa AF647-FEZ2 dimer
127.8 kDa FEZ2 trimer
213.3 kDa AF647-FEZ2 trimer

Supplementary Figure 9: Analysis of the oligomeric states of RTRAF, NudT21 and FEZ2. Mass photometry was used to determine the oligomeric states of RTRAF(-AF647), NudT21(-AF647) and (AF647-)FEZ2. Individual samples were measured in TIRF-M assay buffer (90 mM HEPES, 10 mM PIPES, 2.5 mM $MgCl_2$, 1.5 mM EGTA, 15 mM BME, pH 6.95) supplemented with 2.5 mM ATP. The background (buffer) signal was subtracted from the measured peaks. On the left, the measured molecular weight of individual peaks is noted (pink). On the right, the peaks are assigned (via dashed green lines) to the expected components in each sample (green) based on calculated molecular weights.

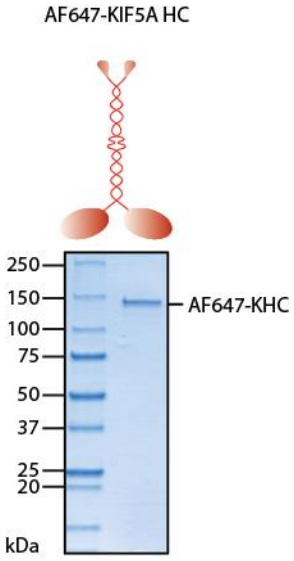

Supplementary Figure 10: Purified AF647-labeled KIF5A HC. AF647-KIF5A HC was purified by Sebastian Baumann.

Supplementary Figure 11. A total of 192 SRSF3 motifs were found in the long 3'UTR isoform of CamKIIα mRNA. SRSF3 motifs were obtained from the literature as well as unpublished data (personal communications with Michaela Müller-McNicoll) (Änkö 2014b; Hargous et al. 2006; Yingqun Huang and Steitz 2001; Jang et al. 2014; Jia and Zheng 2009; Middleton, Eberwine, and Kim 2019; Slišković, Eich, and Müller-McNicoll 2022). **(B)** SRSF3 motifs (colors shown in (A)) found in the long 3'UTR of rat CamKIIα mRNA. (C) Abundance of SRSF3 motifs in the short, middle and long 3'UTRs of rat CamKIIα mRNA.

12. REFERENCES

Aizawa, H. et al. 1992. “Kinesin Family in Murine Central Nervous System.” *Journal of Cell Biology* 119(5): 1287–96.

Alborghetti, M. R. et al. 2010. “Human FEZ1 Protein Forms a Disulfide Bond Mediated Dimer: Implications for Cargo Transport.” *Journal of Proteome Research* 9(9): 4595–4603.

Alborghetti, Marcos R., Ariane S. Furlan, and Jörg Kobarg. 2011. “FEZ2 Has Acquired Additional Protein Interaction Partners Relative to FEZ1: Functional and Evolutionary Implications.” *PLoS ONE* 6(3).

Alcott, Callison E. et al. 2020. “Partial Loss of CFIM25 Causes Learning Deficits and Aberrant Neuronal Alternative Polyadenylation.” *eLife* 9: 1–30.

An, Juan Ji et al. 2008. “Distinct Role of Long 3′ UTR BDNF MRNA in Spine Morphology and Synaptic Plasticity in Hippocampal Neurons.” *Cell* 134(1): 175–87.

Aniento, F., Neil Emans, Greyson Griffiths, and Jean Gruenberg. 1993. “Cytoplasmic Dynein-Dependent Vesicular Transport from Early to Late Endosomes.” *Journal of Cell Biology* 123(6 I): 1373–87.

Änkö, Minna Liisa et al. 2012. “The RNA-Binding Landscapes of Two SR Proteins Reveal Unique Functions and Binding to Diverse RNA Classes.” *Genome Biology* 13(3): R17.

———. 2014a. “Regulation of Gene Expression Programmes by Serine-Arginine Rich Splicing Factors.” *Seminars in Cell and Developmental Biology* 32: 11–21.

———. 2014b. “Regulation of Gene Expression Programmes by Serine-Arginine Rich Splicing Factors.” *Seminars in Cell and Developmental Biology* 32: 11–21.

Aoyama, Takane et al. 2009. “Cayman Ataxia Protein Caytaxin Is Transported by Kinesin along Neurites through Binding to Kinesin Light Chains.” *Journal of Cell Science* 122(22): 4177–85.

Araki, Yoichi et al. 2007. “The Novel Cargo Alcadein Induces Vesicle Association of Kinesin-1 Motor Components and Activates Axonal Transport.” *EMBO Journal* 26(6): 1475–86.

Aubol, Brandon E. et al. 2013. “Partitioning RS Domain Phosphorylation in an SR Protein through the CLK and SRPK Protein Kinases.” *Journal of Molecular Biology* 425(16): 2894–2909.

Baas, Peter W, Jeffrey S Deitch, Mark M Black, and Gary A Banker. 1988. “Polarity Orientation of Microtubules in Hippocampal Neurons: Uniformity in the Axon and Nonuniformity in the Dendrite.” *Proceedings of the National Academy of Sciences of the United States of America* 85(21): 8335–39.

Bagni, Claudia, Flora Tassone, Giovanni Neri, and Randi Hagerman. 2012. “Fragile X Syndrome: Causes, Diagnosis, Mechanisms, and Therapeutics.” *Journal of Clinical Investigation* 122(12): 4314–22.

Barry, Joshua et al. 2014. “Ankyrin-G Directly Binds to Kinesin-1 to Transport Voltage-Gated Na+ Channels into Axons.” *Developmental Cell* 28(2): 117–31.

Baumann, Sebastian et al. 2020. “A Reconstituted Mammalian APC-Kinesin Complex Selectively Transports Defined Packages of Axonal MRNAs.” *Science Advances* 6(11): eaaz1588.

Baumann, Sebastian J et al. 2022. “APC Couples Neuronal MRNAs to Multiple Kinesins, EB1, and Shrinking Microtubule Ends for Bidirectional MRNA Motility.” *PNAS* 119(50).

Bear, J et al. 1999. “Identification of Novel Import and Export Signals of Human TAP, the Protein That Binds to the Constitutive Transport Element of the Type D Retrovirus MRNAs.” *Molecular and cellular biology* 19(9): 6306–17.

Becalska, Agata N., and Elizabeth R. Gavis. 2009. “Lighting up MRNA Localization in Drosophila Oogenesis.” *Development* 136(15): 2493–2503.

Belyy, Vladislav et al. 2016. “The Mammalian Dynein–Dynactin Complex Is a Strong Opponent to Kinesin in a Tug-of-War Competition.” *Nature Cell Biology* 18(9): 1018–24.

Benita Wiatrak,Adriana Kubis-Kubiak, Agnieszka Piwowar and Ewa Barg. 2020. “PC12 Cell Line: Cell Types, Coating of Culture Vessels, Differentiation and Other Culture Conditions.” *Cells* 9(958).

Ben-Yishay, Rakefet et al. 2019. “Imaging within Single NPCs Reveals NXF1’s Role in MRNA Export on the Cytoplasmic Side of the Pore.” *Journal of Cell Biology* 218(9): 2962–81.

Besir, Hüseyin. 2017. “A Generic Protocol for Purifying Disulfide-Bonded Domains and Random Protein Fragments Using Fusion Proteins with SUMO3 and Cleavage by SenP2 Protease.” In *Heterologous Gene Expression in E. Coli: Methods and Protocols, Methods in Molecular Biology*, , 33–43.

Bieling, Peter et al. 2010. 95 Methods in Cell Biology *Fluorescence Microscopy Assays on Chemically Functionalized Surfaces for Quantitative Imaging of Microtubule, Motor, and +tip Dynamics*. First edit. Elsevier.

Bourke, Ashley M., Andre Schwarz, and Erin M. Schuman. 2023. “De-Centralizing the Central Dogma: MRNA Translation in Space and Time.” *Molecular Cell* 83(3): 452–68.

Braun, Isabelle C. et al. 2001. “Overexpression of TAP/P15 Heterodimers Bypasses Nuclear Retention and Stimulates Nuclear MRNA Export.” *Journal of Biological Chemistry* 276(23): 20536–43.

Bremner, K Helen et al. 2009. “Adenovirus Transport via Direct Interaction of Cytoplasmic Dynein with the Viral Capsid Hexon Subunit.” *Cell Host and Microbe* 6(6): 523–35.

Brendel, Cornelia et al. 2004. “Characterization of Staufen 1 Ribonucleoprotein Complexes.” *The Biochemical journal* 384(Pt 2): 239–46.

Bullock, Simon L. 2007. “Translocation of MRNAs by Molecular Motors: Think Complex?” *Seminars in Cell and Developmental Biology* 18(2): 194–201.

Buxbaum, Adina R., Gal Haimovich, and Robert H. Singer. 2015. “In the Right Place at the Right Time: Visualizing and Understanding MRNA Localization.” *Nature Reviews Molecular Cell Biology* 16(2): 95–109.

Buxbaum, Adina R., Young J. Yoon, Robert H. Singer, and Hye Yoon Park. 2015. “Single-Molecule Insights into MRNA Dynamics in Neurons.” *Trends in Cell Biology* 25(8): 468–75.

Cai, Dawen, Adam D. Hoppe, Joel A. Swanson, and Kristen J. Verhey. 2007. “Kinesin-1 Structural Organization and Conformational Changes Revealed by FRET Stoichiometry in Live Cells.” *Journal of Cell Biology* 176(1): 51–63.

Cajigas, Iván J. et al. 2012. “The Local Transcriptome in the Synaptic Neuropil Revealed by Deep Sequencing and High-Resolution Imaging.” *Neuron* 74(3): 453–66.

Caput, D et al. 1986. “Identification of a Common Nucleotide Sequence in the 3’-Untranslated Region of MRNA Molecules Specifying Inflammatory Mediators.” *Proceedings of the National Academy of Sciences of the United States of America* 83(6): 1670–74.

Castoldi, Mirco, and Andrei V. Popov. 2003. “Purification of Brain Tubulin through Two Cycles of Polymerization- Depolymerization in a High-Molarity Buffer.” *Protein Expression and Purification* 32(1): 83–88.

Cavaloc, Yvon, Cyril F. Bourgeois, Liliane Kister, and James Stévenin. 1999. “The Splicing Factors 9G8 and SRp20 Transactivate Splicing through Different and Specific Enhancers.” *Rna* 5(3): 468–83.

Chabanon, Herve, Ian Mickleburgh, and John Hesketh. 2006. “Zipcodes and Postage Stamps: MRNA Localisation Signals and Their Trans-Acting Binding Proteins.” *Briefings in Functional Genomics and Proteomics* 3(3): 240–56.

Chiba, Kyoko, Kassandra M. Ori-McKenney, Shinsuke Niwa, and Richard J. McKenney. 2022. “Synergistic Autoinhibition and Activation Mechanisms Control Kinesin-1 Motor Activity.” *Cell Reports* 39(9): 110900.

Chu, Jen Fei et al. 2019. “TDP-43 Regulates Coupled Dendritic MRNA Transport-Translation Processes in Co-Operation with FMRP and Staufen1.” *Cell Reports* 29(10): 3118-3133.e6.

Chu, Yuan et al. 2019. “Nudt21 Regulates the Alternative Polyadenylation of Pak1 and Is Predictive in the Prognosis of Glioblastoma Patients.” *Oncogene* 38(21): 4154–68.

Clancy, Bason E. et al. 2011. “A Universal Pathway for Kinesin Stepping.” *Nature Structural and Molecular Biology* 18(9): 1020–27.

Cline, Melissa S et al. 2007. “Integration of Biological Networks and Gene Expression Data Using Cytoscape.” *Nature Protocols* 2(10): 2366–82.

Cockburn, Joseph J.B. et al. 2018. “Insights into Kinesin-1 Activation from the Crystal Structure of KLC2 Bound to JIP3.” *Structure* 26(11): 1486-1498.e6.

Coy, David L., William O. Hancock, Michael Wagenbach, and Jonathon Howard. 1999. “Kinesin’s Tail Domain Is an Inhibitory Regulator of the Motor Domain.” *Nature Cell Biology* 1(5): 288–92.

Crimella, C et al. 2012. “Mutations in the Motor and Stalk Domains of KIF5A in Spastic Paraplegia Type 10 and in Axonal Charcot – Marie – Tooth Type 2.” *Clin Genet* 82: 157–164.

Das, Sulagna et al. 2021. “Intracellular MRNA Transport and Localized Translation.” *Nature Reviews Molecular Cell Biology* 22(7): 483–504.

Derti, Adnan et al. 2012. “A Quantitative Atlas of Polyadenylation in Five Mammals.” *Genome Research* 22(6): 1173–83.

Dictenberg, Jason B. et al. 2008. “A Direct Role for FMRP in Activity-Dependent Dendritic MRNA Transport Links Filopodial-Spine Morphogenesis to Fragile X Syndrome.” *Developmental Cell* 14(6): 926–39.

Dienstbier, Martin, Florian Boehl, Xuan Li, and Simon L. Bullock. 2009. “Egalitarian Is a Selective RNA-Binding Protein Linking MRNA Localization Signals to the Dynein Motor.” *Genes and Development* 23(13): 1546–58.

Dietrich, Kristen A. et al. 2008. “The Kinesin-1 Motor Protein Is Regulated by a Direct Interaction of Its Head and Tail.” *Proceedings of the National Academy of Sciences of the United States of America* 105(26): 8938–43.

Dimitrova-Paternoga, Lyudmila et al. 2021. “Molecular Basis of MRNA Transport by a Kinesin-1-Atypical Tropomyosin Complex.” *Genes and Development* 35(13): 1–16.

Ding, D, S M Parkhurst, S R Halsell, and H D Lipshitz. 1993. “Dynamic Hsp83 RNA Localization during Drosophila Oogenesis and Embryogenesis.” *Molecular and Cellular Biology* 13(6): 3773–81.

Dodding, Mark P, Richard Mitter, Ashley C Humphries, and Michael Way. 2011. “A Kinesin-1 Binding Motif in Vaccinia Virus That Is Widespread throughout the Human Genome.” *The EMBO journal* 30: 4523–38.

Edens, Brittany M. et al. 2019. “FMRP Modulates Neural Differentiation through M6A-Dependent MRNA Nuclear Export.” *Cell Reports* 28(4): 845-854.e5.

Eliscovich, Carolina, Shailesh M Shenoy, and Robert H Singer. 2017. “Imaging MRNA and Protein Interactions within Neurons.” *Proceedings of the National Academy of Sciences of the United States of America* 114(10): E1875–84.

Elvira, George et al. 2006. “Characterization of an RNA Granule from Developing Brain.” *Molecular and Cellular Proteomics* 5(4): 635–51.

Engel, Krysta L. et al. 2020. “Mechanisms and Consequences of Subcellular RNA Localization across Diverse Cell Types.” *Traffic* 21(6): 404–18.

Feng, Y et al. 1997. “FMRP Associates with Polyribosomes as an MRNP, and the I304N Mutation of Severe Fragile X Syndrome Abolishes This Association.” *Molecular cell* 1(1): 109–18.

Ferro, Luke S et al. 2022. “Structural and Functional Insight into Regulation of Kinesin-1 by Microtubule-Associated Protein MAP7.” *Science (New York, N.Y.)* 375(6578): 326–31.

Fields, Stanley, and Ok-kyu Song. 1989. “A Novel Genetic System to Detect Protein-Protein Interactions.” *Nature* 342: 189–92.

Forrest, Kevin M, and Elizabeth R Gavis. 2003. “Live Imaging of Endogenous RNA Reveals a Diffusion and Entrapment Mechanism for Nanos MRNA Localization in Drosophila.” *Current Biology* 13: 1159–68.

Francis, Dana M., and Rebecca Page. 2010. “Strategies to Optimize Protein Expression in E. Coli.” *Current Protocols in Protein Science* (SUPPL. 61): 1–29.

Friedman, Dara S., and Ronald D. Vale. 1999. “Single-Molecule Analysis of Kinesin Motility Reveals Regulation by the Cargo-Binding Tail Domain.” *Nature cell biology* 1(5): 293–97.

Fujita, Toshitsugu et al. 2007. “Axonal Guidance Protein FEZ1 Associates with Tubulin and Kinesin Motor Protein to Transport Mitochondria in Neurites of NGF-Stimulated PC12 Cells.” *Biochemical and Biophysical Research Communications* 361(3): 605–10.

Fukuda, Yusuke et al. 2021. “Binding and Transport of Sfpq-Rna Granules by Kif5a/Klc1 Motors Promotes Axon Survival.” *Journal of Cell Biology* 220(1).

Fusco, Claudia M. et al. 2021. “Neuronal Ribosomes Exhibit Dynamic and Context-Dependent Exchange of Ribosomal Proteins.” *Nature Communications* 12(1): 1–14.

Gáspár, Imre et al. 2023. “An RNA-Based Feed-Forward Mechanism Ensures Motor Switching in Oskar MRNA Transport.” *Journal of Cell Biology* 222(7).

Gennarino, Vincenzo A. et al. 2015. “NUDT21-Spanning CNVs Lead to Neuropsychiatric Disease and Altered MeCP2 Abundance via Alternative Polyadenylation.” *eLife* 4(AUGUST2015): 1–13.

Glock, Caspar, Maximilian Heumüller, and Erin M. Schuman. 2017. “MRNA Transport & Local Translation in Neurons.” *Current Opinion in Neurobiology* 45: 169–77.

Goering, Raeann et al. 2020. “FMRP Promotes RNA Localization to Neuronal Projections through Interactions between Its RGG Domain and G-Quadruplex RNA Sequences.” *eLife* 9: 1–31.

Goldman, Chandler H., Hannah Neiswender, Rajalakshmi Veeranan-Karmegam, and Graydon B. Gonsalvez. 2019. “The Egalitarian Binding Partners Dynein Light Chain and Bicaudal-D Act Sequentially to Link MRNA to the Dynein Motor.” *Development (Cambridge)* 146(15).

Golovanov, Alexander P, Guillaume M Hautbergue, Stuart A Wilson, and Lu-yun Lian. 2004. “A Simple Method for Improving Protein Solubility and Long-Term Stability.” *Journal of the American Chemical Society* 126(29): 8933–39.

Goodson, Holly V, and Erin M Jonasson. 2018. “Microtubules and Microtubule-Associated Proteins.” *Cold Spring Harb Perspect Biol*.

Grawenhoff, Julia, Sebastian Baumann, and Sebastian P Maurer. 2022. “In Vitro Reconstitution of Kinesin-Based, Axonal MRNA Transport.” In *Methods in Molecular Biology*, , 547–68.

Gumy, Laura F. et al. 2011. “Transcriptome Analysis of Embryonic and Adult Sensory Axons Reveals Changes in MRNA Repertoire Localization.” *Rna* 17(1): 85–98.

Hackney, D. D., and M. F. Stock. 2000. “Kinesin’s IAK Tail Domain Inhibits Initial Microtubule-Stimulated ADP Release.” *Nature Cell Biology* 2(5): 257–60.

Hargous, Yann et al. 2006. “Molecular Basis of RNA Recognition and TAP Binding by the SR Proteins SRp20 and 9G8.” *EMBO Journal* 25(21): 5126–37.

Hautbergue, Guillaume M. et al. 2008. “Mutually Exclusive Interactions Drive Handover of MRNA from Export Adaptors to TAP.” *Proceedings of the National Academy of Sciences* 105(13): 5154–59.

Heisler, Frank F. et al. 2014. “GRIP1 Interlinks N-Cadherin and AMPA Receptors at Vesicles to Promote Combined Cargo Transport into Dendrites.” *Proceedings of the National Academy of Sciences of the United States of America* 111(13): 5030–35.

Henrichs, Verena et al. 2020. “Mitochondria-Adaptor TRAK1 Promotes Kinesin-1 Driven Transport in Crowded Environments.” *Nature Communications* 11(1): 1–13.

Herold, Andrea, Tetyana Klymenko, and Elisa Izaurralde. 2001. “NXF1 / P15 Heterodimers Are Essential for MRNA Nuclear Export in Drosophila.” : 1768–80.

Herrmann, Harald, and Ueli Aebi. 2016. “Intermediate Filaments: Structure and Assembly.” *Cold Spring Harbor Perspectives in Biology* 8(11).

Hertel, Klemens J, and Brenton R Graveley. 2005. “RS Domains Contact the Pre-MRNA throughout Spliceosome Assembly.” *Trends in Biochemical Sciences* 30(3): 115–18.

Heym, Roland G. et al. 2013. “In Vitro Reconstitution of an MRNA-Transport Complex Reveals Mechanisms of Assembly and Motor Activation.” *Journal of Cell Biology* 203(6): 971–84.

Hirokawa, N. 2006. “MRNA Transport in Dendrites: RNA Granules, Motors, and Tracks.” *Journal of Neuroscience* 26(27): 7139–42.

Hirokawa, Nobutaka, Shinsuke Niwa, and Yosuke Tanaka. 2010. “Molecular Motors in Neurons: Transport Mechanisms and Roles in Brain Function, Development, and Disease.” *Neuron* 68(4): 610–38.

Holt, Christine E., and Simon L. Bullock. 2009. “Subcellular MRNA Localization in Animal Cells and Why It Matters.” *Science* 326(5957): 1212–16.

Holt, Christine E., and Erin M. Schuman. 2013. “The Central Dogma Decentralized: New Perspectives on RNA Function and Local Translation in Neurons.” *Neuron* 80(3): 648–57.

Hooikaas, Peter Jan et al. 2019. “MAP7 Family Proteins Regulate Kinesin-1 Recruitment and Activation.” *Journal of Cell Biology* 218(4): 1298–1318.

Huang, Y., T. A. Yario, and J. A. Steitz. 2004. “A Molecular Link between SR Protein Dephosphorylation and MRNA Export.” *Proceedings of the National Academy of Sciences* 101(26): 9666–70.

Huang, Yingqun, Renata Gattoni, James Stévenin, and Joan A. Steitz. 2003. “SR Splicing Factors Serve as Adapter Proteins for TAP-Dependent MRNA Export.” *Molecular Cell* 11(3): 837–43.

Huang, Yingqun, and Joan A. Steitz. 2001. “Splicing Factors SRp20 and 9G8 Promote the Nucleocytoplasmic Export of MRNA.” *Molecular Cell* 7(4): 899–905.

Hyman, Anthony et al. 1991. “Preparation of Modified Tubulins.” *Methods in Enzymology* 196(C): 478–85.

Inouye, Satoshi, and Yuiko Sahara. 2008. “Soluble Protein Expression in E. Coli Cells Using IgG-Binding Domain of Protein A as a Solubilizing Partner in the Cold Induced System.” *Biochemical and Biophysical Research Communications* 376(3): 448–53.

Ishizuka, Norio, W. Maxwell Cowan, and David G. Amaral. 1995. “A Quantitative Analysis of the Dendritic Organization of Pyramidal Cells in the Rat Hippocampus.” *Journal of Comparative Neurology* 362(1): 17–45.

Jang, Ha Na et al. 2014. “Exon 9 Skipping of Apoptotic Caspase-2 Pre-MRNA Is Promoted by SRSF3 through Interaction with Exon 8.” *Biochimica et Biophysica Acta - Gene Regulatory Mechanisms* 1839(1): 25–32.

Jeffery, William R., Craig R. Tomlinson, and Richard D. Brodeur. 1983. “Localization of Actin Messenger RNA during Early Ascidian Development.” *Developmental Biology* 99(2): 408–17.

Jeong, Sunjoo. 2017. “SR Proteins: Binders, Regulators, and Connectors of RNA.” *Molecules and Cells* 40(1): 1–9.

Jia, Rong, and Zhi-Ming Zheng. 2009. “Regulation of Bovine Papillomavirus Type 1 Gene Expression by RNA Processing.” *Frontiers in Bioscience* 14: 1270–82.

Jin, Li et al. 2003. “Tap and NXT Promote Translation of Unspliced MRNA.” *Genes and Development* 17(24): 3075–86.

Jun, Lin et al. 2001. “NXF5, a Novel Member of the Nuclear RNA Export Factor Family, Is Lost in a Male Patient with a Syndromic Form of Mental Retardation.” *Current Biology* 11(18): 1381–91.

Kaan, Hung Yi Kristal, David D. Hackney, and Frank Kozielski. 2011. “The Structure of the Kinesin-1 Motor-Tail Complex Reveals the Mechanism of Autoinhibition.” *Science* 333(6044): 883–85.

Kanai, Yoshimitsu et al. 2000. “KIF5C, a Novel Neuronal Kinesin Enriched in Motor Neurons.” *Journal of Neuroscience* 20(17): 6374–84.

Kanai, Yoshimitsu, Naoshi Dohmae, and Nobutaka Hirokawa. 2004. “Kinesin Transports RNA: Isolation and Characterization of an RNA-Transporting Granule.” *Neuron* 43(4): 513–25.

Katahira, Jun et al. 2008. “Nuclear RNA Export Factor 7 Is Localized in Processing Bodies and Neuronal RNA Granules through Interactions with Shuttling HnRNPs.” *Nucleic Acids Research* 36(2): 616–28.

Katahira, Jun, Lyudmila Dimitrova, Yumiko Imai, and Ed Hurt. 2015. “NTF2-like Domain of Tap Plays a Critical Role in Cargo MRNA Recognition and Export.” *Nucleic Acids Research* 43(3): 1894–1904.

Kawano, Takanori et al. 2012. “A Small Peptide Sequence Is Sufficient for Initiating Kinesin-1 Activation Through Part of TPR Region of KLC1.” *Traffic* 13: 834–48.

Kellems, Rod E., Venita F. Allison, and Ronald A. Butow. 1974. “Cytoplasmic Type 80 S Ribosomes Associated with Yeast Mitochondria.” *Journal of Biological Chemistry* 249(10): 3297–3303.

Kellems, Rod E., and Ronald A. Butow. 1972. “Cytoplasmic-Type 80 S Ribosomes Associated with Yeast Mitochondria.” *Journal of Biological Chemistry* 247(24): 8043–50.

King, Mary Lou, Timothy J. Messitt, and Kimberly L. Mowry. 2005. “Putting RNAs in the Right Place at the Right Time: RNA Localization in the Frog Oocyte.” *Biology of the Cell* 97(1): 19–33.

Konecna, Anetta et al. 2006. “Calsyntenin-1 Docks Vesicular Cargo to Kinesin-1.” *Molecular biology of the cell* 17: 3651–63.

Lai, Ming Chih, Ru Inn Lin, and Woan Yuh Tarn. 2001. “Transportin-SR2 Mediates Nuclear Import of Phosphorylated SR Proteins.” *Proceedings of the National Academy of Sciences of the United States of America* 98(18): 10154–59.

Lai, Ming Chih, and Woan Yuh Tarn. 2004. “Hypophosphorylated ASF/SF2 Binds TAP and Is Present in Messenger Ribonucleoproteins.” *Journal of Biological Chemistry* 279(30): 31745–49.

Langdon, Erin M., and Amy S. Gladfelter. 2018. “A New Lens for RNA Localization: Liquid-Liquid Phase Separation.” *Annual Review of Microbiology* 72(1): 255–71.

Lashkevich, Kseniya A., and Sergey E. Dmitriev. 2021. “MRNA Targeting, Transport and Local Translation in Eukaryotic Cells: From the Classical View to a Diversity of New Concepts.” *Molecular Biology* 55(4): 507–37.

Lawrence, Carolyn J. et al. 2004. “A Standardized Kinesin Nomenclature.” *Journal of Cell Biology* 167(1): 19–22.

Lécuyer, Eric et al. 2007. “Global Analysis of MRNA Localization Reveals a Prominent Role in Organizing Cellular Architecture and Function.” *Cell* 131(1): 174–87.

Lee Sweeney, H., and Erika L.F. Holzbaur. 2018. “Motor Proteins.” *Cold Spring Harbor Perspectives in Biology* 10(5): 1–17.

Leppek, Kathrin, Rhiju Das, and Maria Barna. 2018. “Functional 5′ UTR MRNA Structures in Eukaryotic Translation Regulation and How to Find Them.” *Nature Reviews Molecular Cell Biology* 19(3): 158–74.

Liao, Ya Cheng et al. 2019. “RNA Granules Hitchhike on Lysosomes for Long-Distance Transport, Using Annexin A11 as a Molecular Tether.” *Cell* 179(1): 147-164.e20.

Lin, Jianfeng et al. 2014. “Structural Mechanism of the Dynein Power Stroke.” *Nature Cell Biology* 16(5): 479–85.

Lipka, Joanna, Marijn Kuijpers, Jacek Jaworski, and Casper C. Hoogenraad. 2013. “Mutations in Cytoplasmic Dynein and Its Regulators Cause Malformations of Cortical Development and Neurodegenerative Diseases.” *Biochemical Society Transactions* 41(6): 1605–12.

Long, Roy M. et al. 1997. “Mating Type Switching in Yeast Controlled by Asymmetric Localization of ASH1 MRNA.” *Science* 277(5324): 383–87.

Ma, Wei-jun, Sangmi Chung, and Henry Furneaux. 1997. “The Elav-like Proteins Bind to AU-Rich Elements and to the Poly (A) Tail of MRNA.” 25(18): 3564–69.

Machleidt, Thomas et al. 2015. “NanoBRET-A Novel BRET Platform for the Analysis of Protein-Protein Interactions.” *ACS Chemical Biology* 10(8): 1797–1804.

Mallardo, Massimo et al. 2003. “Isolation and Characterization of Staufen-Containing Ribonucleoprotein Particles from Rat Brain.” *Proceedings of the National Academy of Sciences of the United States of America* 100(4): 2100–2105.

Mamon, L. A. et al. 2017. “RNA-Binding Proteins of the NXF (Nuclear Export Factor) Family and Their Connection with the Cytoskeleton.” *Cytoskeleton* 74(4): 161–69.

Manley, James L., and Adrian R. Krainer. 2010. “A Rational Nomenclature for Serine/Arginine-Rich Protein Splicing Factors (SR Proteins).” *Genes & Development* 24: 1073–74.

Martin, Kelsey C., and Anne Ephrussi. 2009. “MRNA Localization: Gene Expression in the Spatial Dimension.” *Cell* 136(4): 719–30.

Matzat, Leah H, Stephen Berberoglu, and Lyne Lévesque. 2008. “Formation of a Tap/NXF1 Homotypic Complex Is Mediated through the Amino-Terminal Domain of Tap and Enhances Interaction with Nucleoporins.” *Molecular Biology of the Cell* 19: 327–38.

Maurer, S.P. et al. 2012. “EBs Recognize a Nucleotide-Dependent Structural Cap at Growing Microtubule Ends.” *Cell* 149(2).

Mayr, Christine. 2019. “What Are 3′ Utrs Doing?” *Cold Spring Harbor Perspectives in Biology* 11(10).

McClintock, Mark A. et al. 2018. “RNA-Directed Activation of Cytoplasmic Dynein-1 in Reconstituted Transport RNPs.” *eLife* 7: 1–29.

McKenney, Richard J et al. 2014a. “Activation of Cytoplasmic Dynein Motility by Dynactin-Cargo Adapter Complexes.” *Science* 345(6194): 337–41.

———. 2014b. “Activation of Cytoplasmic Dynein Motility by Dynactin-Cargo Adapter Complexes.” *Science* 345(6194): 337–41.

Medioni, Caroline, Kimberly Mowry, and Florence Besse. 2012. “Principles and Roles of MRNA Localization in Animal Development.” *Development (Cambridge)* 139(18): 3263–76.

Michaud, Morgane, Laurence Maréchal-Drouard, and Anne Marie Duchêne. 2010. “RNA Trafficking in Plant Cells: Targeting of Cytosolic MRNAs to the Mitochondrial Surface.” *Plant Molecular Biology* 73(6): 697–704.

Middleton, Sarah A., James Eberwine, and Junhyong Kim. 2019. “Comprehensive Catalog of Dendritically Localized MRNA Isoforms from Sub-Cellular Sequencing of Single Mouse Neurons.” *BMC Biology* 17(1): 1–16.

Miki, H., M. Setou, K. Kaneshiro, and N. Hirokawa. 2001. “All Kinesin Superfamily Protein, KIF, Genes in Mouse and Human.” *Proceedings of the National Academy of Sciences of the United States of America* 98(13): 7004–11.

Mikl, Martin et al. 2021. “BioRxiv: A Massively Parallel Reporter Assay Reveals Focused and Broadly Encoded RNA Localization Signals in Neurons Affiliations :” *bioRxiv*.

———. 2022. “A Massively Parallel Reporter Assay Reveals Focused and Broadly Encoded RNA Localization Signals in Neurons.” *Nucleic Acids Research*.

Mili, Stavroula, Konstadinos Moissoglu, and Ian G Macara. 2008. “Genome-Wide Screen Reveals APC-Associated RNAs Enriched in Cell Protrusions.” 453(May).

Milic, Bojan, Johan O.L. Andreasson, William O. Hancock, and Steven M. Block. 2014. “Kinesin Processivity Is Gated by Phosphate Release.” *Proceedings of the National Academy of Sciences of the United States of America* 111(39): 14136–40.

Mitchison, T, and M Kirschner. 1984. “Dynamic Instability of Microtubule Growth.” *Nature* 312(5991): 237–42.

Miura, Pedro et al. 2013. “Widespread and Extensive Lengthening of 3’ UTRs in the Mammalian Brain.” *Genome Research* 23(5): 812–25.

Mok, Yu Keung, Kevin W.H. Lo, and Mingjie Zhang. 2001. “Structure of Tctex-1 and Its Interaction with Cytoplasmic Dynein Intermediate Chain.” *Journal of Biological Chemistry* 276(17): 14067–74.

Monroy, Brigette Y. et al. 2018. “Competition between Microtubule-Associated Proteins Directs Motor Transport.” *Nature Communications* 9(1): 1–12.

Moor, Andreas E et al. 2017. “Global MRNA Polarization Regulates Translation Efficiency in the Intestinal Epithelium.” *Science* 357(6357): 1299–1303.

Müller-McNicoll, Michaela et al. 2016. “SR Proteins Are NXF1 Adaptors That Link Alternative RNA Processing to MRNA Export.” *Genes and Development* 30(5): 553–66.

Müller-McNicoll, Michaela, and Karla M. Neugebauer. 2013. “How Cells Get the Message: Dynamic Assembly and Function of MRNA-Protein Complexes.” *Nature Reviews Genetics* 14(4): 275–87.

Nakajima, Kazuo et al. 2012. “Molecular Motor KIF5A Is Essential for GABAA Receptor Transport, and KIF5A Deletion Causes Epilepsy.” *Neuron* 76(5): 945–61.

Nevo-Dinur, Keren, Anat Nussbaum-Shochat, Sigal Ben-Yehuda, and Orna Amster-Choder. 2011. “Translation-Independent Localization of MRNA in E. Coli.” *Science* 331(6020): 1081–84.

Nicolas, Aude et al. 2018. “Genome-Wide Analyses Identify KIF5A as a Novel ALS Gene.” *Neuron* 97(6): 1268-1283.e6.

Niessing, Dierk, Ralf Peter Jansen, Thomas Pohlmann, and Michael Feldbrügge. 2018. “MRNA Transport in Fungal Top Models.” *Wiley Interdisciplinary Reviews: RNA* 9(1): 1–13.

Nitta, Ryo, Yasushi Okada, and Nobutaka Hirokawa. 2008. “Structural Model for Strain-Dependent Microtubule Activation of Mg-ADP Release from Kinesin.” *Nature Structural and Molecular Biology* 15(10): 1067–75.

Okita, Thomas W., and Sang Bong Choi. 2002. “MRNA Localization in Plants: Targeting to the Cell’s Cortical Region and Beyond.” *Current Opinion in Plant Biology* 5(6): 553–59.

Palade, George E. 1955. “A SMALL PARTICULATE COMPONENT OF THE CYTOPLASM.” *J. Biophysic. and Biochem. Cytol.* 1(1).

Park, Hye Yoon et al. 2012. “An Unbiased Analysis Method to Quantify MRNA Localization Reveals Its Correlation with Cell Motility.” *Cell Reports* 1(2): 179–84.

———. 2014. “Visualization of Dynamics of Single Endogenous MRNA Labeled in Live Mouse.” *Science* 343(January): 422–24.

Paschal, Bryce M. 1987. “MAP 1C Is a Microtubule-Activated ATPase Which Translocates Microtubules In Vitro and Has Dynein-like Properties.” *The Journal of Cell Biology* 105(September): 1273–82.

Paschal, Bryce M, and Richard B Vallee. 1987. “Retrograde Transport by the Microtubule- Associated Protein MAP 1 C.” *Nature* 300: 181–83.

Pazo, Alejandra et al. 2019. “HCLE/RTRAF-HSPC117-DDx1-FAM98B: A New Cap-Binding Complex That Activates MRNA Translation.” *Frontiers in Physiology* 10(FEB): 1–13.

Pazour, Gregory J et al. 1999. “The DHC1b (DHC2) Isoform of Cytoplasmic Dynein Is Required for Flagellar Assembly.” *The Journal of Cell Biology* 144(3): 473–82.

Peña-Ortega, Fernando, Ángel Abdiel Robles-Gómez, and Lorena Xolalpa-Cueva. 2022. “Microtubules as Regulators of Neural Network Shape and Function: Focus on Excitability, Plasticity and Memory.” *Cells* 11(6).

Pernigo, Stefano et al. 2018. “Structural Basis for Isoform-Specific Kinesin-1 Recognition of Y-Acidic Cargo Adaptors.” *eLife* 7: 1–22.

Pernigo, Stefano, Anneri Lamprecht, Roberto A. Steiner, and Mark P. Dodding. 2013. “Structural Basis for Kinesin-1:Cargo Recognition.” *Science* 340(6130): 356–59.

Pilling, Aaron D, Dai Horiuchi, Curtis M Lively, and William M Saxton. 2006. “Kinesin-1 and Dynein Are the Primary Motors for Fast Transport of Mitochondria in Drosophila Motor Axons.” *Molecular Biology of the Cell* 17(April): 2057–68.

Pocock, Ginger M. et al. 2016. “HIV-1 and M-PMV RNA Nuclear Export Elements Program Viral Genomes for Distinct Cytoplasmic Trafficking Behaviors.” *PLoS Pathogens* 12(4): 1–30.

Poirier, Karine et al. 2013. “Mutations in TUBG1, DYNC1H1, KIF5C and KIF2A Cause Malformations of Cortical Development and Microcephaly.” *Nature genetics* 45(6).

Porter, Mary E et al. 1999. “Cytoplasmic Dynein Heavy Chain 1b Is Required for Flagellar Assembly in Chlamydomonas.” *Molecular Biology of the Cell* 10: 693–712.

Preitner, Nicolas et al. 2014. “APC Is an RNA-Binding Protein , and Its Interactome Provides a Link to Neural Development and Microtubule Assembly.” *Cell* 158(2): 368–82.

Raran-kurussi, Sreejith, and David S Waugh. 2012. “The Ability to Enhance the Solubility of Its Fusion Partners Is an Intrinsic Property of Maltose-Binding Protein but Their Folding Is Either Spontaneous Or.” 7(11).

Raran-Kurussi, Sreejith, and David S. Waugh. 2014. “Unrelated Solubility-Enhancing Fusion Partners MBP and NusA Utilize a Similar Mode of Action.” *Biotechnology and Bioengineering* 111(No. 12).

Reck-Peterson, Samara L., William B. Redwine, Ronald D. Vale, and Andrew P. Carter. 2018. “The Cytoplasmic Dynein Transport Machinery and Its Many Cargoes.” *Nature Reviews Molecular Cell Biology* 19(6): 382–98.

Reddy, Babu J. N. et al. 2016. “Load-Induced Enhancement of Dynein Force Production by LIS1–NudE in Vivo and in Vitro.” *Nature Communications* 7: 12259.

Reid, Evan et al. 2002. “A Kinesin Heavy Chain (KIF5A) Mutation in Hereditary Spastic Paraplegia (SPG10).” *Am. J. Hum. Genet.* 71: 1189–94.

Remans, Kim et al. 2022. “Protein Purification Strategies Must Consider Downstream Applications and Individual Biological Characteristics.” *Microbial Cell Factories* 21(1): 1–16.

Rice, Sarah et al. 1999. “A Structural Change in the Kinesin Motor Protein That Drives Motility.” *Nature* 402(6763): 778–84.

Richards, Alicia L, Manon Eckhardt, and Nevan J Krogan. 2021. “Mass Spectrometry-based Protein–Protein Interaction Networks for the Study of Human Diseases.” *Molecular systems biology* 17(e8792).

Rodrigues, Elsa C. et al. 2021. “Mammalian Neuronal MRNA Transport Complexes: The Few Knowns and the Many Unknowns.” *Frontiers in Integrative Neuroscience* 15(June): 1–8.

Roll-Mecak, Antonina. 2015. “Intrinsically Disordered Tubulin Tails: Complex Tuners of Microtubule Functions?” *Seminars in Cell and Developmental Biology* 37: 11–19.

Rosa-Ferreira, Cláudia, and Sean Munro. 2011. “Arl8 and SKIP Act Together to Link Lysosomes to Kinesin-1.” *Developmental Cell* 21(6): 1171–78.

Rosenfeld, Steven S. et al. 2003. “Stepping and Stretching. How Kinesin Uses Internal Strain to Walk Processively.” *Journal of Biological Chemistry* 278(20): 18550–56.

Rosenfeld, Steven S., Anne Houdusse, and H. Lee Sweeney. 2005. “Magnesium Regulates ADP Dissociation from Myosin V.” *Journal of Biological Chemistry* 280(7): 6072–79.

Saito, Kuniaki et al. 2004. “TAP/NXF1, the Primary MRNA Export Receptor, Specifically Interacts with a Neuronal RNA-Binding Protein HuD.” *Biochemical and Biophysical Research Communications* 321(2): 291–97.

Sanghavi, Paulomi et al. 2013. “Dynein Associates with Oskar MRNPs and Is Required for Their Efficient Net Plus-End Localization in Drosophila Oocytes.” *PLoS ONE* 8(11): 1–12.

Schaal, Thomas D., and Tom Maniatis. 1999. “Selection and Characterization of Pre-MRNA Splicing Enhancers: Identification of Novel SR Protein-Specific Enhancer Sequences.” *Molecular and Cellular Biology* 19(3): 1705–19.

Schlager, Max A., Andrea Serra-Marques, et al. 2014. “Bicaudal D Family Adaptor Proteins Control the Velocity of Dynein-Based Movements.” *Cell Reports* 8(5): 1248–56.

Schlager, Max A, Ha Thi Hoang, et al. 2014. “*In Vitro* Reconstitution of a Highly Processive Recombinant Human Dynein Complex.” *The EMBO Journal* 33(17): 1855–68.

Schmidt, Michael R et al. 2009. “Regulation of Endosomal Membrane Traffic by a Gadkin/AP-1/Kinesin KIF5 Complex.” *Proceedings of the National Academy of Sciences* 106(36): 15344–49.

Schnitzer, Mark J., and Steven M. Block. 1997. “Kinesin Hydrolyses One ATP per 8-Nm Step.” *Nature* 388(6640): 386–90.

Schroer, Trina A, Eric R. Steuer, and Michael P. Sheetz. 1989. “Cytoplasmic Dynein Is a Minus End-Directed Motor for Membranous Organelles.” *Cell* 56(6): 937–46.

Schwich, Oliver Daniel et al. 2021. “SRSF3 and SRSF7 Modulate 3′UTR Length through Suppression or Activation of Proximal Polyadenylation Sites and Regulation of CFIm Levels.” *Genome Biology* 22(1): 1–35.

Seitz, Arne, and Thomas Surrey. 2006. “Processive Movement of Single Kinesins on Crowded Microtubules Visualized Using Quantum Dots.” *The EMBO journal* 25(2): 267–77.

Serra-marques, Andrea, Maud Martin, Eugene A Katrukha, and Ilya Grigoriev. 2020. “Concerted Action of Kinesin-1 KIF5B and Kinesin-3 KIF13B Promotes Efficient Transport of Exocytotic Vesicles to Microtubule plus Ends.”

Shah, Sneha et al. 2020. “FMRP Control of Ribosome Translocation Promotes Chromatin Modifications and Alternative Splicing of Neuronal Genes Linked to Autism.” *Cell Reports* 30(13): 4459-4472.e6.

Shepard, K. A. et al. 2003. “Widespread Cytoplasmic MRNA Transport in Yeast: Identification of 22 Bud-Localized Transcripts Using DNA Microarray Analysis.” *Proceedings of the National Academy of Sciences of the United States of America* 100(20): 11429–34.

Shimizu, Takashi, Kurt S. Thorn, Aaron Ruby, and Ronald D. Vale. 2000. “ATPase Kinetic Characterization and Single Molecule Behavior of Mutant Human Kinesin Motors Defective in Microtubule-Based Motility.” *Biochemistry* 39(18): 5265–73.

Shirokikh, Nikolay E., and Thomas Preiss. 2018. “Translation Initiation by Cap-Dependent Ribosome Recruitment: Recent Insights and Open Questions.” *Wiley Interdisciplinary Reviews: RNA* 9(4): 1–45.

Siepel, Adam et al. 2005. “Evolutionarily Conserved Elements in Vertebrate, Insect, Worm, and Yeast Genomes.” *Genome Research* 15(8): 1034–50.

Sladewski, Thomas E et al. 2018. “Recruitment of Two Dyneins to an MRNA-Dependent Bicaudal D Transport Complex.” *BioRxiv* 2.

Sladewski, Thomas E, Carol S Bookwalter, Myoung-Soon Hong, and Kathleen M Trybus. 2013. “Single-Molecule Reconstitution of MRNA Transport by a Class V Myosin.” *Nature structural & molecular biology* 20(8): 952–57.

Slišković, Irena, Hannah Eich, and Michaela Müller-McNicoll. 2022. “Exploring the Multifunctionality of SR Proteins.” *Biochemical Society Transactions* 50(1): 187–98.

Sonn-Segev, Adar et al. 2020. “Quantifying the Heterogeneity of Macromolecular Machines by Mass Photometry.” *Nature Communications* 11(1): 1–10.

St Johnston, Daniel. 1995. “The Intracellular Localization of Messenger RNAs.” *Cell* 81(2): 161–70.

Stock, Maryanne F. et al. 1999. “Formation of the Compact Confomer of Kinesin Requires a COOH-Terminal Heavy Chain Domain and Inhibits Microtubule-Stimulated ATPase Activity.” *Journal of Biological Chemistry* 274(21): 14617–23.

Subramanian, Murugan et al. 2011. “G-Quadruplex RNA Structure as a Signal for Neurite MRNA Targeting.” *EMBO Reports* 12(7): 697–704.

Sun, Faneng, Chuanmei Zhu, Ram Dixit, and Valeria Cavalli. 2011. “Sunday Driver/JIP3 Binds Kinesin Heavy Chain Directly and Enhances Its Motility.” *EMBO Journal* 30(16): 3416–29.

Sutton, Michael A., and Erin M. Schuman. 2006. “Dendritic Protein Synthesis, Synaptic Plasticity, and Memory.” *Cell* 127(1): 49–58.

Suzuki, Tadaki et al. 2005. “Identification of FEZ1 as a Protein That Interacts with JC Virus Agnoprotein and Microtubules: Role of Agnoprotein-Induced Dissociation of FEZ1 from Microtubules in Viral Propagation.” *Journal of Biological Chemistry* 280(26): 24948–56.

Swenson, Anja M. et al. 2014. “Magnesium Modulates Actin Binding and ADP Release in Myosin Motors.” *Journal of Biological Chemistry* 289(34): 23977–91.

Takano, Keizo, Takashi Miki, Jun Katahira, and Yoshihiro Yoneda. 2007. “NXF2 Is Involved in Cytoplasmic MRNA Dynamics through Interactions with Motor Proteins.” *Nucleic Acids Research* 35(8): 2513–21.

Taliaferro, J. Matthew et al. 2016. “Distal Alternative Last Exons Localize MRNAs to Neural Projections.” *Molecular cell* 61(6): 821–33.

Tan, Zhenyu et al. 2023. “Autoinhibited Kinesin-1 Adopts a Hierarchical Folding Pattern.” *bioRxiv*: 1–28.

Taniguchi, Yuichi et al. 2011. “Quantifying E. Coli Proteome and Transcriptome with Single-Molecule Sensitivity in Single Cells.” *Science (New York, N.Y.)* 329(5991): 533–39.

Teixeira, Mariana Bertini, Marcos Rodrigo Alborghetti, and Jörg Kobarg. 2019. “Fasciculation and Elongation Zeta Proteins 1 and 2: From Structural Flexibility to Functional Diversity.” *World Journal of Biological Chemistry* 10(2): 28–43.

Teplova, Marianna et al. 2011. “Structure-Function Studies of Nucleocytoplasmic Transport of Retroviral Genomic RNA by MRNA Export Factor TAP.” *Nature Structural and Molecular Biology* 18(9): 990–98.

Thorn, Kurt S., Jeffrey A. Ubersax, and Ronald D. Vale. 2000. “Engineering the Processive Run Length of the Kinesin Motor.” *Journal of Cell Biology* 151(5): 1093–1100.

Tian, Bin, and James L. Manley. 2016. “Alternative Polyadenylation of MRNA Precursors.” *Nature Reviews Molecular Cell Biology* 18(1): 18–30.

Tintaru, Aura M. et al. 2007. “Structural and Functional Analysis of RNA and TAP Binding to SF2/ASF.” *EMBO Reports* 8(8): 756–62.

Trokter, Martina, Norbert Mücke, and Thomas Surrey. 2012. “Reconstitution of the Human Cytoplasmic Dynein Complex.” *Proceedings of the National Academy of Sciences* 109(51): 20895–900.

Turner-Bridger, Benita et al. 2018. “Single-Molecule Analysis of Endogenous β-Actin MRNA Trafficking Reveals a Mechanism for Compartmentalized MRNA Localization in Axons.” *Proceedings of the National Academy of Sciences of the United States of America* 115(41): E9697–9706.

Tushev, Georgi, Caspar Glock, Maximilian Heumüller, et al. 2018. “Alternative 3′ UTRs Modify the Localization, Regulatory Potential, Stability, and Plasticity of MRNAs in Neuronal Compartments.” *Neuron* 98(3): 495-511.e6.

Tushev, Georgi, Caspar Glock, Anne Biever, et al. 2018. “Regulatory Potential , Stability , and Plasticity of MRNAs in Neuronal Compartments NeuroResource the Localization , Regulatory Potential , Stability , and Plasticity of MRNAs in Neuronal Compartments.” : 495–511.

Twelvetrees, Alison E et al. 2016. “The Dynamic Localization of Cytoplasmic Dynein in Neurons Is Driven by Kinesin-1.” *Neuron* 90(5): 1000–1015.

Verbrugge, Sander, Siet M.J.L. Van Den Wildenberg, and Erwin J.G. Peterman. 2009. “Novel Ways to Determine Kinesin-1’s Run Length and Randomness Using Fluorescence Microscopy.” *Biophysical Journal* 97(8): 2287–94.

Verhey, Kristen J. et al. 1998. “Light Chain-Dependent Regulation of Kinesin’s Interaction with Microtubules.” *Journal of Cell Biology* 143(4): 1053–66.

Verhey, Kristen J., and Jennetta W. Hammond. 2009. “Traffic Control: Regulation of Kinesin Motors.” *Nature Reviews Molecular Cell Biology* 10(11): 765–77.

Viphakone, Nicolas et al. 2012. “TREX Exposes the RNA-Binding Domain of Nxf1 to Enable MRNA Export.” *Nature Communications* 3: 1006–11.

Walker, R. A. et al. 1988. “Dynamic Instability of Individual Microtubules Analyzed by Video Light Microscopy: Rate Constants and Transition Frequencies.” *The Journal of cell biology* 107(4): 1437–48.

Walsh, Matthew J., Guillaume M. Hautbergue, and Stuart A. Wilson. 2010. “Structure and Function of MRNA Export Adaptors.” *Biochemical Society Transactions* 38(1): 232–36.

Wegener, M., and M. Müller-McNicoll. 2019. “View from an MRNP: The Roles of SR Proteins in Assembly, Maturation and Turnover.” *Adv. Exp. Med. Biol.* 1203: 83–112.

Willemsen, Marjolein H et al. 2014. “Involvement of the Kinesin Family Members KIF4A and KIF5C in Intellectual Disability and Synaptic Function.” *Journal of Medical Genetics* 51(7): 487–94.

Williams, Lucy S. et al. 2014. “The Auto-Inhibitory Domain and ATP-Independent Microtubulebinding Region of Kinesin Heavy Chain Are Major Functional Domains for Transport in the Drosophila Germline.” *Development (Cambridge)* 141(1): 176–86.

Woźniak, Marcin J., and Victoria J. Allan. 2006. “Cargo Selection by Specific Kinesin Light Chain 1 Isoforms.” *EMBO Journal* 25(23): 5457–68.

Wu, Di, and Grzegorz Piszczek. 2020. “Measuring the Affinity of Protein-Protein Interactions on a Single-Molecule Level by Mass Photometry.” *Analytical Biochemistry* 592(November 2019).

———. 2021. “Standard Protocol for Mass Photometry Experiments.” *European Biophysics Journal* 50(3–4): 403–9.

Wu, Jane Y, and Tom Maniatis. 1993. “Specific Interactions between Proteins Implicated in Splice Site Selection and Regulated Alternative Splicing.” *Cell* 75: 1061–70.

Xie, Xiaohui et al. 2005. “Systematic Discovery of Regulatory Motifs in Human Promoters and 3′ UTRs by Comparison of Several Mammals.” *Nature* 434(7031): 338–45.

Yakimova, Anna O., Olga M. Pugacheva, Elena V. Golubkova, and Ludmila A. Mamon. 2016. “Cytoplasmic Localization of SBR (Dm NXF1) Protein and Its Zonal Distribution in the Ganglia of Drosophila Melanogaster Larvae.” *Invertebrate Neuroscience* 16(3): 1–9.

Yang, Jae Seong et al. 2018. “Rec-YnH Enables Simultaneous Many-by-Many Detection of Direct Protein–Protein and Protein–RNA Interactions.” *Nature Communications* 9(1).

Yildiz, Ahmet, Michio Tomishige, Arne Gennerich, and Ronald D. Vale. 2008. “Intramolecular Strain Coordinates Kinesin Stepping Behavior along Microtubules.” *Cell* 134(6): 1030–41.

Yip, Yan Y et al. 2016. “The Light Chains of Kinesin-1 Are Autoinhibited.” *Proceedings of the National Academy of Sciences of the United States of America* 113(9): 2418–23.

Zhang, Meiqin, Qiaoqiao Wang, and Yingqun Huang. 2007. “Fragile X Mental Retardation Protein FMRP and the RNA Export Factor NXF2 Associate with and Destabilize Nxf1 MRNA in Neuronal Cells.” *Proceedings of the National Academy of Sciences of the United States of America* 104(24): 10057–62.

Zhu, Haizhong et al. 2012. “Crystal Structures of the Tetratricopeptide Repeat Domains of Kinesin Light Chains: Insight into Cargo Recognition Mechanisms.” *PLoS ONE* 7(3): 1–10.

Zivraj, Krishna H et al. 2010. “Subcellular Profiling Reveals Distinct and Developmentally Regulated Repertoire of Growth Cone MRNAs.” *Journal of Neuroscience* 30(46): 15464–78.